The Structural and Performance Analysis of Active Camber Morphing Wing and Optimization

YANG XUE [redacted]

MPhil

Supervisor: Prof. Liyong Tong

A thesis submitted in fulfilment of
the requirements for the degree of
Master of Philosophy

School of Aerospace, Mechanical and Mechatronic Engineering
Faculty of Engineering
The University of Sydney
Australia

29 August 2025

Statement of Student Contribution

I hereby declare that all content within this thesis is the result of my individual work.
- I conducted the literature review and identified the starting point for my research.
- I developed modified methods based on existing approaches to enhance functionality and design quality.
- I independently learned how to use various commercial software tools and utilized them to validate my results.
- I wrote the MATLAB code used to generate all figures and results presented in this thesis.

This research reported in this thesis was supported by the award of a Research Training Program scholarship to the Mphil Candidate

Signature.....

Acknowledgements

First and foremost, I would like to express my deepest gratitude to my supervisor, Professor Liyong Tong, for his invaluable guidance and unwavering support throughout my research journey. He not only helped me identify an engaging and meaningful research direction but also provided continuous support along the way. During my studies, I faced challenges from various aspects, both academically and personally, yet he always encouraged me to choose the most comfortable and reasonable path forward. I am immensely grateful for his patience, understanding, and encouragement, which have been instrumental in the successful completion of my master's degree.

I would also like to extend my sincere thanks to my fellow research students and colleagues Yifu Lu, Yi Xing, Yanjun Yu, Wenwei Li, and Steven Deng. Their valuable suggestions and insightful ideas greatly assisted me in solving several complex problems throughout my research. I am truly grateful for their support and collaboration.

I would like to express my heartfelt gratitude to Zuping Huang, who provided me with invaluable emotional support during times of challenge and when I felt stuck with certain problems. Her encouragement gave me the confidence to complete both the challenging coding tasks and my thesis.

Finally, I am deeply thankful to my parents for their continuous emotional and financial support, which enabled me to pursue and complete my studies.

Abstract

This thesis presents an investigation into the design and optimization of an active camber morphing wing, employing shape parameterization, evolutionary algorithms, topology optimization, and advanced computational techniques to improve aerodynamic performance. The research aims to develop an airfoil capable of dynamically adapting its shape to different flight conditions, thereby improving key performance metrics such as lift, drag, and overall efficiency. While previous studies in the literature have explored various mechanisms for actuating morphing structures, this thesis proposes a solution that integrates a compliant mechanism capable of achieving the target shape while maintaining sufficient stiffness to withstand aerodynamic loads.

The first challenge addressed is the airfoil shape representation and optimization, accomplished through a modified Bezier-PARSEC (BP) parameterization method combined with a Differential Evolution (DE) algorithm. The BP method enables precise parameterization of the airfoil's camber and thickness profiles using a segmented approach, which allows for independent optimization of the leading and trailing edges while preserving the structural integrity of the middle section. The optimization process is driven by multi-objective functions, focused on maximizing aerodynamic performance indicators such as lift coefficient, lift-to-drag ratio, and endurance while ensuring that the airfoil's curve length remains consistent to prevent physically unrealistic shapes.

The shape optimization involves adjusting camber profile parameters within predetermined morphing ranges for choosing leading and trailing edges. The DE algorithm, known for its robustness in solving complex aerodynamic optimization problems, is applied to iteratively refine these parameters, seeking an optimal balance between aerodynamic performance and geometric feasibility. The flight conditions and boundary parameters defined in the

optimization provide a realistic framework for analyzing the morphing wing's behaviour under operational scenarios.

Building on aerodynamic optimization, the structural design and optimization focus on realizing the optimized airfoil shapes through a structural framework that supports dynamic morphing with the required stiffness. Topology optimization techniques are introduced to address this challenge, ensuring that the wing's internal structure can withstand aerodynamic loads while enabling controlled deformation. Two methods are developed to solve the challenge of finding the geometry difference between the target and actual profiles. Discretized finite element models of the leading and trailing edges are generated, allowing topology optimization to determine the optimal material distribution for these critical morphing regions.

The leading and trailing edges are designed separately, with comparative analyses performed between the optimized shape and the baseline airfoil. The design parameters used in topology optimization are systematically explored to illustrate their effects on the resulting designs. Coupled structural and aerodynamic analyses are conducted using MATLAB and commercial software, ensuring reliable and validated results.

In conclusion, this thesis presents an effective approach to the design and optimization of morphing wings by integrating aerodynamic and structural optimization processes. The applications of advanced optimization algorithms and computational tools discover the potential for improving aircraft performance through adaptive wing designs. This work contributes to the advancement of morphing wing technologies and provides some possible solutions for future developments in aeronautical engineering.

Contents

List of Figures

List of Tables

List of Abbreviations and parameters

E_0**:** Young's modulus of solid material.

$E_e(\rho_e)$**:** Interpolated element modulus.

$E_{\min}$**:** Young's modulus assigned to voids.

$F_{\textbf{input}}$**:** Applied actuation force.

$\Delta z_{\textbf{TE}}$**:** Trailing-edge thickness offset.

$\alpha_{\textbf{TE}}$**:** Trailing-edge camber-curve direction.

$\beta_{\textbf{TE}}$**:** Trailing-edge wedge angle.

$\gamma_{\textbf{LE}}$**:** Leading-edge camber angle (BP variable).

$\gamma_{\textbf{LE}}$**:** Leading-edge camber angle.

F: Global load vector.

K: Global stiffness matrix.

L: Adjoint load vector.

U: Global displacement vector.

V: Adjoint displacement vector.

ω**:** Filter-radius scaling factor.

ρ_e**:** Element pseudo-density (design variable in SIMP).

b_0**:** Bezier control coefficient for leading-edge camber.

b_2**:** Bezier control coefficient for camber crest.

b_7**:** Bezier control coefficient (mid-chord camber).

b_8**:** Bezier control coefficient for leading-edge thickness.

b_{15}**:** Bezier control coefficient for TE thickness.

b_{17}**:** Bezier control coefficient for TE camber.

c_1**:** Sensitivity-scaling coefficient 1.

c_2**:** Sensitivity-scaling coefficient 2.

p**:** SIMP penalty factor.

$r_{\min}$**:** Minimum physical filter radius.

$r_{\mathbf{LE}}$**:** Leading-edge radius.

v_{frac}**:** Prescribed volume-fraction constraint.

w_c**:** Compliance-term weighting factor.

x_0**:** Leading-edge Bezier anchor.

x_c**:** Camber-crest abscissa.

x_t**:** Thickness-crest abscissa.

$x_{\mathbf{end}}$**:** Chord-wise end control point.

x_{c1}**:** First segmentation abscissa (mid-chord fixed point).

x_{c2}**:** Second segmentation abscissa (mid-chord fixed point).

y_c**:** Camber-crest ordinate.

y_t**:** Thickness-crest ordinate.

y_{c1}**:** First segmentation ordinate (mid-chord fixed point).

y_{c2}**:** Second segmentation ordinate (mid-chord fixed point).

$z_{\mathbf{TE}}$**:** Trailing-edge thickness ordinate.

BP: Bezier–PARSEC (air-/foil parameterisation).

CAD: Computer-Aided Design.

CFD: Computational Fluid Dynamics.

DE: Differential Evolution.

DLR: Deutsches Zentrum für Luft- und Raumfahrt (German Aerospace Center).

DPL: Dynamic Perpendicular Line (shape-error metric).

DVP: Dynamic Vertical Plane (shape-error metric).

FEA: Finite Element Analysis.

FEM: Finite Element Method.

FSI: Fluid–Structure Interaction.

GA: Genetic Algorithm.

LE: Leading Edge.

MACW: Mission Adaptive Compliant Wing.

MAW: Mission Adaptive Wing.

NP: Population size in evolutionary algorithms.

SIMP: Solid Isotropic Material with Penalisation.

SMA: Shape Memory Alloy.

TE: Trailing Edge.

XFOIL: NASA viscous/inviscid airfoil solver.

CHAPTER 1

Introduction

The evolution of aircraft has consistently involved the optimization of both structure and materials. Conventional fixed-wing configurations are designed to achieve optimal efficiency under specific flight conditions, but they incur efficiency losses during other phases of flight or when performing maneuvers. The deflection of discrete control surfaces during takeoff, landing, maneuvering, or when changing cruising altitudes disrupts the aerodynamic continuity of the wing, resulting in increased drag and higher fuel consumption. Furthermore, the reliance on complex hydraulic and mechanical systems adds significant weight and reduces overall reliability. However, recent advancements in smart materials and optimization techniques have made the realization of morphing wings far more feasible than in the past.

The concept of the morphing wing dates back to 1903 when Orville and Wilbur Wright designed the first manned and powered aircraft, the Wright Flyer. The pilot controlled the aircraft by shifting a cradle and pulling cables to twist the wing, introducing an asymmetrically twisted morphing wing design intended for maneuvering through changes in lift distribution. In contrast, later aircraft achieved roll control using ailerons to modify the wing camber. Over time, as performance demands increased and flight conditions became more diverse, the original flexible and adaptable wing designs were replaced by rigid, fixed structures to enhance wing loading and reduce vibration-induced failures.

1.1 The classification of aircraft morphing wing

Morphing wings can be classified into three primary categories based on the section of the wing that undergoes shape adaptation, as illustrated in Figure 1.1.

- **Planform-Based Morphing:** This mode enables large-scale changes in aerodynamic properties, such as wing loading or longitudinal stability, allowing the aircraft to adapt to different flight regimes.
- **Out-of-Plane Morphing:** This type of morphing alters the lift distribution across the wing, which can be advantageous in increasing the stall angle of the airfoil or enhancing lateral stability in specific flight conditions.
- **Airfoil-Based Morphing:** In this category, the wing camber or thickness is modified to alter the lift coefficient at specific angles of attack, ultimately improving aerodynamic efficiency and performance across a variety of operating conditions.

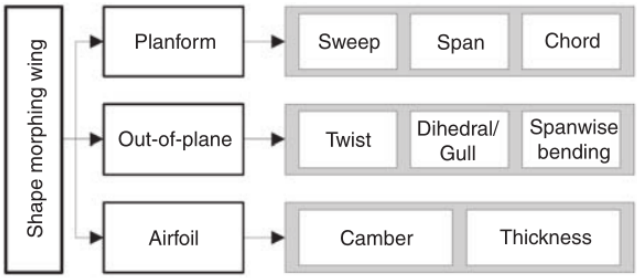

FIGURE 1.1. Three morphing modes[**1**]

Vasista et al. provided a detailed overview of morphing wing design, including the classification of shape parameters, performance benefits, and enabling technologies [**2**]. Projects prior to 2010 are categorized based on in-plane morphing shapes, out-of-plane morphing shapes, structural system combinations, and morphing types. The in-plane and out-of-plane shape parameters are outlined in a framework by Sofla et al., where changes in parameters such as chord length, camber, thickness, leading-edge radius, and bumps are recognized as critical to aircraft performance [**3**].

1.2 Design and Analysis Strategies for Morphing Wing

Designing a morphing wing is inherently a multidisciplinary enterprise, demanding a simultaneous grasp of structural mechanics, unsteady aerodynamics, smart-material actuation, and aircraft-grade manufacturing constraints. From the outset, the structural and aerodynamic models must be coupled—not treated in sequence—so that load paths, surface pressures, and skin deformations are evaluated in concert. Only with this aero-structural synchrony can a candidate architecture guarantee both the lift–to–drag gains promised by the morphing shape and the strength required to survive gust loads and manoeuvre envelopes. A typical workflow therefore begins by parametrising the target airfoil or wing section, setting performance objectives for each flight regime, and then allowing an optimisation loop to sculpt an internal compliant mechanism that can reproduce those shapes. This mechanism must be flexible enough to deliver the desired camber excursions yet stiff enough, once deployed, to behave like a conventional load-bearing spar. Simplicity also matters: replacing discrete flaps and ailerons with a continuous, hinge-free surface is worthwhile only if the resulting subsystem is lighter, less maintenance-intensive, and easier to integrate with existing power and control architectures. Finally, reliability and certification cannot be afterthoughts. Actuators must survive millions of duty cycles, skins must endure rain-erosion and fuel-temperature swings, and the entire morphing assembly has to interface cleanly with avionics, gust-load alleviation logic, and structural-health-monitoring hardware. In short, a successful morphing-wing design balances aerodynamic ambition with pragmatic constraints in structures, control, and systems integration—turning a novel concept into a flight-worthy asset.

The Air Force Research Laboratory (AFRL) tested a mechanical morphing system on the F-111, showcasing the advantages of morphing wings over conventional wings with seams and hinges [**4**][**5**]. However, the increased system weight and complexity diminished the performance gains. In DARPA's Phase 1 project, led by Northrop Grumman Corporation (NGC) in 1999, shape memory alloys (SMA) were used to actuate the morphing wing [**6**]. By 2001, during DARPA's Phase 2 [**7**], a piezoelectric driver replaced the low-bandwidth SMA actuator, significantly increasing the response rate of the active camber morphing wing.

In 2016, Flexsys tested its FlexFoil adaptive compliant trailing edge on a Gulfstream GIII Business Jet, replacing traditional control surfaces to assess the structural feasibility and durability of the FlexFoil system [**10**]. Other projects, such as CHANGE and SmartX [**14**], employed composite trailing edges directly actuated by actuators, simplifying the complexity of the morphing system. Additionally, the Fishbone Active Camber Wing project used a bio-inspired fishbone structure to achieve large-scale camber morphing while maintaining a constant airfoil thickness throughout the morphing process [**15**].

1.3 Challenges in Designing the Morphing Wing

Designing a high-performance morphing wing poses various challenges, including shape optimization methods, internal structure design, actuation control, material selection, and the integration of substructures. Recent advances in smart materials, fluid-structure interaction (FSI) analysis technologies, and optimization methods have made significant strides in addressing these challenges [**16**]-[**62**]. According to Vasista et al.[**2**], key challenges identified in previous literature include: 1) weight penalties associated with the morphing system, 2) the need for distributed, high-energy-density actuators, 3) structural design complexities, 4) control systems for actuation, 5) determining the target optimized shape, and 6) designing load-bearing, flexible skin. Additional desired capabilities in future morphing wing designs include large-scale morphing, multiple shape-change capabilities, high load-bearing capacity, high actuation rates, high-frequency response, low power consumption, reduced weight, and advanced materials.

1.4 The Optimization Method for Morphing Wing Design

Evolutionary algorithms are frequently employed in morphing wing design due to their computational efficiency, ability to identify optimal designs, and versatility in addressing various design objectives. Commonly used evolutionary methods include the Genetic Algorithm (GA) [**74**] and Differential Evolution (DE) [**77**]. For structural design in morphing wing applications, the Solid Isotropic Material with Penalization (SIMP) method has gained prominence

in recent years [**81**]-[**85**]. Its straightforward implementation allows it to accommodate a wide range of objective functions, such as the minimum compliance problem and compliant mechanism design. A variety of extended formulations and techniques have been developed to improve the design quality and manufacturability.

1.5 Research Novelty and Contributions

(1) **Segmented Bezier–PARSEC parameterization with Differential Evolution (DE)** – A modified BP framework allows the leading and trailing edges to be optimized independently while the mid-chord remains fixed, maintaining structural continuity, yet allowing large camber excursions with controllable curve-length change.

(2) **Novel real-time shape-error metrics and adaptive filtering** - Two formulations of displacement error (dynamic vertical plan and dynamic perpendicular line) paired with an area-adaptive density filter accelerate convergence and suppress mesh dependency during topology optimization, producing hinge-free and manufacturable load paths.

(3) **Irregular mesh tailored to airfoil curvature** - Adopting an unstructured curvature-aligned mesh captures boundary layer pressure gradients and geometric nuances more efficiently than conventional structured grids, yielding higher-fidelity aerodynamic solutions.

(4) **Take consideration of minimum compliance formulation** - By taking consideration of the minimum compliance problem ensure that the final architecture achieves a suitable stiffness to improve reliability under flight loads and mitigate excessive deflection.

(5) **Seamless topology-to-solid conversion workflow** – The density map from topology optimization is automatically converted into a smooth CAD surface with spline smoothing, so the design can go straight to CAD model and FEA without manual redrawing.

1.6 Thesis Outline

The current research on active camber morphing wings aims to design a shape control of morphable 2-D wing, using SIMP method to find the optimal material distribution. This work employs Differential Evolution as the shape optimization method and the SIMP method [**81**] for structural optimization of the compliant mechanism to achieve the target morphing shape and minimum compliance. A modified parameterization approach, based on the PARSEC-Bezier method [**79**], is introduced to capture the design features of the morphing wing based on the multi-objective function. The design parameters are optimized using the Differential Evolution method. Additionally, the designed active camber morphing wing is tested using commercial software to validate the method accuracy and efficiency.

This thesis is structured into five chapters, which are as follows:
Chapter 2: A literature review of the background and advancements in morphing wing technology. This chapter covers recent morphing wing design projects and the methods implemented over the past few years.
Chapter 3: Airfoil Shape Parameterization and Optimization. A baseline airfoil is selected for parameterization and optimization. The shape is fitted using the Bezier-PARSEC method and divided into three segments to optimize performance.
Chapter 4: Structural Optimization of Active Morphing Wings. Chapter 4 will use shape optimization results from Chapter 3 to do structure design. The SIMP method is applied to determine the optimal material distribution, minimizing the difference between the target and actual geometry while reducing compliance through the introduction of a weighting factor.
Chapter 5: Conclusion and Future Work. A summary of the contributions made in this work, along with proposed future improvements to the current design and optimization strategies.

CHAPTER 2

Literature review

The challenges in designing active camber morphing wings have been presented in the introduction chapter. For preliminary design, the main challenges are airfoil shape optimization and structural optimization. For further integration of the system, the main challenges are the actuation system, the fabrication of the morphing wing and the balance between performance and weight penalty. This literature review consists of the active camber morphing wing techniques, the development of significant projects and the updates in design and optimization methods. The review begins with the background of previous projects in the last 25 years and followed by analysis methods reviews. The review ends with the present methods attempted in morphing wing design, which could be a new starter for this thesis research.

2.1 Background of Active Camber Morphing Wing Research

The active camber morphing wing is realized by adjusting out-of-plane parameters, specifically the camber, which alters the shape of the airfoil or parts of the airfoil, such as the leading and trailing edges. Various researchers and institutions have explored optimal combinations of morphing wing substructures to achieve design targets while balancing the trade-offs

associated with increased weight and complexity. Although multiple morphing concepts have been developed, the practical application of morphing wings still presents numerous challenges.

2.1.1 Mechanical Morphing Structures with Hinges and Seams

The AFTI/F-111 Mission Adaptive Wing (MAW) project, conducted by NASA and the U.S. Air Force in the 1980s, introduced a wing design that allowed for variable camber at the leading and trailing edges, replacing the supercritical wing on the F-111A aircraft [**4**]. The MAW was actuated by a conventional mechanical system with a flexible airfoil skin shown in figure 2.1 and 2.2. In this design, the load was transferred from the airfoil skin to the internal mechanism, with the skin not bearing any load in the chord-wise direction. This variable camber wing demonstrated improved performance across subsonic, transonic, and supersonic flight conditions, achieving a verified drag reduction of 7% at the design point during cruise and over 20% at off-design points [**5**]. However, the complexity of the mechanical structure increased the system's weight, spatial requirements, and control system intricacy, thereby diminishing the advantages of the design.

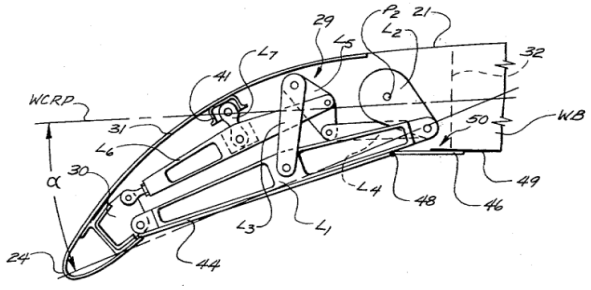

FIGURE 2.1. AFTI/F-111 MAW high lift configuration[**4**]

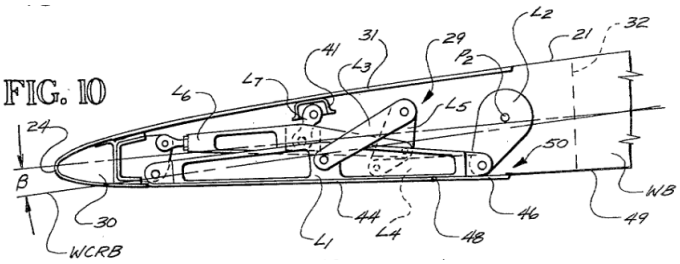

FIGURE 2.2. AFTI/F-111 MAW high velocity configuration[**4**]

The DARPA Smart Wing Program was spearheaded by a team led by Northrop Grumman Corporation (NGC) and included two phases of development, incorporating significant optimization processes compared to conventional wing control systems. In Phase 1, the Smart Wing utilized shape memory alloys (SMA) to control the twist of the control surfaces, allowing for optimized airfoil shapes under varying flight conditions [**6**]. In Phase 2, the SMA-based actuation system was replaced with a piezoelectric motor actuator, enabling higher bandwidth and qualifying the system for high-performance aircraft requiring rapid maneuvering responses [**7**].

The actuation system in Phase 2 consisted of an eccentuator driven by a piezoelectric motor, integrated into a honeycomb segment supporting a silicone skin shown in figure 2.3 and 2.4. The second wind tunnel tests revealed a 10.5% improvement in aileron effectiveness, as measured by the rolling coefficient. Additionally, the wing was able to generate the same lift with a smaller aileron deflection, resulting in reduced drag and faster response times in achieving the desired shape. Despite these advancements, challenges remain in aeroservoelastic behaviour, flexible structure selection, durability, and systems integration, including feedback control and compact power supplies, all of which require further development [**6**][**7**].

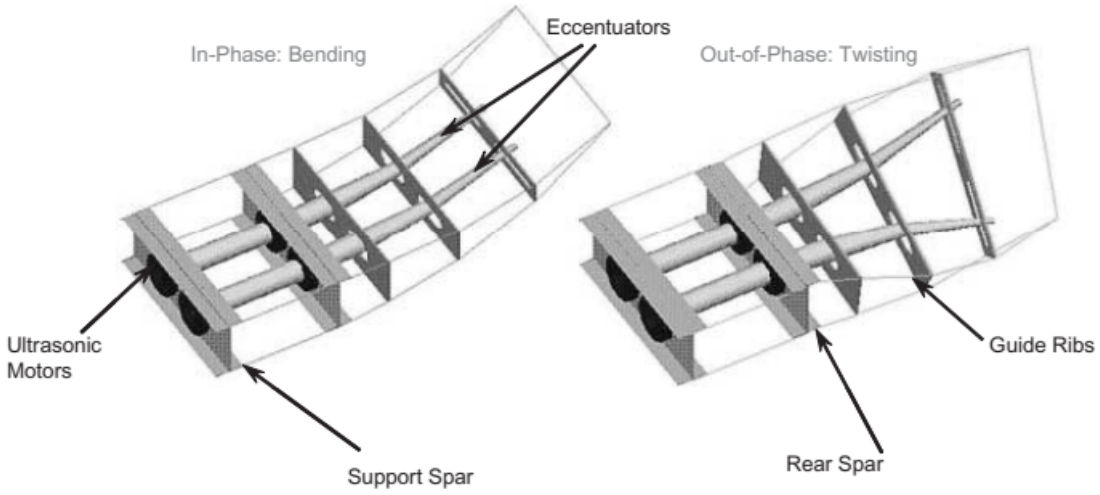

FIGURE 2.3. DARPA Smart Wing eccentuator design[**6**]

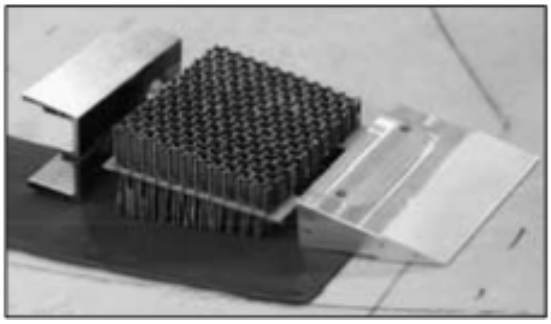

FIGURE 2.4. DARPA Smart Wing assembed segment[**6**]

The German Aerospace Center (DLR) initiated a project that developed a novel compliant, finger bone-like structure for the Airbus A340-300 Fowler flap [**8**]. This design features a combination of flexible and rigid segmented structures arranged in sequence, as shown in Figure 2.5 and 2.7, with each subunit rotating around a pin. The system can be actuated either by a single large actuator driving the entire structure or by multiple distributed actuators. The skin is vertically attached to the actively adjustable ribs via a linear slide bearing, allowing the skin to follow each rib segmentally (see Figure 2.6).

The test model incorporates both aluminium and carbon fibre, with the latter material providing weight savings while maintaining stiffness. The rib structures are designed to handle different aerodynamic conditions through three distinct types of functional configurations. Parameter variation studies indicate that the optimal configuration consists of a four-segment or five-segment rib design. As the design focuses on improving the Fowler flaps of civilian transport aircraft, aerodynamic studies suggest that the optimal camber variation begins at 90% chord.

Compared to earlier mechanical structures, the flex flap system introduces a continuously variable shape-morphing feature. The complex kinematics allow the rib to be positioned along any desired median line to achieve the required shape. The formulation for calculating the rib geometry is presented in a general form, making it adaptable for various geometrical and aerodynamic requirements.

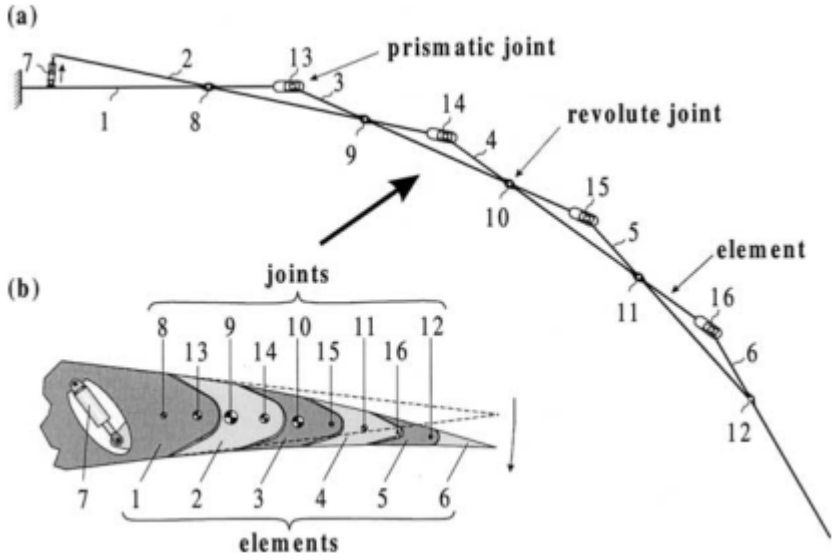

FIGURE 2.5. DLR active deformable ribs[**8**]

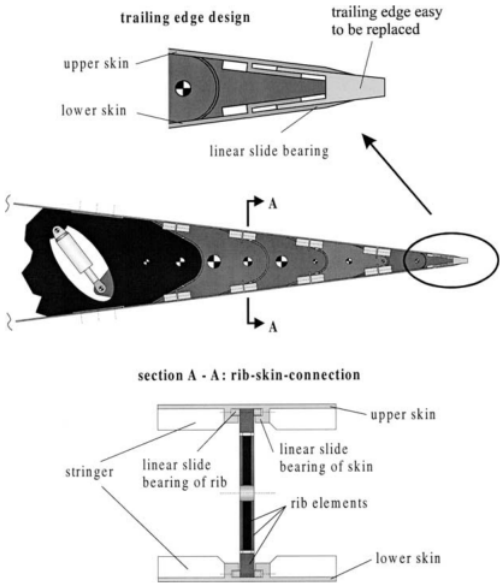

FIGURE 2.6. DLR skin design[**8**]

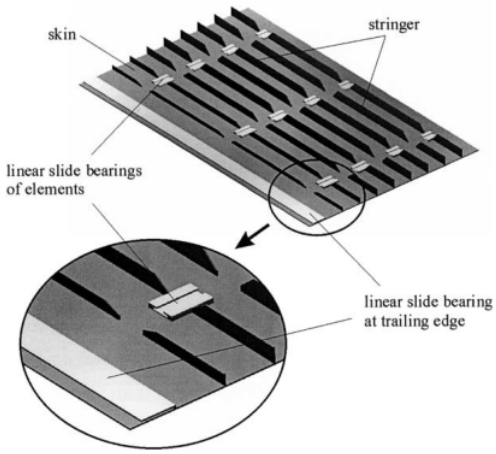

FIGURE 2.7. DLR skin with linear slide bearings[**8**]

2.1.2 Bionic inspired morphing structure design

Inspired by NASA's fishbone concept, Woods and Friswell et al. proposed a Fish Bone Active Camber (FishBAC) morphing concept that realizes positive and negative camber

changes and can deform on a large scale[**15**]. This concept consists of four main parts: 1. Compliant skeleton 2. Pre-tensioned EMC skin 3. Non-backdriveable antagonistic tendon drive 4.Non-morphing main spar. Figure 2.8 shows the Fish BAC design concepts with its main components.

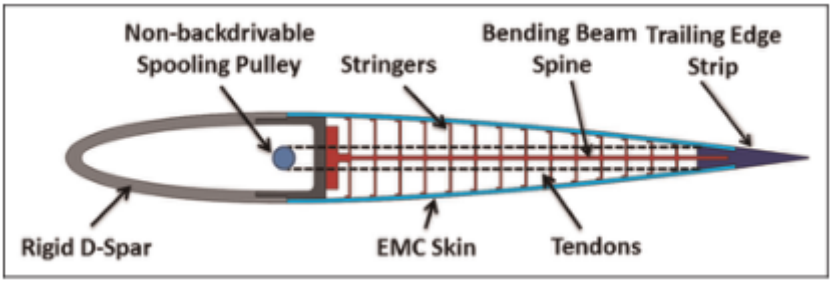

FIGURE 2.8. Fishbac concept overview[**15**]

The compliant skeleton is a highly anisotropic fish spine-like structure. It is set horizontally along the chord-wise direction, taking the load from the airflow through the stringers. This structure has low bending stiffness in the chord-wise direction but high bending stiffness in the span-wise direction, so the size and output of the actuation system can be reduced. The pre-tensioned skin is made of elastic material, which is supported by stringers to achieve strain along the surface of the airfoil. To counteract the effects of a high Poisson's ratio, high-modulus fibres are added to achieve an effective zero Poisson's ratio composite. The EMC skin is pre-stretched before installation to overcome the buckling that occurs when the skin is compressed. At the same time, this can also increase the stiffness of the out-of-plane, so that the vertical deformation of the skin under higher loads is smaller. Non-backdriveable antagonistic tendon drive an actuation system consisting of an actuator, non-backdrivable worm and worm gear pair and tendons. Two tendons are arranged above and below the spine, and the ends of the spine are pulled through the actuator to achieve positive and negative morphing. Worm and worm gear pair can control the shape of the airfoil under frequently changing air loads to reduce power requirements. The type of actuator can be any actuation system that can provide sufficient power. The non-morphing D-spar is a rigid structure that carries the primary load from the air and morphing wing system.

2.1.3 Seamless and hingeless morphing structure design

The smart X is a project ongoing with a highly integrated system by the TU Delft. It absorbed the idea of Translation Induced Camber (TRIC) from the EU FP7 CHANGE project [**14**]. It integrates multiple distributed morphing sections by using elastomer material to connect each morphing modular. With a pair of actuators inside the wing box, the individual modular is controlled directly by applying loads on the lower skin. The twin actuators in each individual morphing modular can realize twist morphing by using opposite input loads. Figure 2.9 shows the general and sectional details of the smart X concept. This project has an innovative concept that connects the entire trailing edge to ensure the continuity of the structure, which maintains the aerodynamic efficiency in real (3D) cases. The Smart X project coupled the MD NASTRAN and XFOIL to do a nonlinear structural analysis and a 2D aeroelastic analysis. It aims to find the desired morphing design and quickly conduct an aerodynamic assessment of the wing. The NASTRAN SOL200 optimization solver was used to optimize the design parameters of the structure that can achieve the target aerodynamic shape. Due to its simple structure, the excess space in the wing box can also be used for other purposes such as putting more sensors or avionics. However, the disadvantage of the simple structure could be the increased required actuation force, because the lack of control of the middle section of the trailing edge will result in a large stiffness design for the skin, which simultaneously increases the required load to achieve the target shape.

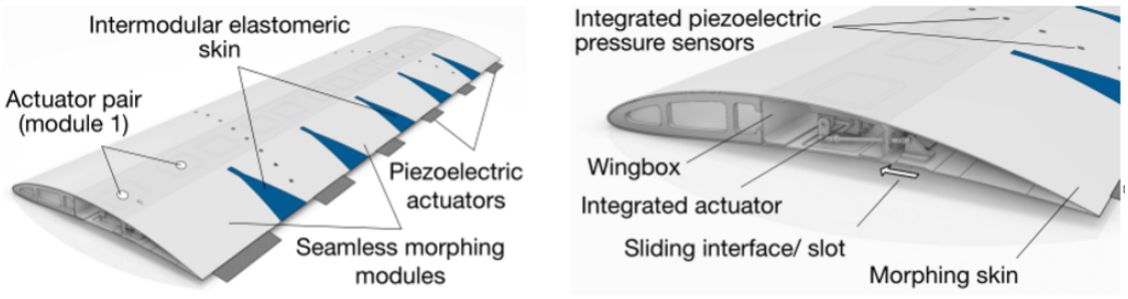

(a) Detailed view of SmartX wing. **(b) Close UP of the TRIC morphing module**

FIGURE 2.9. Smart X concept overview [**14**]

FlexSys mission-adaptive compliant wing is a seamless and hingeless design that was promoted in 2000 [**9**]. The target shape is to maximize the L/D ratio at different flight conditions with various flap deflections. It promoted the idea of designing the internal structure to control the target shape while controlling the wing stiffness to bear the wing loadings and survivability constraints. Kota et al.[**10**] used the FlexSys Inc. proprietary Continuous Shape Generation (CSG) software to design compliant structures that meet desired design targets. The current actuators such as piezoelectric, SMA and Terfenol-D all have problems with displacement or bandwidth. The compliant structure is able to deform as an entity with the stress distributed averagely without concentration. Then the power required from the actuator is minimized. The compliant structure plays the role of force or motion transmission, motion guidance, shape morphing, and/or energy storage and release. The Flexsys trailing edge flap was fabricated and tested at the Ohio State University wind tunnel facility in 2002 (figure 2.10). The test results were compared with conventional flaps and showed a better drag reduction feature.

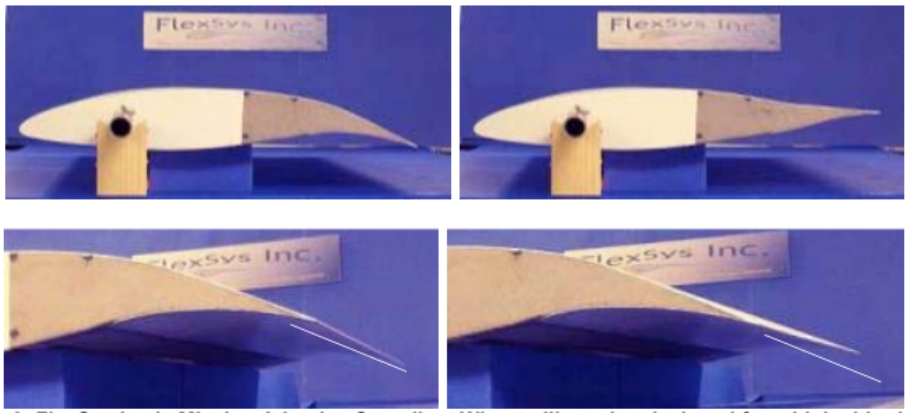

FIGURE 2.10. Flexsys MACW with +/-10 degrees flap deflection and 3 degrees twist [**10**]

The system for designing the structure is required to do FEA. Compared to a conventional hinged mechanism, the compliant structure can be easily fabricated and assembled, eliminating the complexity and space of the integrated system. The limited displacement of piezoelectric stack actuators can be amplified by using a compliant mechanism. To make a balance between maximum stiffness corresponding to external loads and minimum stiffness corresponding to

the desired deformation, the flexibility of the compliant structure is considered carefully to meet the requirements of both actuator energy and aeroelastic and structure constraints. The LE model test has shown a slightly increased weight model (7%) without optimization, which proves the feasibility of the concept. The TE concept required various shapes of the deflecting section, which shows a development of the concept from an all-moving/twisted morphing wing. The wind tunnel test of the various trailing edge model shows an improved drag polar, which has a smaller increase of drag coefficient than a conventional mechanism under the high angle of attack conditions. One novel thing mentioned is the high-frequency vortex generators, which are used to control flow separation. It extends the flow control authority under transonic conditions.

In 2006, a new mission-adaptive compliant trailing edge (Figure 2.11) used in conjunction with a natural laminar flow airfoil was fabricated and tested on the Scaled Composites White Knight aircraft [**10**]. The design target was to extend the laminar boundary layer over the wing surface for various lift coefficient conditions for endurance aircraft. The flight test results showed that the laminar flow could be maintained at about 60% of the chord for most of the lift range. In addition, the range can be extended over 15% by continuously optimizing the lift-to-drag ratio during the flight. The MACW wing can achieve 40% more control authority and 25% reduced drag than a conventional wing [**11**].

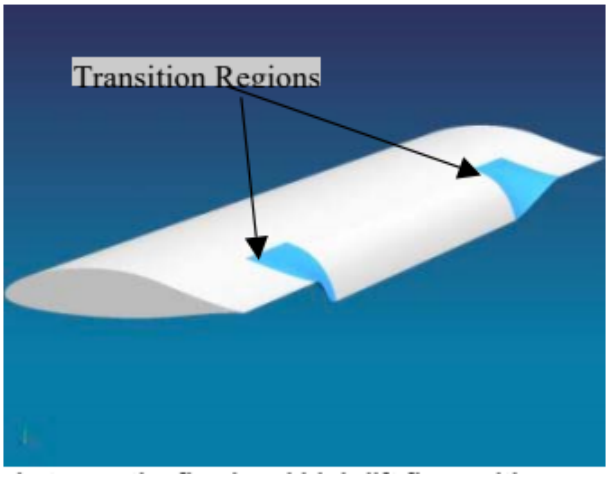

FIGURE 2.11. Flexible transition composite compliant structure [**10**]

Figure 2.11 shows a smooth transition between the fixed wing and flexible flap which uses a compliant structure. It reduces the drag and noise caused by the turbulent flow on the discontinuous surface. The trailing edge flap was fabricated by aluminium but was proposed to be fabricated by composite material in the future, which will be a significant point in this thesis. It can also reduce the noise produced by turbulent flow and flaps during landing.

Before doing the flight test on the Scaled Composites White Knight aircraft, the MACW model shown in Figure 2.12 was tested in the Wright Patterson Air Force Base's Subsonic Aerodynamic Research Lab (SARL) facility to test its performance and safety factor. It was operated under 240 psf loading at flap rates up to 30 degrees/sec driven by two electrical servo motors. The upper surface was fabricated by aluminium and polymer composition, while the lower surface has an additional composite reinforced panel to allow the lower surface to expand and contract during morphing.

FIGURE 2.12. MACW aluminium model installed in SARL facility [**10**]

Figure 2.13 shows the installation of the MACW wing under the Scaled Composites White Knight vertical stub pylon. The flight test proved that the pressure distribution, lift, preliminary drag and moment could be controlled well and meet the prediction. The most significant result was that the drag coefficient does not vary a lot for different lift coefficients, with about 40% drag coefficient compared to the conventional flap. For long-endurance military aircraft,

the implementation of drag minimizing mechanism has significant improvements in fuel efficiency. The MACW did not have any limitations to be operated under high altitude, low-temperature environments, which can also be implemented in commercial aircraft. The patent published in 2008 showed some design concepts of the adaptive compliant wing design[**12**].

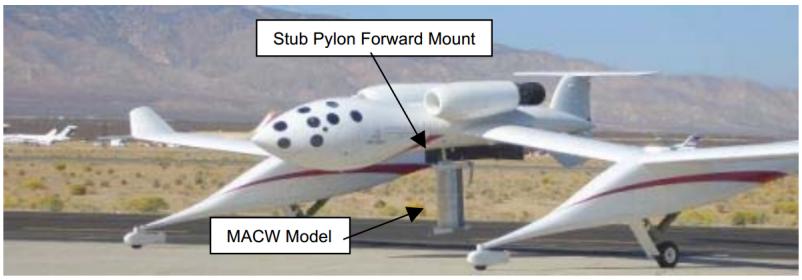

FIGURE 2.13. MACW installation under the Scaled Composites White Knight[**10**]

From Nov. 2014 to Apr.2015, FlexSys, Inc. cooperated with the U.S. Air Force Research Laboratory (AFRL) to do a flight test of the Adaptive Compliant Trailing Edge (ACTE) on a Gulfstream GIII Business Jet[**13**] for 23 times. The Flexfoil on each wing is a 19-foot span-wise flap, that can realize the change in camber and twist from -9 to 40 degrees. It can be operated under a 2G maneuver load and 384 psf of dynamic pressure.

FIGURE 2.14. Flexfoil tested on the Gulfstream III business jet [**12**]

Compared to some modern commercial aircraft that use ailerons and flaps to reduce the induced drag during cruise, the Flexfoil can provide more accurate morphing of the control surfaces with seamless and hingeless continuous deflections. Figure 2.14 shows the continuous transition region made by the compliant composite material mentioned previously. The CFD and fatigue tests were conducted on the full aircraft to validate and update the Adaptive Compliant Trailing Edge structural dynamics model. The weight penalty of the Adaptive Compliant Trailing Edge was lower than 10% compared to the current conventional control surface. The power required to operate the Adaptive Compliant Trailing Edge was 10-20% higher than the conventional flap, while the power required for gust load alleviation was much higher because of the high rate of twist (30 degrees/second). A variety of types of data for different disciplines have been generated for analysis such as structures, dynamics and aerodynamics. The Flexsys and Boeing team was authorized by AFRL to do a further test of the Flexfoil on a KC 135 test aircraft to validate its fuel-saving ability.

2.2 Compliant mechanism design and analysis methods

2.2.1 The development of compliant mechanism design methods

Previous projects such as the Flexfoil from Flexsys have proven the application potential of compliant mechanisms in morphing wings, which realized continuous shape-changing of the control surfaces and maintained enough structure stiffness.

The compliant mechanisms (CMs) are mechanisms that transfer input load to displacement outputs and force outputs. It is a seamless and hingeless mechanism without the demand for lubrication at the joints in operation. The concept of the compliant mechanism was first presented by Buens and Crossley in 1968, that the kinematics of flexible-link mechanisms is assumed to have the large deflection member transverse a path with a radius of 5/6 of the member length[**16**]. The compliant mechanism can be divided into a partially compliant and a fully compliant mechanism[**17**]. The fully compliant mechanism can also be divided into a distributed compliant mechanism and a lumped compliant mechanism shown in Figure 2.15.

FIGURE 2.15. Definition of distributed compliant mechanism and lumped compliant mechanism[**18**]

For a very long time, the design of the compliant mechanism was based on experience without a large number of calculations. With the development of computers, numerical methods can be used to solve complex problems related to compliant mechanism designs. Sigmund et al. has started to study mechanisms with flexible segments since 1997 [**18**]. With the improvement of the topology optimization method, it has become one of the main methods of compliant mechanism design. The optimization of the structure consists of shape optimization, size optimization and topology optimization. Compared to the kinematics-based method such as Freedom and Constraints Topologies (FACT) method [**23, 24**] and the Rigid Body Replacement method [**25**]-[**31**], the topology optimization method does not require an external program to do shape optimization and size optimization. The building blocks method is to use a known equivalent system of pin joints, rigid links and torsional springs to replace the flexible segment [**22**]. The topology optimization method optimizes the material distribution in the design domain, which meets the objective function with given boundary settings [**18**][**32**]-[**37**]. The program of topology optimization is combined with a Finite Element Analysis (FEA) section to analyze the structure optimized during the optimization process quickly. The topology optimization method can be divided into discretization topology optimization [**38**]-[**44**] and continuum topology optimization [**18, 47, 48**]. The representative method of discretization topology optimization is the ground structure method, which has been introduced in [**45, 46**] with the consideration of flexibility and stiffness by using a weighted sum. Continuum topology optimization is a new and fast-developed method recently, Zhu et al. provided a review of the continuum topology optimization to help researchers systematically understand its application to CMs [**49**].

The are a number of methods have been developed to design CMs such as the homogenization method [**50**], the SIMP method [**51, 52**], the Level Set Method [**53, 54**], the ESO method [**55, 56**], phase field methods [**57, 58**], the MMC method [**59, 60**], GA [**61, 62**] and MIST (Moving Iso-Surface Threshold)[**63**].

2.2.2 The topology synthesis of displacement inverter and path-generation mechanism

The objective functions formulated for the compliant mechanism are usually displacement, MSE (mutual strain energy), SE (strain energy), output work, geometrical advantages, mechanical advantages, mechanical efficiency and the combination of the above parameters. Nishiwaki et al. [**47**] promoted the objective function with a combination of MSE and SE to find the optimized result that maximizes the mutual potential energy and minimizes strain energy simultaneously. Larsen et al. promoted an objective function based on geometrical advantages (GA) and mechanical advantages(MA) and returned the best structure. It can obtain continuum-type compliant mechanisms with multiple input and output degrees of freedom [**48**]. Pedersen et al. [**64**] formulated a new objective function, which controls the path of the compliant mechanism before it reaches its final position. The objective function is represented as an error function to minimize the error between the target and the actual location for M precision points. This strategy is worth talking about since it has the potential to be implemented in multi-step control of the behaviour of compliant mechanisms. The objective function is shown in equation 2.1,

$$\Phi = \sum_{i=0}^{2} \alpha_i \sum_{m=1}^{M} \left[\mathbf{u}_{\mathrm{out},m,i} - \mathbf{u}^*_{\mathrm{out},m} \right]^2 \tag{2.1}$$

where the $u_{out,m,i}$ and $u^*_{out,m}$ are the actual displacements and target displacements vectors at the output ports. M is the number of intermediate steps and α_i are the weighting factors for each step. To build the load path between input and output ports, the counter load $P_{m,i}$ (i= 0, 1, 2) is applied at the output port. For i = 0, there is no counter load applied but only the input load. For i = 1 and 2, the counter loads are applied opposite to and perpendicular to the input load, but with a much lighter weighting factor. The strategy for determining the scale of the

counter load is as follows:

$$P = \frac{1}{k} R_{\text{in}}^{*} \frac{\Delta u_{\text{in}}}{\Delta u_{\text{out}}} \tag{2.2}$$

where k = 2 can result in the best results from tests. The compliant mechanism design is expected to be analyzed by using nonlinear FEA since the displacement is large and the linear FEA cannot provide suitable results. By using the adjoint method, the sensitivity of the objective function can be obtained. Figure 2.16 shows the design domain for the force inverter and Figure 2.17 shows the results of synthesized force-inverter mechanisms by using linear and non-linear finite element analysis.

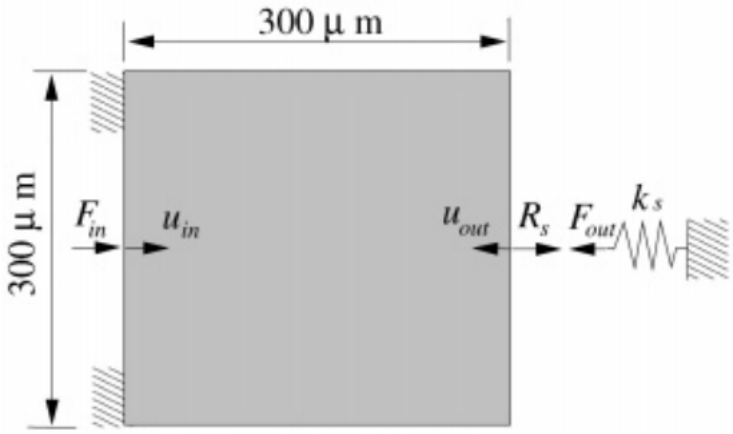

FIGURE 2.16. Design domain for the force inverter[**64**]

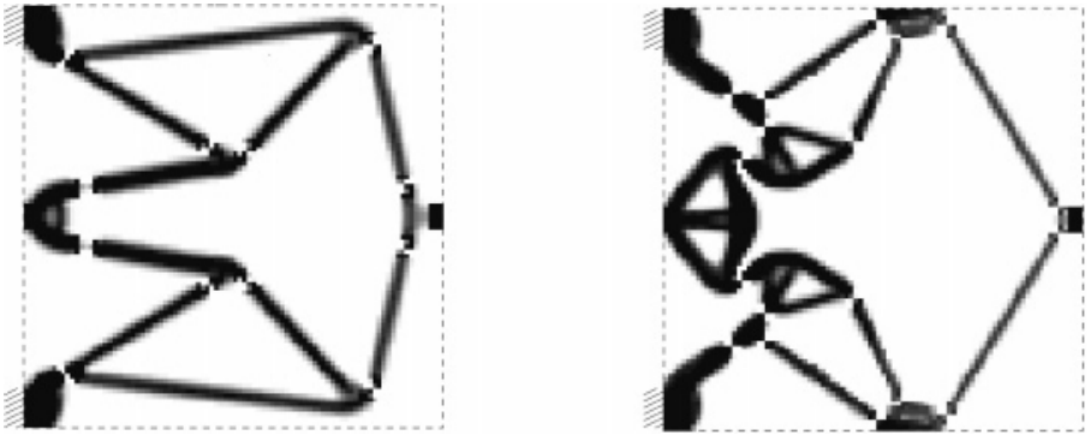

FIGURE 2.17. synthesized force-inverter mechanisms by using linear and non-linear finite element analysis[**64**]

These two designs have significant differences caused by the FEA method applied. If using the linear FEA during the design process, the final displacement is 48.6 μm using linear FEA and 16.5 μm using non-linear FEA. If using the non-linear FEA during the design process, the final displacement is 9.7 μm if using linear FEA and 42.1 μm if using non-linear FEA to measure the displacement. The resultant mechanisms after displacement are shown in Figure 2.18 and 2.19, showing the issues using linear FEA to do compliant mechanism design.

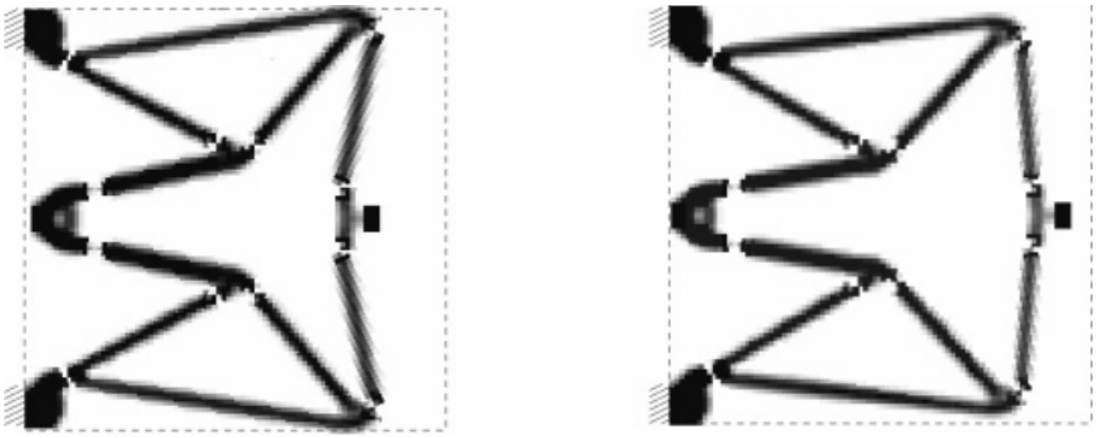

FIGURE 2.18. Force-inverter mechanism designed using linear FEA and analyzed using linear(left) and non-linear(right) FEA[**64**]

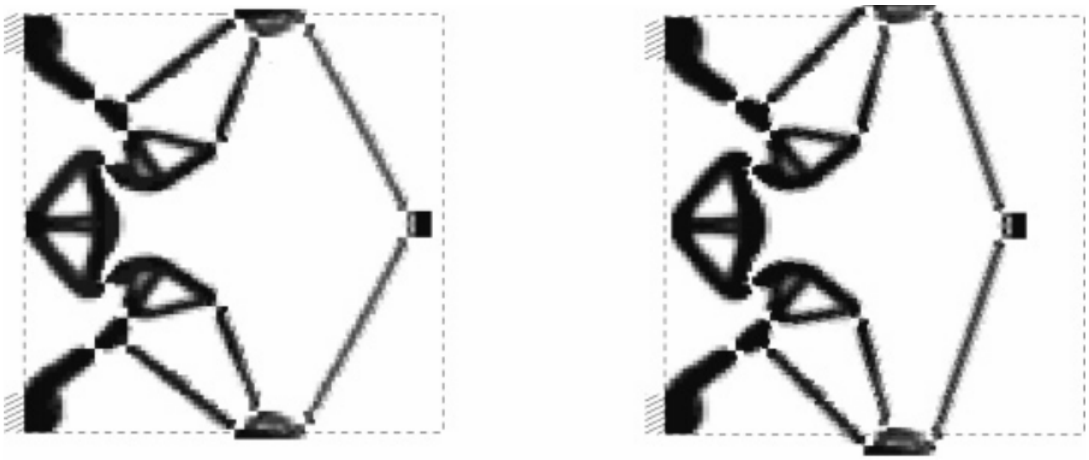

FIGURE 2.19. Force-inverter mechanism designed using non-linear FEA and analyzed using linear(left) and non-linear(right) FEA[**64**]

By observing the results, the left one in Figure2.18 has an unreasonable displacement, where the output port goes beyond the maximum possible displacement. It should be locked when

the output port is in the same vertical line with the upper and lower bar connected to the output port. If change the linear FEA to non-linear FEA, the result shown in the right one in figure 2.18 make sense but with a much smaller result. By observing the results that were designed using non-linear FEA, the left one in Figure 2.19 looks blocked by the upper and lower boundary of the design domain without the large rotations in the right one. Then using non-linear FEA during the design process and analysis could be a mandatory requirement for designing a compliant mechanism with large displacement. For the path-generation compliant mechanism, the non-linear FEA is also suggested. The consideration of path generation could bring two benefits: 1) Control of the behaviour of the compliant mechanism during shape-changing. 2) Make the input and output have a linear relationship to be accurately controlled using the actuator. Figure 2.20 shows the input-output displacement relationship by using 2 and 5 precision points during the design process.

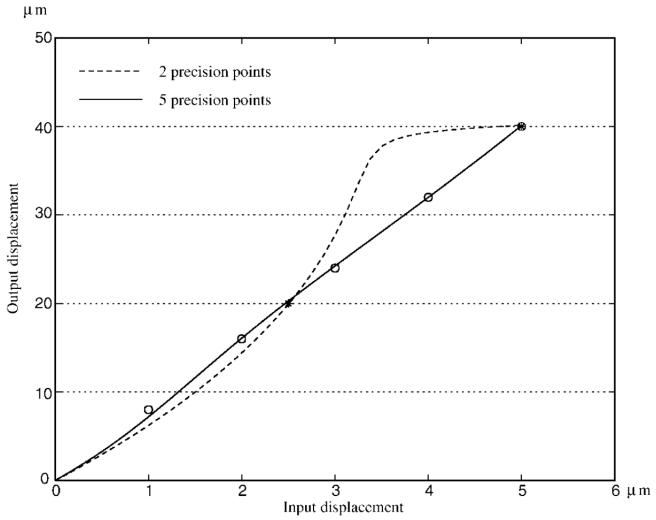

FIGURE 2.20. input-output displacement relationship[**64**]

2.2.3 The objective formulation and implementation of topology optimization in compliant morphing wing

Shili et al. [**65**] used GA(Genetic algorithm) optimization to design a compliant trailing edge on a discretized design domain shown in figure 2.21. Its objective function is in the form of LSE (least square error) to minimize the difference between target and actual displacements.

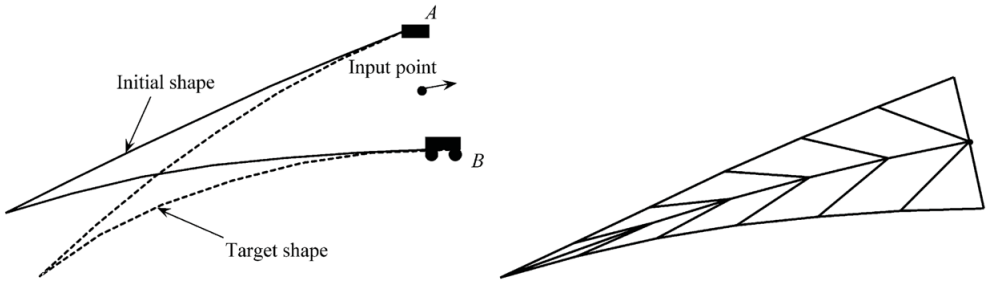

FIGURE 2.21. Discretized design domain and boundary conditions of the trailing edge[**65**]

Zhang et al. designed the variable camber morphing leading and trailing edge internal structure by using Meshless-based topology optimization updated by the method of moving asymptotes (MMA) and non-linear FEA [**66**]. The skin is designed by GA using geometrically nonlinear analysis of the beam modal in ANSYS. The objective function of the internal structure is to maximize the displacement, while the objective function of the skin is to minimize the displacement error between target and actual displacements. Figures 2.22 to 2.24 show the example of their leading edge skin and structure designs. The spring model mentioned by Sigmund in [**18**] is used in the internal compliant mechanism design to simulate the resistance from the skin. It is calculated by:

$$k^i_{out} = F_i / u^i_{out} \tag{2.3}$$

where F_i is the output force of the compliant mechanism (same as the input force of the skin), u^i_{out} is the displacement at the output port (same as the input displacement of the skin).

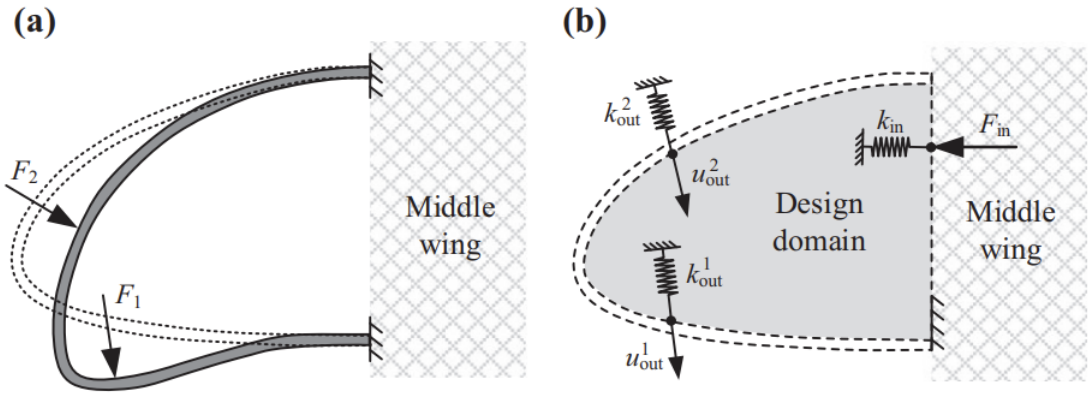

FIGURE 2.22. Design domain of the leading edge skin and internal compliant mechanism[**66**]

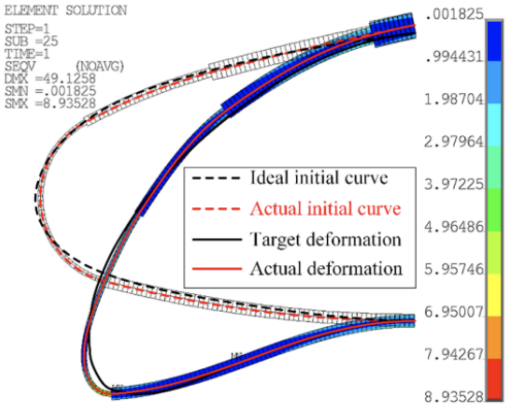

FIGURE 2.23. Deformation of leading-edge skin[**66**]

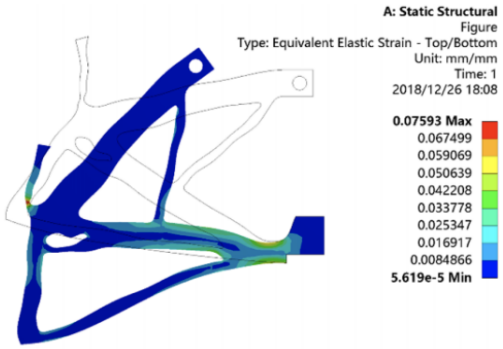

FIGURE 2.24. Deformation of leading-edge compliant mechanism[**66**]

Li et al. designed a variable camber leading-edge with concentrated flexibility based on the five-bar mechanism [**67**]. The skin design used the GA by minimizing the displacement error between the target and actual displacements during the first bending process. For the internal structure design, the optimized objective is to minimize the strain energy of the original and optimized skin when the driving points are fixed.

Tong et al. made some efforts on the compliant adaptive wing with composite materials [**68**]-[**70**]. The objective functions are formulated to minimize the LSE (least square error) to control the difference between target and actual displacements. The SIMP method is used to design the compliant structure, while the skin is defined as a fixed design domain. The virtual load method is used to calculate the sensitivity of the objective function. The design problem is expressed as:

Find : $\boldsymbol{X} = [x_1, x_2, \ldots, x_N]^{\mathrm{T}}$

$$\text{Min} : f(\boldsymbol{X}) = \sum_{l=1}^{n} \sqrt{\left(u_{x,l}(\boldsymbol{X}) - u'_{x,l}\right)^2 + \left(u_{y,l}(\boldsymbol{X}) - u'_{y,l}\right)^2}$$

$$\text{s.t.} \begin{cases} \boldsymbol{KU} = \boldsymbol{F} \\ \boldsymbol{kV} = \boldsymbol{L} \\ \sum_{i=1}^{N} x_i \bar{v}_i \leqslant hV_0 \\ 0 < x_{\min} \leqslant x_i \leqslant 1 \end{cases}$$

Where X is the design parameter density (vector) from 0-1 in the SIMP method, K is the global stiffness matrix, U is the global displacement field, L is the adjoint load vector, v_i is the element volume, h is the volume fraction constraint, V_0 the total volume of the design domain which is 1, F is the input force, V is the adjoint displacement vector. The OC, MMA and GCMMA were attempted to update the design variables.

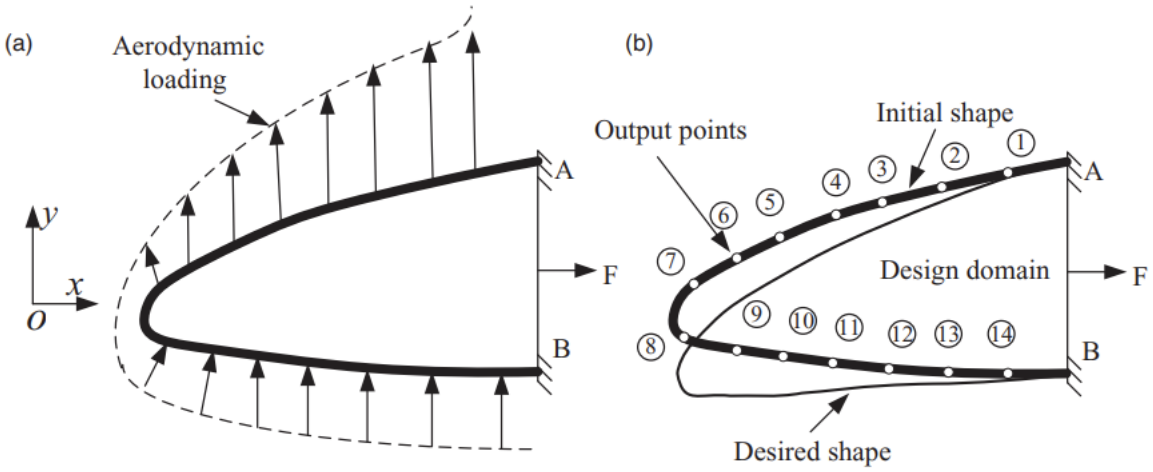

FIGURE 2.25. Design domain of the leading edge compliant mechanism[**69**]

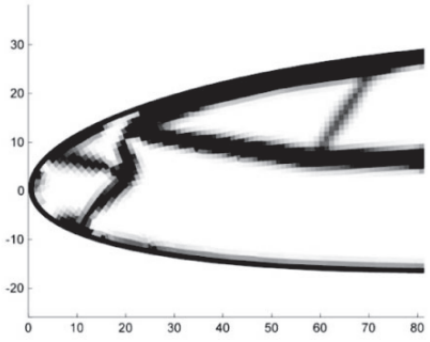

FIGURE 2.26. Topology shape of the leading edge[**69**]

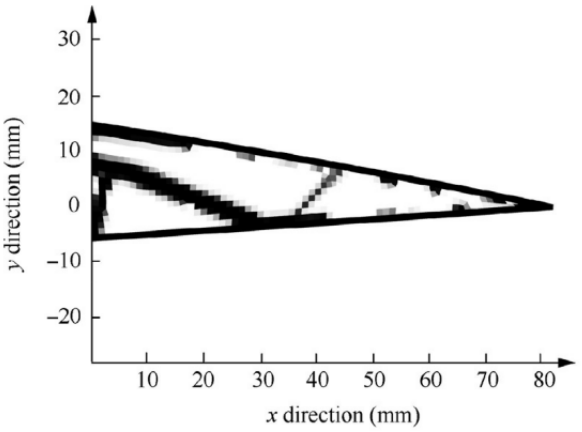

FIGURE 2.27. Topology shape of the trailing edge[**70**]

Figure 2.25 shows the example of the leading edge design domain, Figures 2.26 and 2.27 show the shape topology shapes of the leading and trailing edge.

The aerodynamic pressure is replaced by concentrated forces applied on the boundary of the design domain. The numerical results show good convergence of the algorithm developed and acceptable error of the displacement. However, the experiment of the fabricated model sometimes needs modification of the boundary settings to achieve desired displacement errors.

Building on the comprehensive survey of morphing strategies by Li et al. which classifies planform, camber, twist and span-wise concepts and compares numerical, analytical and experimental approaches[**71**]—the last decade has delivered three pivotal breakthroughs: (i) high-fidelity fluid–structure-interaction solvers that resolve large, transient deformations; (ii) machine-learning surrogates that slash optimisation time while retaining prediction error; and (iii) additive-manufactured compliant mechanisms that translate complex kinematics into gapless, lightweight structures. Collectively, these advances are steering the field toward integrated, real-time and production-ready morphing wings.

2.3 Knowledge Gaps and Research Positioning

Although progress has been substantial, several intertwined challenges remain unresolved and motivate the present thesis:

(1) **Truly coupled aero-structural optimization**: Aerodynamic and structural designs are often treated sequentially, risking stress or deflection violations once disciplines interact.
(2) **Mesh fidelity versus computational cost**: Structured grids struggle with sharp airfoil curvature, whereas fully unstructured meshes can be prohibitively expensive; a systematic, curvature-aligned irregular mesh has yet to be mainstreamed.
(3) **Topology-to-CAD translation**: Density-based outputs seldom pass directly into CAD/FEA; manual surface reconstruction slows the loop and introduces errors.
(4) **Multi-objective trade-offs**: Lift, drag, weight, stiffness and energy draw the design in competing directions; few frameworks optimize these objectives concurrently across the flight envelope.

(5) **Actuation integration**: Embedding shape-memory alloys, piezo layers or tendon drives within slender wings poses packaging and reliability challenges still handled empirically.

(6) **Fatigue durability** : Continuous morphing skins endure millions of cycles, while the design and test of morphing wing skin are still challenging topics.

2.4 The shape parameterization and optimization method

To conduct the optimization of the airfoil shape, a suitable parameterization method should be designed, so that the parameters can be used as design parameters in optimization algorithms. The typical method to do this is to use polynomials to reduce the degree of freedom of the curve while reducing the computation time but maintaining enough accuracy. Some well-known shape parameterization methods are the Bezier curve, B-spline or NURBS, PARSEC and Bezier-PARSEC (BP). The BP parameterization was developed by Rogalsky et al. to accelerate the convergence of airfoil shape representation [**72**][**73**].

The design parameters of BP can be further optimized using the DE (Differential Evolution) algorithm [**77**], which is a kind of GAs [**74**], developed recently that is particularly effective for aerodynamic optimization [**75**][**76**]. The structure of DE is similar to other population-based searches, with NP (number of population) and D (dimensions). The suggested population is equal to 10 times D, which makes it an effective search [**77**]. The initial vectors with NP and D-dimensions recombined by using a mutation and crossover operation to recombine a trial vector. A competition happens between the original vector and the trial vector, and the better one will be maintained for the next generation. The mutation is a modification of the current vector based on a perturbation. The traditional GA use a pre-determined probability distribution to apply the perturbation, while the DE use the population as the source of perturbation to make the scale of perturbation close to the topology of the objective function [**73**]. DE uses a weighted differential, which is the difference between two random numbers in the original vector, to perturb other vectors. A difference is then multiplied by a

weighting factor F to control the mutation operation, and F=0.85 is a recommended value. The DE algorithm and a modified BP parameterization will be introduced in Chapter 3.

CHAPTER 3

Airfoil Shape Parameterization and Optimization

The design of an active camber morphing wing involves two fundamental challenges: (1) determining the target shape, and (2) achieving that target shape. The target shape of an airfoil is defined by the desired aerodynamic performance at specific flight conditions, such as lift coefficient, drag coefficient, or lift-to-drag ratio, all of which influence the overall performance of an aircraft. To optimize a 2D airfoil for specific flight conditions, the first step is to select and represent a baseline airfoil using a suitable parameterization method based on a set of design parameters. Once the design parameters are determined to fit the baseline airfoil, shape optimization can proceed by adjusting certain parameters to find the optimal shape.

This process involves coupling an optimization algorithm with the airfoil parameterization method to iteratively update the design parameters and achieve the best aerodynamic performance under the given conditions. After the optimized airfoil shapes are obtained, the internal structure can be designed to realize these target shapes in practice. This chapter introduces a modified airfoil parameterization approach based on the Bezier-PARSEC method and describes the use of the Differential Evolution algorithm to update the design variables during the optimization process.

3.1 Differential evolution algorithms and its implementation

As introduced in the literature review chapter, the DE is an effective algorithm for aerodynamic optimization. It is a parallel direct search method that utilizes a number of population NP with D-dimensional parameters [**78**]. It has four main operations: 1) Initialization, 2) Mutation, 3) Crossover 4) Selection. This section will introduce its basic theory and how to implement it in the BP method to design the airfoil shape using MATLAB.

3.1.1 Initilization of population and dimensions

The NP does not change for each generation G in each iteration, and the NP should cover the entire range of parameters. The first population is generated using normally distributed random deviations. The equation for initialization can be expressed as[**77**]:

$$x_{i,0}^{j} = x_{\min}^{j} + \mathrm{rand}(0,1) \cdot \left(x_{\max}^{j} - x_{\min}^{j}\right), \quad j = 1, 2, \ldots, D \tag{3.1}$$

Where i is the population, j is the dimension, $\mathrm{rand}(0,1)$ is the normally distributed random variables in the range [0,1]. This equation ensures the initial population is in the range of the maximum and minimum boundaries while producing normally distributed vectors based on NP and Dimension. Before going to the next operation, the fitness of the first population is tested using the test function (objective function). The initial best-fitted value and its position in the vector are recorded for the Selection operation. For example, the best-fitted value is selected for an LSE objective function as:

$$\mathrm{Min}\, Obj = \sqrt{\left(x_{t_{i,j}} - x_{i,j}\right)^2 + \left(y_{t_{i,j}} - y_{i,j}\right)^2} \tag{3.2}$$

$$[X_{best}, Index(X_{best})] = Min(Obj) \tag{3.3}$$

3.1.2 Mutation

The mutant vectors for the next generation are first created by adding a weighted difference between two random population vectors to a third random vector. There are five frequently used mutation strategies for the Mutation operation [**77**].

1) "DE/rand/1":

$$\mathbf{V}_{i,G} = \mathbf{X}_{r_1^i,G} + F \cdot \left(\mathbf{X}_{r_2^i,G} - \mathbf{X}_{r_3^i,G}\right) \tag{3.4}$$

2) "DE/best/1":

$$\mathbf{V}_{i,G} = \mathbf{X}_{\text{best},G} + F \cdot \left(\mathbf{X}_{r_1^i,G} - \mathbf{X}_{r_2^i,G}\right) \tag{3.5}$$

3) "DE/rand-to-best/1":

$$\mathbf{V}_{i,G} = \mathbf{X}_{i,G} + F \cdot (\mathbf{X}_{\text{best},G} - \mathbf{X}_{i,G}) + F \cdot \left(\mathbf{X}_{r_1^i,G} - \mathbf{X}_{r_2^i,G}\right) \tag{3.6}$$

4) "DE/best/2":

$$\mathbf{V}_{i,G} = \mathbf{X}_{\text{best},G} + F \cdot \left(\mathbf{X}_{r_1^i,G} - \mathbf{X}_{r_2^i,G}\right) + F \cdot \left(\mathbf{X}_{r_3^i,G} - \mathbf{X}_{r_4^i,G}\right) \tag{3.7}$$

5) "DE/rand/2":

$$\mathbf{V}_{i,G} = \mathbf{X}_{r_1^i,G} + F \cdot \left(\mathbf{X}_{r_2^i,G} - \mathbf{X}_{r_3^i,G}\right) + F \cdot \left(\mathbf{X}_{r_4^i,G} - \mathbf{X}_{r_5^i,G}\right). \tag{3.8}$$

The mutant vector $V_{i,G}$ is created for each $X_{i,G}$ in generation G. It can be seen that there are five indices r_1^i - r_5^i, which are integers randomly chosen from [1, NP], which should also be different from the index i. F is a positive scaling factor that controls the difference vector, in the range of [0,2]. $\mathbf{X}_{\text{best},G}$ is the best-fitted value recorded at generation G, which is the same as the X_{best} mentioned previously for the first generation. A possible improvement of the scaling factor F is:

$$F = F_0 * 2^{\exp\left(1 - \frac{T\max}{T\max + 1 - T}\right)} \tag{3.9}$$

However, the scaling factor is usually set as constant between [0,2].

In the mutation operation, it is possible that some values are out of the maximum and minimum boundaries for design variables. An operation that ensures all mutant vectors are in the available range must be taken. A simple method is to make the vectors larger than the

upper boundary equal to the upper boundary and make the vectors smaller than the lower boundary equal to the lower boundary.

3.1.3 Crossover

After the mutation operation, the crossover operation is conducted to increase the population (perturbed parameters) diversity. Equation 3.10 shows the crossover criteria based on the crossover ratio CR.

$$u_{ji,G+1} = \begin{cases} v_{ji,G+1} & \text{if } (\text{randb}(j) \leq CR) \text{ or } j = \text{rnbr}(i) \\ x_{ji,G} & \text{if } (\text{randb}(j) > CR) \text{ and } j \neq \text{rnbr}(i) \end{cases}, \quad j = 1, 2, \ldots, D. \tag{3.10}$$

$randb(j)$ represents the j-th evaluation of a uniform random number generator that produces outcomes in the range $[0, 1]$. CR denotes the crossover constant, also in the range $[0, 1]$, which must be specified by the user.

If the $randb(j)$ value is smaller than the user-determined CR (crossover constant) value, the final vectors in the trial vector $U_{i,G}$ come from the mutation operation $V_{i,G}$. Otherwise, the final vectors come from the initial population $X_{i,G}$.

$rnbr(i)$ is a randomly selected index from the set $\{1, 2, ..., D\}$, ensuring that $u_{i,G+1}$ inherits at least one parameter from $v_{i,G+1}$ [**77**].

The CR value represents the information exchanged among the initial population $X_{i,G}$, the results of mutation operation $V_{i,G}$ and the results of crossover value $U_{i,G}$. The larger the scaling factor F is, the more information is exchanged. Figure 3.1 shows a clear explanation of the information exchange process between initial vectors, mutant vectors and crossover vectors.

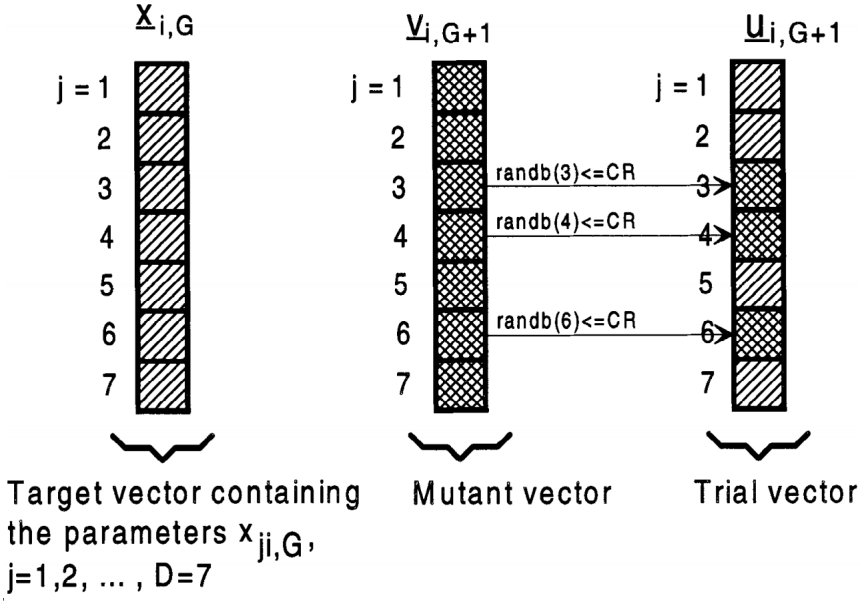

FIGURE 3.1. Explanation of the information exchange process[**78**]

3.1.4 Selection

The final step is to select suitable vectors from crossover trial vectors and keep them for the next generation. Equation 3.11 shows the simple criteria to select the kept values, that compare the fitness of the trial vectors to the initial vectors. According to the principle of survival of the fittest, the design variables will be updated only if the fitness of the trial vectors is better than that of the initial vectors.

$$\mathbf{X}_{i,G+1} = \begin{cases} \mathbf{U}_{i,G}, & \text{if } f\left(\mathbf{U}_{i,G}\right) \leq f\left(\mathbf{X}_{i,G}\right) \\ \mathbf{X}_{i,G}, & \text{otherwise.} \end{cases} \tag{3.11}$$

3.2 Bezier-PARSEC Parameterization Method

The Bezier-PARSEC (BP) method [**73**] employs PARSEC variables as parameters, defining two distinct but continuous Bezier curves to represent the camber and thickness profiles of the airfoil. These two profiles are added and subtracted to obtain the final upper and lower

surfaces of the airfoil. The Bezier curve is controlled by a set of control points in a 2D plane, with three control points positioned in a straight line at the junction between the two curves to ensure gradient continuity. The number of control points depends on the degree of the Bezier curves, which influences both the fitting accuracy and computational cost.

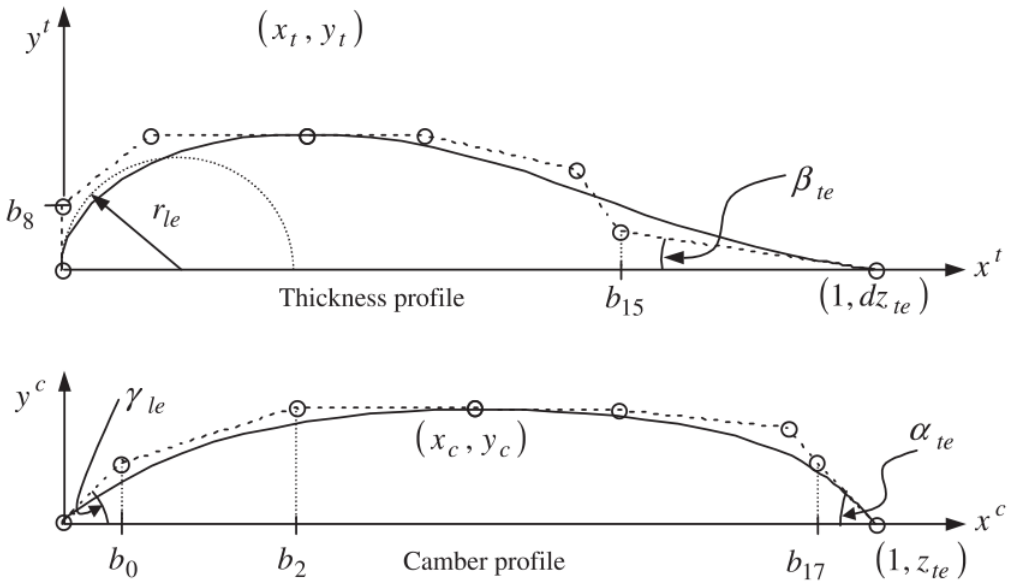

FIGURE 3.2. Definition of the BP-3434 Bezier–PARSEC layout. Two cubic Bezier segments model the leading-edge camber/thickness, while a cubic + quartic pair models the trailing edge[**73**]

Two combinations of Bezier curves were described by Rogalsky: BP3333 and BP3434 [**73**]. A BP3333 combination utilizes two third-degree Bezier curves for both the leading and trailing edge camber and thickness profiles, while the BP3434 combination replaces the third-degree Bezier curve at the trailing edge with a fourth-degree Bezier curve. Figure 3.2 illustrates the definition of the BP3434 combination. The polynomial equations below represent the third-degree and fourth-degree Bezier curves for the x and y coordinates of the camber and thickness profiles [**73**]:

$$x(u) = x_0(1-u)^3 + 3x_1u(1-u)^2 + 3x_2u^2(1-u) + x_3u^3 \tag{3.12}$$

$$y(u) = y_0(1-u)^4 + 4y_1u(1-u)^3 + 6y_2u^2(1-u)^2 + 4y_3u^3(1-u) + y_4u^4 \tag{3.13}$$

The coefficients from x_0 to x_4 and y_0 to y_4 are determined by establishing geometric relationships between the Bezier curves and airfoil parameters. Rogalsky provides detailed derivation steps for these parameters in his thesis [**72**]. The aerodynamic parameters that define the coefficients in the polynomial equations are outlined below, and their variable definitions are provided in Table 3.1 [**73**].

Leading edge thickness curve:

$x_0 = 0 \quad y_0 = 0$
$x_1 = 0 \quad y_1 = b_8$
$x_2 = -3b_8^2/2r_{le} \quad y_2 = y_t$
$x_3 = x_t \quad y_3 = y_t$

Leading edge camber curve:

$x_0 = 0 \quad y_0 = 0$
$x_1 = b_0 \quad y_1 = b_0 \tan(\gamma_{le})$
$x_2 = b_2 \quad y_2 = y_c$
$x_3 = x_c \quad y_3 = y_c$

Trailing edge thickness curve:

$x_0 = x_t \quad y_0 = y_t$
$x_1 = \frac{1}{4}(7x_t + 9b_8^2/2r_{le}) \quad y_1 = y_t$
$x_2 = 3x_t + 15b_8^2/4r_{le} \quad y_2 = \frac{1}{2}(y_t + b_8)$
$x_3 = b_{15} \quad y_3 = dz_{te} +$
$x_4 = 1 \quad (1 - b_{15})\tan(\beta_{te})$
$y_4 = dz_{te}$

Trailing edge camber curve:

$x_0 = x_c \quad y_0 = y_c$
$x_1 = \frac{1}{2}(3x_c - y_c \cot(\gamma_{le})) \quad y_1 = y_c$
$x_2 = \frac{1}{6}(-8y_c \cot(\gamma_{le}) + 13x_c) \quad y_2 = 5y_c/6$
$x_3 = b_{17} \quad y_3 = z_{te} - (1 - b_{17})$
$x_4 = 1 \quad \tan(\alpha_{te})$
$y_4 = z_{te}$

Definition	Variable		
Leading edge camber curve radius	γ_{le}	Leading edge thickness curve radius	$\mathrm{r_{le}}$
Camber curve crest abscissa	$\mathrm{x_c}$	Thickness curve crest abscissa	$\mathrm{x_t}$
Camber curve crest ordinate	$\mathrm{y_c}$	Thickness curve crest ordinate	$\mathrm{y_t}$
Trailing edge thickness curve ordinate	$\mathrm{Z_{te}}$	Trailing edge thickness curve offset	$\mathrm{d_{Zte}}$
Trailing edge camber curve direction	α_{te}	Trailing edge thickness curve wedge angle	β_{te}

TABLE 3.1. Definition of aerodynamic variables in BP method [**79**]

The curve fitting can be conducted by setting suitable boundaries for design parameters [**72**].

Parameter	Lower	Upper	Parameter	Lower	Upper
γ_{le}	0.05	0.1	b_0	0.01	0.1
b_2	0.1	0.3	x_c	0.2	0.5
y_c	0	0.2	b_{17}	0	0.9
z_{te}	0	0.01	α_{te}	0.05	0.1
r_{le}	-0.04	-0.001	b_8	0	0.7
x_t	0.15	0.4	y_t	0.05	0.15
b_{15}	0	0.9	dz_{te}	0	0.001
β_{te}	0.001	0.3			

TABLE 3.2. Initial upper and lower population bounds for Parameters[**72**]

3.3 Objective function of the airfoil shape fitting

The objective function for airfoil fitting is expressed as equation 3.14, which minimizes the shape differences between the baseline and fitted airfoil.

$$\text{Min } f(q) = \sum_{j=1}^{m} \sum_{i=1}^{n} \sqrt{\left(x_{t_{i,j}} - x_{i,j}\right)^2 + \left(y_{t_{i,j}} - y_{i,j}\right)^2} \tag{3.14}$$

Where q is a vector contains the design parameters of the airfoil curve, n is the number of points of the airfoil shape profile, i is the airfoil coordinates number, j is the iteration number, $(x_{t_{i,j}}, y_{t_{i,j}})$ is the target airfoil coordinate and $(x_{i,j}, y_{i,j})$ is the obtained coordinate. This equation will be the fitness function applied in the differential evolution algorithm to update design parameters.

3.3.1 Implementation of DE in Airfoil Fitting

The steps in the shape fitting process are as follows:
(1) Define the baseline airfoil curve coordinates, using the NACA2418 airfoil as the baseline.
(2) Set the PARSEC and Bezier curve parameters within the suggested ranges, as shown in Tables 3.1 and 3.2.
(3) Apply the differential evolution (DE) algorithm (to be discussed later) to update the design parameters and minimize the shape differences between the baseline and the fitted airfoil. This step is divided into three sub-steps: (a) Camber curve fitting, (b) Thickness curve fitting, (c) Combine the two curves (addition and subtraction) to generate the upper and lower surfaces of the airfoil.
(4) Perform post-processing and verify the achieved fitted airfoil.

In the BP parameterization, the design parameters for the camber and thickness profiles are different, which means the camber and thickness profiles will have different x coordinates, posing challenges when adding and subtracting the two curves. One of the approaches is to first perform camber fitting using an equally distributed set of interpolation points, u_{camber}. Then, the set of values for thickness fitting, $u_{thickness}$, can be inversely calculated using the

x_{camber} coordinates and the design parameters for the thickness profile. Equations 3.15 and 3.16 describe the relationship between the two Bezier curves with different coefficients.

$$x(u_{camber}) = x_{0c}(1-u)^3 + 3x_{1c}u(1-u)^2 + 3x_{2c}u^2(1-u) + x_{3c}u^3 \tag{3.15}$$

$$x(u_{thickness}) = x_{0t}(1-u)^3 + 3x_{1t}u(1-u)^2 + 3x_{2t}u^2(1-u) + x_{3t}u^3 \tag{3.16}$$

The above method is computationally expensive, as it requires solving polynomial equations to obtain u for each point in the thickness profile. An alternative, lower-cost method is to generate a large number of x values for the camber profile and find the closest corresponding x value for the thickness profile. Although this method introduces some approximations, it can be minimized by using a large number of interpolation points, such as 1×10^3. Figure 3.3 illustrates the low-cost method for finding the thickness profile x coordinates that correspond to the camber profile x coordinates.

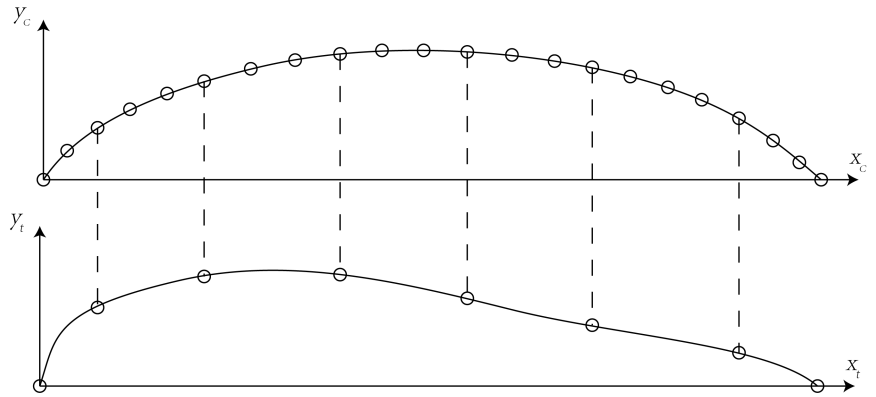

FIGURE 3.3. low-cost method to find corresponding camber and thickness x coordinates

When adding and subtracting the camber and thickness profiles to generate the airfoil curve, another challenge arises: the thickness at each camber point is defined perpendicular to the camber profile, but the slope is unknown. One approximate method involves using two adjacent interpolation points to estimate the slope at a given point, where $k_2 = \frac{y_3 - y_1}{x_3 - x_1}$ (P_1 and P_3 are the two adjacent points and k_2 is the slope of P_2 to estimate). The accuracy of this method improves as the number of interpolation points increases.

Another geometric approach, illustrated in Figure 3.4, offers a solution to this problem. Any continuous set of three points on the camber curve can be assumed to lie on a circle. Two lines are formed by connecting the first and second points, and the second and third points. By finding the midpoints of these two lines, perpendicular lines can be drawn at the midpoints. The intersection of these perpendicular lines provides the centre of the circle. The slope of the thickness profile at the second point is then determined by connecting this point to the centre of the circle. The thickness offsets, d_x and d_y, in the x and y directions can be calculated to accurately represent the asymmetric wing profiles.

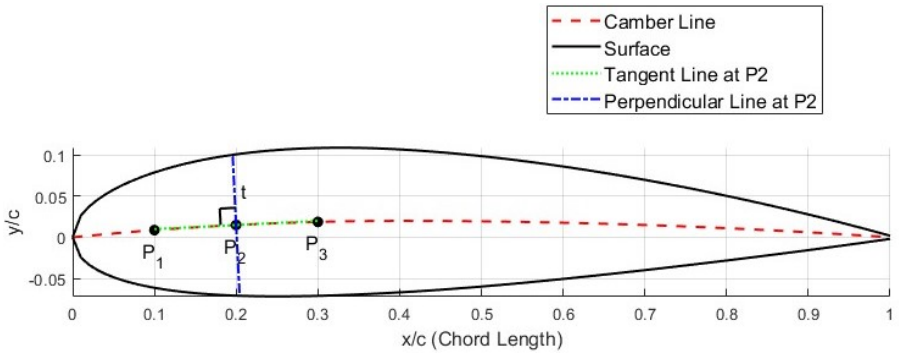

(A) Thickness profile adding and subtracting illustration

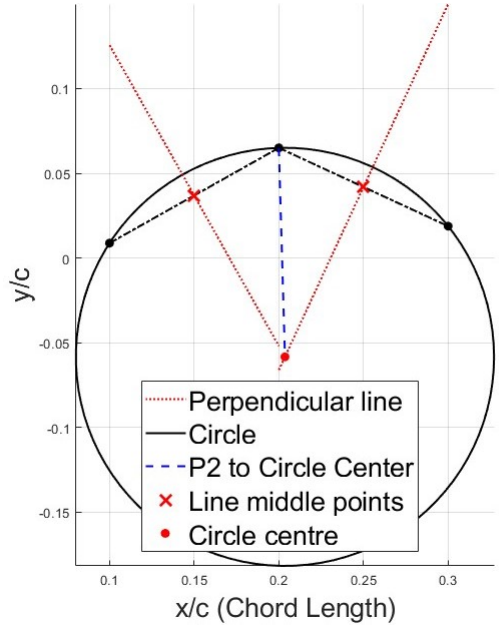

(B) Camber point slope calculation

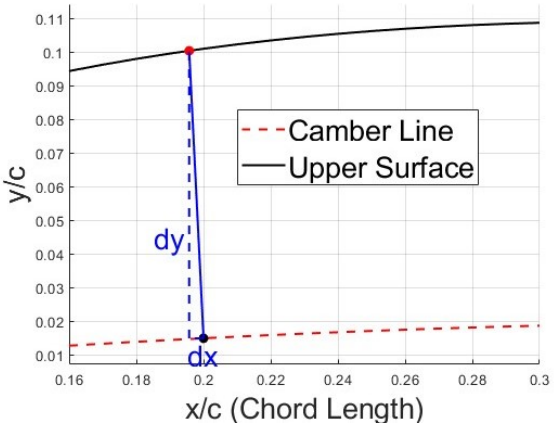

(C) Calculation of the x and y direction offset

FIGURE 3.4. Calculation of the thickness profile slope using circle

The advantage of this method is that it can accurately calculate the slope at any point within a set of three continuous points, even when the interpolation is non-uniform. Since the airfoil curve significantly impacts performance, this method provides greater accuracy compared to simply calculating the midpoint slope using $k_2 = \frac{y_3 - y_1}{x_3 - x_1}$.

Figure 3.5 shows the curve fitting process of a NACA 2418 airfoil. The black solid curve is the trial curve, the red dot points represent the target camber curve, and the green dot points represent the target airfoil surface curve. The trial curve keeps iterating in the range of parameter bounds until it meets the minimum error requirement. There are a total of 16 parameters to be optimized, with the DE parameters set as NP=160 (10 times the number of parameters), F=0.5, CR=0.3. The mutation strategy used is the basic "DE/rand/1". The resultant error for camber fitting is 2e-7 and for airfoil fitting is 5e-4.

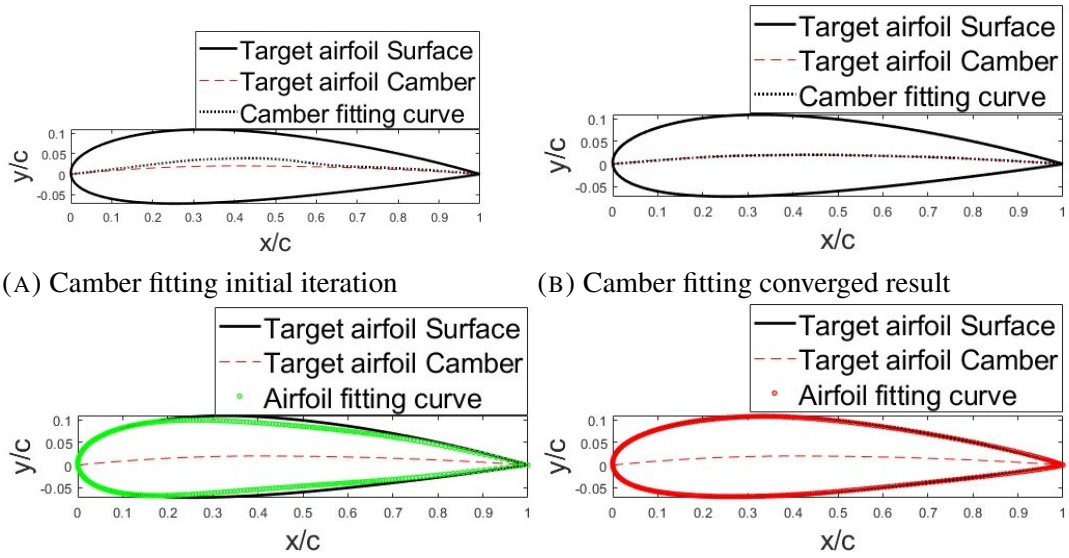

(A) Camber fitting initial iteration

(B) Camber fitting converged result

(C) Airfoil fitting initial iteration

(D) Airfoil fitting converged result

FIGURE 3.5. NACA2418 airfoil curve fitting using DE

To verify the accuracy of representing the airfoil curve using camber and thickness profiles, drawing a circle at a given point with a radius equal to the local thickness can provide direct validation. Figure 3.6 illustrates that the circle at each camber point is tangent to the airfoil curve at the endpoint of each thickness, accounting for the offset. Figure 3.7 provides detailed views of the leading edge and trailing edge of the fitted airfoil. The dashed lines represent

the thickness, which is perpendicular to the camber profile at each point. These figures demonstrate that the accuracy of the BP parameterization is sufficient for producing a well-fitted airfoil, and the method can be verified. The computational cost is acceptable, achieving a shape difference smaller than 5×10^{-4} in approximately 10 minutes. The difference is the sum of the differences between the target and actual nodes. Once the fitting airfoil is obtained, the thickness profile data will be stored and will remain constant in the next airfoil shape optimization stage.

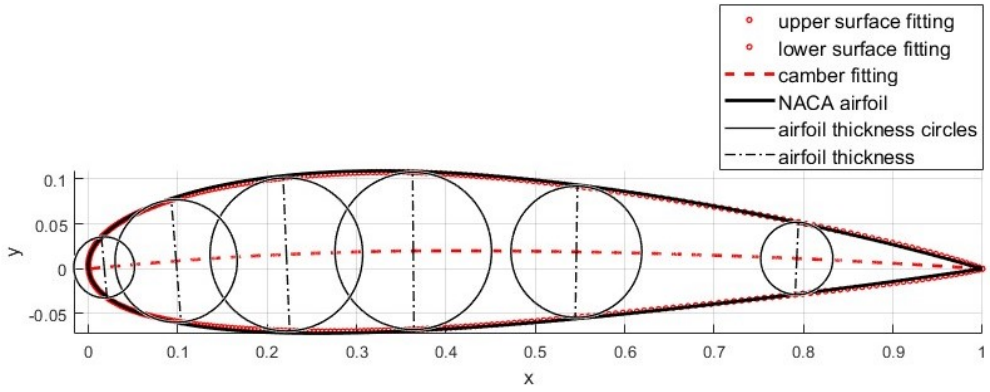

FIGURE 3.6. Thickness-profile verification using the "circle test." At each camber point a circle of radius equal to the local thickness is tangent to the airfoil surface, confirming that the fitted Bézier thickness curve preserves the intended envelope.

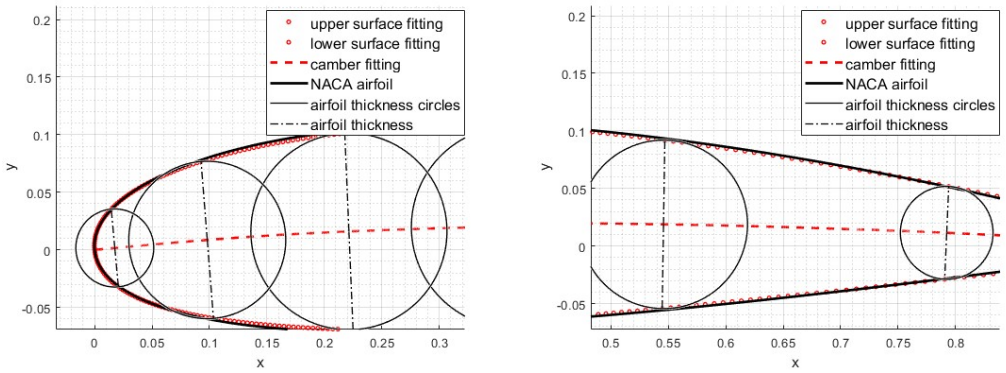

(A) Fitted airfoil leading edge (B) Fitted airfoil trailing edge

FIGURE 3.7. Zoom-in on the fitted NACA 2418 geometry, dashed normals show that camber-line normals intersect the surface precisely, validating orthogonality in the BP fit.

3.4 Modified BP Method for Morphing Wing Design

In the context of the active morphing wing design concept presented in this thesis, the middle section of the wing remains unchanged. Since the BP parameterization utilizes segmented Bezier curves, it allows the original Bezier curves representing the upper and lower surfaces to be divided into three segments. The optimization is applied only to the first curve, representing the leading edge, and the third curve, representing the trailing edge. The newly introduced middle curve, defining the unchanged section, is controlled by two control points. Additionally, the morphing 2D airfoil is designed to maintain a constant thickness along the chord-wise direction, ensuring that the thickness profile remains identical before and after shape optimization.

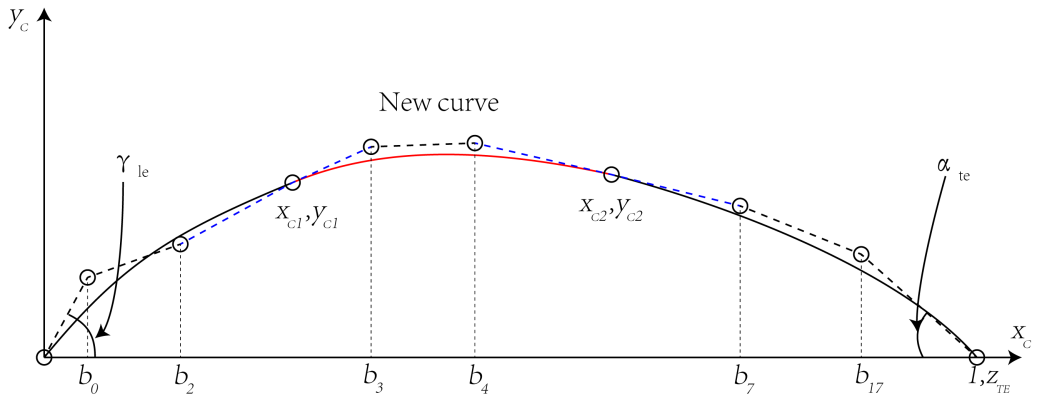

FIGURE 3.8. Modified BP parameterization for the morphing wing. A fixed mid-segment preserves baseline structure, while leading- and trailing-edge Bézier segments are free to morph within a bounded design space.

Figure 3.8 illustrates the modified BP parameterization with new design parameters for the morphing wing's camber profile. The control points correspond to segmentation points such as (x_{c1}, y_{c1}), and the control points on either side are aligned along the same straight line to ensure gradient continuity. This new combination of the camber and thickness profiles is referred to as BP 34-333. In the airfoil shape-fitting process, seven parameters related to the thickness profile will be determined. Meanwhile, nine camber profile parameters remain unchanged, while eight camber profile parameters will be updated to optimize the airfoil

based on the objective function. Table 3.3 presents the new design bounds for the camber profile during airfoil fitting. To preserve the baseline airfoil through the mid-chord region, the two interior Bezier control points obtained from the baseline-airfoil curve fit are *fixed* at those fitted values. Design freedom is granted exclusively to the interior, leading-edge and trailing-edge tip control points, which are allowed to translate within pre-defined bounds. These limits were selected from a preliminary testing that balanced deformation and structural feasibility. A larger bound can make it achieve a better performance airfoil shape but will result in extra challenges in shape matching.

Parameter	Lower	Upper	Parameter	Lower	Upper
γ_{le}	fixed	fixed	b_0	0.01	0.2
b_2	0.2	0.28	x_{c1}	0.3	0.3
y_{c1}	fixed	fixed	b_{17}	0.8	0.9
z_{te}	-0.05	0	α_{te}	0.02	0.1
b_3	fixed	fixed	b_4	fixed	fixed
b_{3y}	fixed	fixed	b_{4y}	fixed	fixed
x_{c2}	0.7	0.7	y_{c2}	fixed	fixed
b_7	0.7	0.95	x_0	0	0.1
y_0	-0.1	0	x_{end}	0.97	1

TABLE 3.3. Upper and lower bounds for design parameters in updated camber profile

Parameter	Lower	Upper	Parameter	Lower	Upper
r_{le}	-0.04	-0.001	b_8	0	0.7
x_t	0.15	0.4	y_t	0.05	0.15
b_{15}	0	0.9	dz_{te}	0	0.001
β_{te}	0.001	0.3			

TABLE 3.4. Upper and lower bounds for design parameters in thickness profile[**72**]

3.5 Objective function of the airfoil shape optimization

After obtaining the fitted airfoil using the updated camber parameters and the original thickness parameters, the camber profile will be further adjusted to generate trial shapes for aerodynamic analysis during shape optimization. Parameters such as the camber starting point and endpoint,

listed in Table 3.3, were treated as non-design parameters during the fitting process but will now become flexible variables, allowing deformation of the leading and trailing edges. Table 3.5 presents the bounds for the camber design parameters used in shape optimization, while the parameters listed in Table 3.3 but not included in Table 3.5 will remain constants.

Parameter	Lower	Upper	Parameter	Lower	Upper
b_0	0.01	0.2	b_2	0.1	0.299
b_{17}	0.72	0.9	z_{te}	-0.1	0
α_{te}	0.02	0.1	b_7	0.7	0.95
x_0	0	0.05	y_0	-0.1	0

TABLE 3.5. Upper and lower bounds for camber design parameters in shape optimization

Note that the BP parameterization does not account for the physical behavior of the airfoil skin material, such as compression or stretch, which means the resultant shape may not be physically realistic. Additionally, the original BP parameterization fixes the camber curve coordinates at the leading and trailing edge tips. This results in the optimized airfoil having a different total curve length compared to the baseline airfoil, posing challenges for structural optimization. To ensure consistency in the total airfoil curve length, this constraint will be incorporated into the objective function with a weighting factor.

The objective function for shape optimization can include goals such as minimizing $C_D(q)$, maximizing $C_L(q)$, maximizing $C_L(q)/C_D(q)$, or maximizing $C_L(q)^{\frac{3}{2}}/C_D(q)$, where C_D is the drag coefficient and C_L is the lift coefficient. If the optimized airfoil is required to maintain the same arc length as the original airfoil, a balance can be made between aerodynamic performance and total curve length. Equation 3.17 shows the objective function for maximizing endurance while minimizing the difference in curve length, using a weighting factor w_s.

$$\text{Max } f(q) = \frac{C_L^{\frac{3}{2}}}{C_D} * (1 - w_s) - w_s * |S_i - S| \tag{3.17}$$

Where S_i is the total arc length of the optimized airfoil, and S is the total arc length of the original airfoil. The endurance parameter $\frac{C_L^{\frac{3}{2}}}{C_D}$ is derived using the Breguet endurance equation

for propeller-driven aircraft, as shown below [**86**]:

$$E = \int_{W_0 - W_f}^{W_0} \frac{\eta_p}{c} \left(\frac{C_L^{3/2}}{C_D} \right) \sqrt{\frac{\rho_\infty S}{2}} \frac{dW}{W^{3/2}} \tag{3.18}$$

In the endurance equation, E represents the total flight time the aircraft can sustain, η_p is the propeller efficiency accounting for the effectiveness of the propulsion system, c is the specific fuel consumption representing the rate of fuel burned per unit thrust per unit time, C_L and C_D are the coefficients of lift and drag, respectively, ρ_∞ is the freestream air density, S is the wing reference area, W is the aircraft weight that decreases as fuel is consumed, W_0 is the initial weight of the aircraft including the total fuel weight, and W_f is the fuel weight consumed during flight.

If the target airfoil needs to meet specific arc length changes on either the upper or lower surface, the penalized objective function can be further modified as:

$$\text{Max } f(q) = \frac{C_L^{\frac{3}{2}}}{C_D} * (1 - w_{leading} - w_{low}) - w_{low} * |S_{low_i} - S_{low}| - w_{leading} * |S_{leading_i} - S_{leading}| \tag{3.19}$$

$$\text{Max } f(q) = C_L * (1 - w_{leading} - w_{low}) - w_{low} * |S_{low_i} - S_{low}| - w_{leading} * |S_{leading_i} - S_{leading}| \tag{3.20}$$

Where $w_{leading}$ and w_{low} are the weighting factors for the leading edge (LE) total curve length and the lower surface curve length of the trailing edge (TE), respectively. $S_{leading}$ and S_{low} are the target total curve lengths of the LE and TE lower surface, while $S_{leading_i}$ and S_{low_i} are the actual total curve lengths of the LE and TE lower surface.

The weighting factors were adjusted via a manual process: beginning with a near-zero value, the factor was incrementally increased until the structural shape-matching error dropped below the prescribed tolerance.

3.5.1 Shape optimization results for different objective functions

As shown in Table 3.5, there are eight parameters to be determined for the camber profile in the shape optimization process using the modified BP method. In this optimization problem,

the leading and trailing edge points are allowed to morph within predetermined ranges: [0, 0.05] in the x-direction and [-0.1, 0.05] in the y-direction. The flight condition is set at a 5-degree angle of attack in viscous flow, with a Reynolds number of 6×10^6 and Mach number 0, using XFOIL for fast and stable convergence. By applying the defined multi-objective functions, the optimized airfoil shape can be obtained. The morphable sections of the NACA 2418 airfoil are located between 0%-30% and 70%-100% chord, as illustrated in Figure 3.9.

Figure 3.10 shows the trial shapes during the optimization. The total arc length of the trail shapes is optimized to approach the expected value, while the performance is optimized. The sum of the aerodynamic coefficients and shape difference of the trail shapes is recorded and used as the objective function for the next generation.

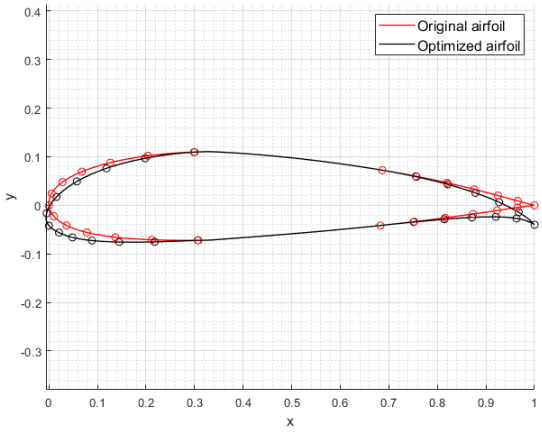

FIGURE 3.9. Morphable regions of the baseline NACA 2418

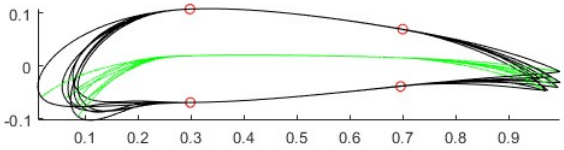

FIGURE 3.10. Examples of attempted shapes during optimization

Figure 3.11 presents several optimized shape results for different objective functions, considering both aerodynamic coefficients and curve length differences. The performance improvements are summarized in Table 3.6. It can be observed that there are some jumps in aerodynamic parameters in early iterations. In those cases, the aerodynamic parameters are satisfied but then dropped because of a second constraint on the arc length control.

The parameter productivity efficiency, $C_L^{1.5}/C_D$, represents the aircraft's cruising capability, indicating its ability to move a gross weight over the maximum possible distance. This parameter is particularly valuable for analysis when designing a morphing wing.

Since the airfoil must be designed to provide sufficient stiffness to withstand aerodynamic loads, selecting appropriate materials becomes a challenging task. To simplify the structural design, a solid isotropic material is used, with the assumption that the trailing edge features an open upper surface at 70% of the chordwise location. As a result, the arc length of the target shape will exceed that of the original airfoil.

Typically, the initially obtained shape is not optimal because the target curve length is unknown prior to structural optimization. Multiple design iterations are often necessary to determine the best target shape, which can be efficiently refined in subsequent analyses.

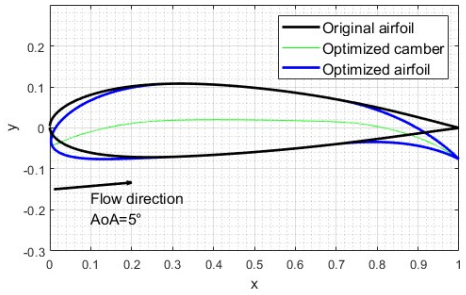

(A) Optimized shape for Max CL

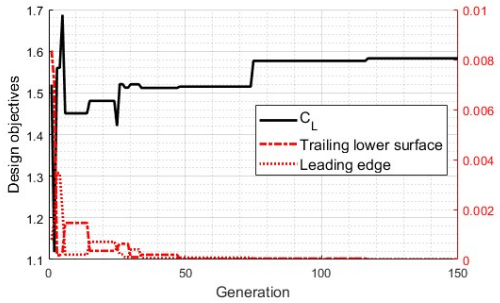

(B) Objective function for Max CL

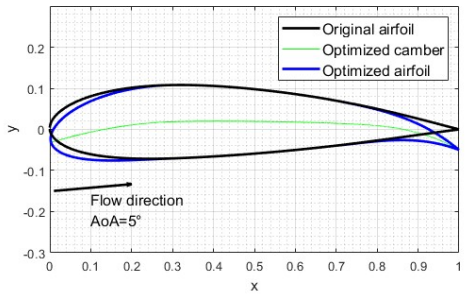

(C) Optimized shape for Max $CL^{1.5}/CD$

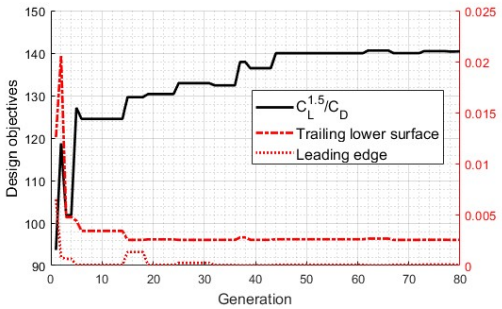

(D) Objective function Max $CL^{1.5}/CD$

FIGURE 3.11. Airfoil shape optimization results for different objectives

	CL	CL^1.5/CD
Baseline airfoil	0.807	98.84
Optimized airfoil	1.583	140.36
Percentage of improvements	+96.16% %	+42.01%

TABLE 3.6. Results in performance improvements

3.6 Summary

In this chapter, the focus is on the shape parameterization and optimization of a morphing wing, utilizing a modified Bezier-PARSEC (BP) method and differential evolution (DE) algorithm. The chapter begins by introducing the typical differential evolution algorithm and its formulations. Then the BP parameterization is introduced, which divides the camber and thickness profiles of the airfoil into segments for easier manipulation. A modified Bezier-PARSEC (BP) method is employed, keeping the middle section of the wing fixed while allowing the leading and trailing edges to morph. This design flexibility is crucial for enhancing the aerodynamic performance of the morphing wing.

This chapter introduces a refined objective function that integrates both airfoil performance and shape requirements, balanced through a weighting factor. This approach ensures a more achievable shape in structural design, reducing the discrepancy between the target shape and the deformed shape. The achievable shape means a shape that can be realized using existing material and actuation. In the meantime, the achieved displacement error is within tolerance. The optimization process focuses on adjusting design parameters for the camber profile to enhance aerodynamic performance, aiming to maximize the lift coefficient (C_L), minimize the drag coefficient (C_D), optimize the lift-to-drag ratio (C_L/C_D) or maximum the endurance ($C_L^{1.5}/C_D$).

Additionally, specific ranges were set for morphing regions, such as $0\% - 30\%$ and $70\% - 100\%$ chord, and the morphing behaviour was analyzed under specific flight conditions, including a 5-degree angle of attack and Reynolds number of 6×10^6. Optimized airfoil shapes were obtained, showing improvements in aerodynamic performance and confirming

the effectiveness of the multi-objective optimization approach in designing morphing wings. The obtained shape will be set as the target in the next chapter to do topology optimization.

CHAPTER 4

The Structural Optimization of Active Morphing Wing

This chapter presents the problem statement and formulation for the topology optimization of shape control using the SIMP method. The formulation focuses on minimizing the displacement error between the initial observation points and the target points. In contrast to the fixed observation and target points commonly used in the literature, a more adaptive approach is proposed, utilizing dynamic target points on the target airfoil profile to mitigate uncertainties in their location. The objective function also incorporates a minimum compliance problem, weighted to ensure the optimized structure retains sufficient stiffness to withstand aerodynamic loads. Furthermore, including the minimum compliance criterion enhances the stability of the optimization process, leading to faster convergence. Additionally, a benchmark comparison between the developed code/results and published code/results is provided to validate the accuracy of the developed algorithm. Finally, the designed morphing wing will be tested and compared with the baseline airfoil.

4.1 Problem Statement and Formulation for Shape Control Mechanism

The morphing wing's leading and trailing edges are designed separately, employing two distinct design domains that cover the front 30% and rear 30% of the airfoil, respectively. The design objectives are as follows: a. Actuate the compliant mechanism to the desired position. b. Minimize structural compliance to ensure sufficient stiffness for withstanding the loads from both the actuator and aerodynamic forces.

4.1.1 Problem Definition and Objective Function

The problem can be defined as:
For a fixed actuation load location, apply a constant input force to determine the optimal material distribution that minimizes the geometrical deviation between the actuated external profile and the desired external profile. At the same time, minimize the compliance using a weighting factor. Convergence is achieved when the volume fraction constraint, the change in the design variables and number of high-density elements meet the specified criteria. The optimization problem is based on the following assumptions:
1. The airfoil is represented as a 2D profile with a specified angle of attack.
2. The airflow is uniform and occurs at a constant velocity.
3. A predefined actuation system is integrated within the airfoil.
4. Aerodynamic pressure is assumed constant for small deformations.
5. The airfoil is assumed to deform into the target shape, with the corresponding pressure distribution used as the external load in the topology optimization.

The five assumptions bound the aero-structural task to a single static solve: a 2-D airfoil in steady, uniform flow, a prescribed actuation system, and a frozen pressure field reduce the coupled FSI problem to tractable topology optimization. Assumptions 1–2 drop 3-D

and unsteady effects; 3 locks actuator details; 4 keeps the pressure constant; 5 makes aeroelasticity one-way. Such simplifications are sensible for a first pass with modest deformations, but pressure updates, spanwise flow and real actuator limits must be re-introduced in later, higher-fidelity studies.

The objective function, aimed at minimizing the geometrical discrepancy, is expressed as:

$$\min f(\rho) = |G_t - G| \tag{4.1}$$

Where G_t represents the target airfoil profile, and G denotes the deformed airfoil profile at each iteration. Given that the airfoil geometry is described by 2D coordinates, the objective function is expanded as the least square error between the target and deformed profiles:

$$\min f(\rho) = \sum_{i=1}^{n} \left((x_{t,i} - x_i)^2 + (y_{t,i} - y_i)^2 \right) \tag{4.2}$$

Where i represents the i_{th} observation point, n is the total number of observation points, and $(x_{t,i}, y_{t,i})$ and (x_i, y_i) are the coordinates of the target and deformed observation points, respectively. The square root is omitted, as it does not influence the optimization direction, provided that the enclosed values are positive.

4.1.2 Method for Determining Target Point Locations

In Chapter 3, the target airfoil profiles with optimized performance were defined. However, to convert these shape differences into precise displacement differences, a real-time displacement error update method is required. Since the optimization process applies virtual loads to observation points to compute virtual displacements (virtual load and displacement introduction can be found in [**64**], [**68**]-[**70**]), the method must correlate each observation point with other points to determine the displacement error. Two intuitive, geometry-based methods were developed in this chapter to calculate displacement errors between observation points and their dynamic targets, each offering distinct advantages and limitations.

To demonstrate these methods, Figures 4.1, 4.2, and 4.3 provide examples of one-dimensional curve deformation. In this case, three points on the original black curve are considered. The

left end is fixed on the wall. The curve is actuated to the green dashed curve and is expected to deform into the target blue curve. By selecting the second point as the observation point, its deformed coordinates can be calculated using finite element analysis (FEA).

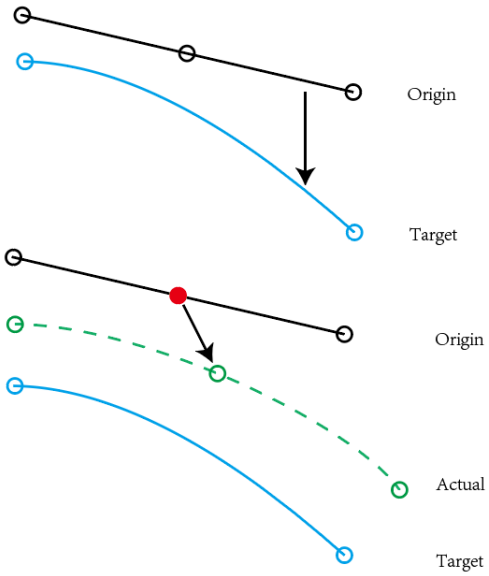

FIGURE 4.1. 1-D curve deformation error example

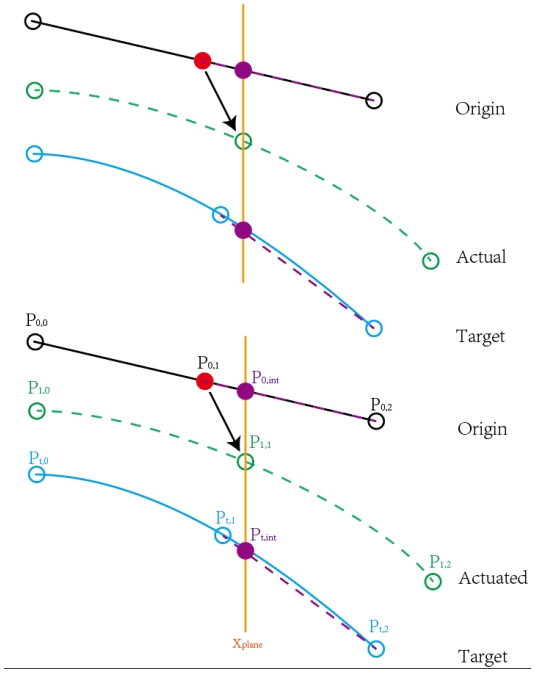

FIGURE 4.2. The method of dynamic vertical plane

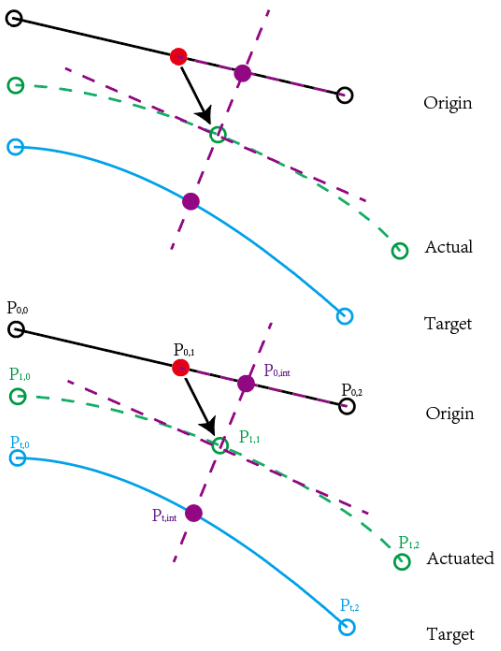

FIGURE 4.3. The method of dynamic perpendicular line

In the first method, to determine the actual and target displacements, a dynamic vertical plane (yellow vertical line in Figure 4.2) is employed that shifts with the deformed observation point $(P_{1,1})$. The intersection of this plane with the original curve gives the original point $P_{0,\text{int}}$, while its intersection with the target curve provides the target point $P_{t,\text{int}}$, as shown in Figure 4.2. Linear interpolation is applied to calculate the coordinates of both the original and target points, based on the known positions of neighboring nodes along the original and target curves.

The second method uses the tangent line at the observation point $(P_{1,1})$, where its slope is denoted as k_1. The perpendicular line to this tangent is then calculated as $k_2 = -\frac{1}{k_1}$. The intersection of this perpendicular line with the original curve yields the original point $P_{0,\text{int}}$, while its intersection with the target curve gives the target point $P_{t,\text{int}}$, as shown in Figure 4.3. The actual and target displacements in the x-direction for the i_{th} observation point are defined as $u_{x,i} = P_{x,1,1} - P_{x,0,\text{int}}$ and $u_{x,t,i} = P_{x,t,\text{int}} - P_{x,0,\text{int}}$, respectively. The displacement error in the x-direction is then calculated as:

$$\textbf{error}_x = u_{x,t,i} - u_{x,i} \tag{4.3}$$

These two methods effectively measure the relative error between the curves and are particularly useful when the curves do not exhibit significant elongation or deformation. The dynamic plane method has a lower computational cost because it requires only virtual load cases in the y-direction, avoiding the most time-consuming part of the finite element analysis. However, if the geometry undergoes large deformations in both x and y directions, this method may fail in elongated sections. The second method accounts for both directions, but in problems where the y-direction deformation dominates, convergence may be slower, requiring a trade-off between x and y direction sensitivities. Otherwise, the x-direction may produce unexpectedly large sensitivities, slowing convergence.

Figure 4.4 illustrates the implementation of both methods in the trailing edge design.

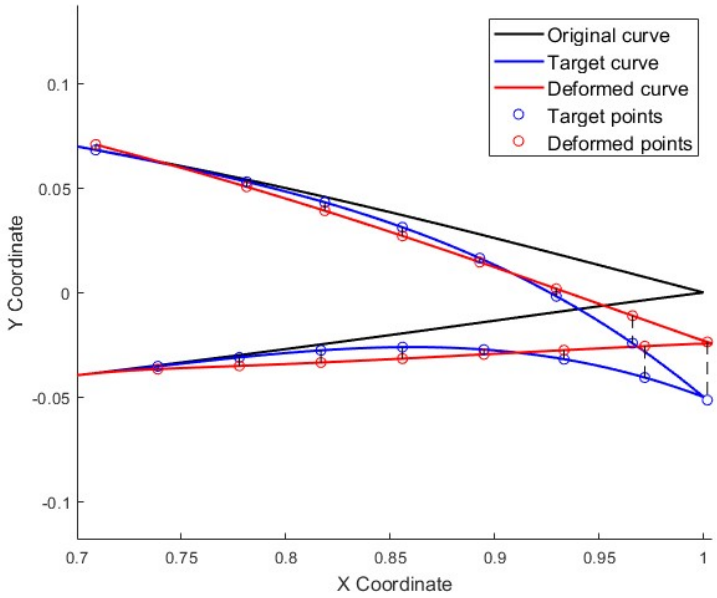

(A) Implementation of dynamic vertical plane method on trailing edge

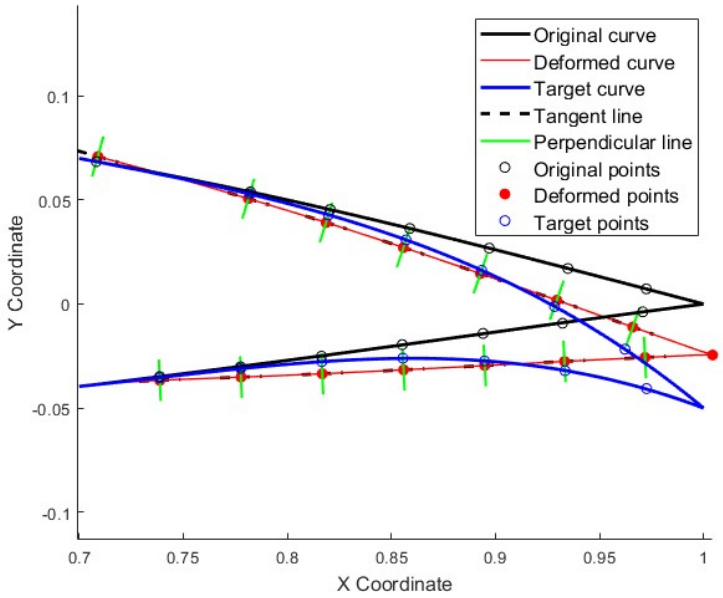

(B) Implementation of dynamic perpendicular line method on trailing edge

FIGURE 4.4. Implementation of dynamic vertical plane method and dynamic perpendicular line method

4.1.3 Problem definition and formulation

The optimization problem and constraints are defined as:

$$
\begin{aligned}
&\text{Find:} \quad \rho_e = [\rho_1, \rho_2, \ldots, \rho_N]^T \\
&\text{Min:} f(\rho) = \sum_{i=1}^{n} \left((u_{x,t,i} - u_{x,i})^2 + (u_{y,t,i} - u_{y,i})^2 \right) \cdot (1 - w_c) \cdot c_1 + \mathbf{F}^T \mathbf{U} \cdot w_c \cdot c_2 \\
&\text{s.t.} \quad \begin{cases} \mathbf{KU} = \mathbf{F} \\ \mathbf{KV} = \mathbf{L} \\ \sum_{i=1}^{N} \rho_e v_e \leq V_{target} \\ 0 < \rho_{\text{min}} \leq \rho_e \leq 1 \end{cases}
\end{aligned}
$$

The objective function considers two problems and can be defined as:

$$\text{Min } f(\rho) = s(\rho) \cdot (1 - w_c) \cdot c_1 + c(\rho) \cdot w_c \cdot c_2 \tag{4.4}$$

Where the shape control problem is $s(\rho)$ and the minimum compliance problem is $c(\rho)$ in the FEM form. n is the total number of observation points, $u_{x,t,i}$ and $u_{y,t,i}$ are the target displacements in the x and y directions, while $u_{x,i}$ and $u_{y,i}$ represent the actual displacements in the respective directions. The design variable vector, ρ_e, corresponds to the density of each element, and w_c is the weighting factor for the minimum compliance problem. The load vector is denoted by $\mathbf{F}$, and the displacement vector by $\mathbf{U}$. Additionally, c_1 and c_2 are scaling factors for the sensitivity of the shape control problem and the minimum compliance problem, respectively. The scaling factors $c_1$and c_2 normalise the sensitivity magnitudes of the shape-control and minimum-compliance terms, respectively, so that both contributions operate on comparable scales. This makes it easier to tune the weighting factor w_c, which is ultimately chosen to satisfy the prescribed shape-matching error tolerance.

4.1.4 Material interpolation for $E_e(\rho_e)$

In the SIMP method, the material interpolation is given by:

$$E_e(\rho_e) = E_{min} + \rho_e^p(E_0 - E_{min}) \tag{4.5}$$

The partial derivative with respect to ρ_e is:

$$\frac{\partial E_e(\rho_e)}{\partial \rho_e} = p\rho_e^{p-1}(E_0 - E_{min}) \tag{4.6}$$

where E_0 represents the modulus of elasticity of the solid isotropic material, E_{min} is the minimum modulus of elasticity, and p denotes the penalty factor.

4.1.5 Sensitivity Analysis

To find the derivative of $f(\rho)$ with respect to ρ_i, start with the displacement terms $s(\rho)$, it can be expanded as:

$$s(\rho) = \sum_{i=1}^{n} \left((u_{x,t,i})^2 - 2u_{x,t,i}u_{x,i} + (u_{x,i})^2 + (u_{y,t,i})^2 - 2u_{y,t,i}u_{y,i} + (u_{y,i})^2\right) \tag{4.7}$$

Eliminate the constant terms and its derivative is:

$$\frac{\partial s(\rho)}{\partial \rho_e} = \sum_{i=1}^{n} \left(\frac{\partial(-2u_{x,t,i}u_{x,i})}{\partial \rho_e} + \frac{\partial(u_{x,i})^2}{\partial \rho_e} - \frac{\partial(-2u_{y,t,i}u_{y,i})}{\partial \rho_e} + \frac{\partial(u_{y,i})^2}{\partial \rho_e}\right) \tag{4.8}$$

Using the chain rule and rearrange:

$$\frac{\partial s(\rho)}{\partial \rho_e} = \frac{\partial s(\rho)}{\partial u_i}\frac{u_i}{\partial \rho_e} \tag{4.9}$$

$$\frac{\partial s(\rho)}{\partial \rho_e} = \sum_{i=1}^{n} \left(2(u_{x,i} - u_{x,t,i}) \cdot \frac{\partial u_{x,i}}{\partial \rho_e} + 2(u_{y,i} - u_{y,t,i}) \cdot \frac{\partial u_{y,i}}{\partial \rho_e}\right) \tag{4.10}$$

The displacement of a specified degree of freedom can be expressed as:

$$u_j = \mathbf{L}^T\mathbf{U} = \mathbf{V}^T\mathbf{K}\mathbf{U} \tag{4.11}$$

where u_j denotes the displacement of a specified degree of freedom, $\mathbf{L}$ and $\mathbf{V}$ represent the adjoint load vector and adjoint displacement vector, respectively, $\mathbf{K}$ is the global stiffness matrix, and $\mathbf{U}$ is the global displacement vector.

Differentiate u_j with respect to the design variable ρ_e:

$$\frac{\partial u_j}{\partial \rho_e} = \frac{\partial}{\partial \rho_e}\left(\mathbf{V}^T\mathbf{K}\mathbf{U}\right) \tag{4.12}$$

$$\frac{\partial u_j}{\partial \rho_e} = \left(\frac{\partial \mathbf{V}^T}{\partial \rho_e}\mathbf{K}\mathbf{U}\right) + \left(\mathbf{V}^T\frac{\partial(\mathbf{K}\mathbf{U})}{\partial \rho_e}\right) \tag{4.13}$$

Since $F = KU$ and F is independent of the design variable, the equation can be simplified to:

$$\frac{\partial u_j}{\partial \rho_e} = \frac{\partial \mathbf{V}^T}{\partial \rho_e}\mathbf{K}\mathbf{U} \tag{4.14}$$

Since $L = KV$ and L is independent of the design variable:

$$\frac{\partial \mathbf{L}}{\partial \rho_e} = \frac{\partial}{\partial \rho_e}(\mathbf{K}\mathbf{V}) \tag{4.15}$$

$$0 = \frac{\partial \mathbf{K}}{\partial \rho_e}\mathbf{V} + \mathbf{K}\frac{\partial \mathbf{V}}{\partial \rho_e} \tag{4.16}$$

Rearranging the equation:

$$\mathbf{K}\frac{\partial \mathbf{V}}{\partial \rho_e} = -\frac{\partial \mathbf{K}}{\partial \rho_e}\mathbf{V} \tag{4.17}$$

This yields:

$$\frac{\partial \mathbf{V}^T}{\partial \rho_e}\mathbf{K} = -\mathbf{V}^T\frac{\partial \mathbf{K}}{\partial \rho_e} \tag{4.18}$$

Substitute equation (18) into equation (13):

$$\frac{\partial u_j}{\partial \rho_e} = -\mathbf{V}^T\frac{\partial \mathbf{K}}{\partial \rho_e}\mathbf{U} \tag{4.19}$$

Since the stiffness matrix k is linear in ρ_e, the global stiffness matrix $\mathbf{K}$ is a sum of element stiffness matrices:

$$\mathbf{K} = \sum_{e=1}^{N} \mathbf{k}_e(E_e) \tag{4.20}$$

Thus, the partial derivative $\frac{\partial \mathbf{K}}{\partial \rho_e}$ is:

$$\frac{\partial \mathbf{K}}{\partial \rho_e} = \frac{\partial \mathbf{k}_e}{\partial \rho_e} = -p\rho_e^{p-1}(E_0 - E_{min})\mathbf{k}_0 \tag{4.21}$$

Here, $\mathbf{U}$ and $\mathbf{V}$ are the global and adjoint displacement vectors, $\mathbf{u}_e$ and $\mathbf{v}_e$ can be denoted as the displacement vectors corresponding to the e-th element due to the load vectors. Thus:

$$\frac{\partial u_j}{\partial \rho_e} = -\mathbf{v}_e^T \frac{\partial \mathbf{k}_e}{\partial \rho_e}\mathbf{u}_e = -\mathbf{v}_e^T \frac{\partial E_{\rho_e}\mathbf{k}_0}{\partial \rho_e}\mathbf{u}_e = -p\rho_e^{p-1}(E_0 - E_{min})\mathbf{v}_e^T\mathbf{k_0}\mathbf{u}_e \tag{4.22}$$

Substitute equation (4.24) to equation (4.11), the sensitivity of objective function in terms of the displacement error is:

$$\begin{aligned}\frac{\partial s(\rho)}{\partial \rho_i} =& -2p(E_0 - E_{min}) \cdot \sum_{i=1}^{n} \big((u_{x,i} - u_{x,t,i}) \cdot p\rho_e^{p-1}\mathbf{v}_{e,x}^T\mathbf{k_0}\mathbf{u}_{e,x} \\ &+(u_{y,i} - u_{y,t,i}) \cdot p\rho_e^{p-1}\mathbf{v}_{e,y}^T\mathbf{k_0}\mathbf{u}_{e,y}\big)\end{aligned} \tag{4.23}$$

The objective function for minimum compliance is given by:

$$\min c(\rho) = \mathbf{F}^T\mathbf{U} \tag{4.24}$$

Using the adjoint method, introducing an arbitrary but fixed vector $\tilde{\mathbf{U}}$ and rewriting the equation as:

$$c(\rho) = \mathbf{F}^T\mathbf{U} - \tilde{\mathbf{U}}^T(\mathbf{K}\mathbf{U} - \mathbf{F}) \tag{4.25}$$

To find the sensitivity of the compliance with respect to the design variable ρ_e, differentiate $c(\rho)$ with respect to ρ_e:

$$\frac{\partial c(\rho)}{\partial \rho_e} = \frac{\partial}{\partial \rho_e}\left(\mathbf{F}^T\mathbf{U} - \tilde{\mathbf{U}}^T(\mathbf{K}\mathbf{U} - \mathbf{F})\right) \tag{4.26}$$

Applying the chain rule:

$$\frac{\partial c(\rho)}{\partial \rho_e} = \mathbf{F}^T\frac{\partial \mathbf{U}}{\partial \rho_e} - \tilde{\mathbf{U}}^T\frac{\partial}{\partial \rho_e}(\mathbf{K}\mathbf{U} - \mathbf{F}) \tag{4.27}$$

Since $\mathbf{F}$ does not depend on ρ_e, focus on the differentiation of $\mathbf{KU}$:

$$\frac{\partial}{\partial \rho_e}(\mathbf{K}\mathbf{U} - \mathbf{F}) = \frac{\partial \mathbf{K}}{\partial \rho_e}\mathbf{U} + \mathbf{K}\frac{\partial \mathbf{U}}{\partial \rho_e} \tag{4.28}$$

Substituting this back into the expression and get:

$$\frac{\partial c(\rho)}{\partial \rho_e} = \mathbf{F}^T \frac{\partial \mathbf{U}}{\partial \rho_e} - \tilde{\mathbf{U}}^T \left(\frac{\partial \mathbf{K}}{\partial \rho_e} \mathbf{U} + \mathbf{K} \frac{\partial \mathbf{U}}{\partial \rho_e} \right) \tag{4.29}$$

Grouping the terms involving $\frac{\partial \mathbf{U}}{\partial \rho_e}$:

$$\frac{\partial c(\rho)}{\partial \rho_e} = \left(\mathbf{F}^T - \tilde{\mathbf{U}}^T \mathbf{K} \right) \frac{\partial \mathbf{U}}{\partial \rho_e} - \tilde{\mathbf{U}}^T \frac{\partial \mathbf{K}}{\partial \rho_e} \mathbf{U} \tag{4.30}$$

Now introduce the adjoint equation $\tilde{\mathbf{U}}^T \mathbf{K} = \mathbf{F}^T$. This simplifies the expression as follows:

$$\mathbf{F}^T - \tilde{\mathbf{U}}^T \mathbf{K} = 0 \tag{4.31}$$

Thus:

$$\frac{\partial c(\rho)}{\partial \rho_e} = -\tilde{\mathbf{U}}^T \frac{\partial \mathbf{K}}{\partial \rho_e} \mathbf{U} \tag{4.32}$$

Assuming $\tilde{\mathbf{U}} = \mathbf{U}$ in the problem:

$$\frac{\partial c(\rho)}{\partial \rho_e} = -\mathbf{U}^T \frac{\partial \mathbf{K}}{\partial \rho_e} \mathbf{U} \tag{4.33}$$

In terms of the material interpolation model in equation (4.6):

$$\frac{\partial \mathbf{K}}{\partial \rho_e} = p \rho_e^{p-1} (E_0 - E_{min}) \mathbf{K}_0 \tag{4.34}$$

The final sensitivity of the minimum compliance objective function is:

$$\frac{\partial c(\rho)}{\partial \rho_e} = -p \rho_e^{p-1} (E_0 - E_{min}) \mathbf{U}^T \mathbf{K}_0 \mathbf{U} \tag{4.35}$$

As mentioned, the stiffness matrix k, displacement vector $\mathbf{U}$ and $\mathbf{V}$ are linear in ρ_e, the equation can be written in element level [**81**]:

$$\frac{\partial c(\rho)}{\partial \rho_e} = -p \rho_e^{p-1} (E_0 - E_{min}) \mathbf{u_e}^T \mathbf{k}_0 \mathbf{u_e} \tag{4.36}$$

The combined sensitivity of objective function is:

$$\begin{aligned}\frac{\partial f}{\partial \rho_e} = &\sum_{i=1}^{n}(-2p(E_0 - E_{min}) \cdot \big((u_{x,i} - u_{x,t,i}) \cdot p\rho_e^{p-1}\mathbf{v}_{e,x}^T\mathbf{k_0}\mathbf{u}_{e,x} \\ &+(u_{y,i} - u_{y,t,i}) \cdot p\rho_e^{p-1}\mathbf{v}_{e,y}^T\mathbf{k_0}\mathbf{u}_{e,y}\big) \cdot (1 - w_c)) \cdot c_1 \\ &+ \big(-p\rho_e^{p-1}(E_0 - E_{min})\mathbf{u_e}^T\mathbf{k}_0\mathbf{u_e}\big) \cdot w_c \cdot c_2\end{aligned} \tag{4.37}$$

An irregular mesh will be generated to solve the shape control problem of the morphing wing, featuring a smooth boundary to accurately represent the wing skin. The mesh elements, varying in shape and size, can influence the total volume calculation. To ensure consistency and accuracy, it is crucial to account for these differences when calculating the volume fraction and its derivative.

The sensitivity of the material volume fraction constraint is given by:

$$\frac{\partial}{\partial \rho_e}\sum_{i=1}^{N}\rho_e v_e = v_e \tag{4.38}$$

where the element volume v_e corresponds to the element area A_e in a 2D problem.

4.1.6 Filtering and intermediate density elimination

To avoid checkerboard patterns and ensure the optimized topology can be manufactured, a sensitivity filter described by Sigmund is implemented here [**85**].

$$\frac{\partial \hat{f}}{\partial \rho_e} = \frac{1}{\max(\gamma, \rho_e)} \cdot \frac{\sum\limits_{i \in N_e} H_{ei} \cdot \rho_i \cdot \frac{\partial f}{\partial \rho_i}}{\sum\limits_{i \in N_e} H_{ei}} \tag{4.39}$$

where $\frac{\partial \hat{f}}{\partial \rho_e}$ represents the modified sensitivity for the design variable ρ_e, ρ_e is the design variable for element e, and γ is a small positive number (typically $\gamma = 10^{-3}$) to prevent division by zero. N_e denotes the set of elements i such that the distance $\Delta(e, i)$ from element i to element e is smaller than the filter radius r_{min}. H_{ei} is the weight factor, defined as $H_{ei} = \max(0, r_{\text{min}} - \Delta(e, i))$, and $\frac{\partial c}{\partial \rho_i}$ is the original sensitivity of the objective function

with respect to the design variable ρ_i. Finally, r_{min} is the filter radius used to calculate the weighting of elements whose centroids fall within this value.

The filter adjusts the sensitivity of the objective function with respect to the design variables by incorporating the sensitivities of neighboring elements. This is achieved through a weighted averaging process, where the influence of each neighboring element is determined by its distance from the element under consideration.

For a regular mesh with elements of uniform shape and size, a constant filter radius r_{min} can be applied. However, when dealing with an irregular low resolution mesh for more complex optimization problems, a dynamic filter radius is required to adapt to variations in element shape and size. In this project, the filter radius is determined based on the element area, as illustrated in Figure 4.5. Each element is considered equivalent to a circle with the same area, where $r = \frac{\sqrt{A_e}}{\pi}$, and A_e represents the area of the e_{th} element. The filter radius is then defined as $r_{min} = \omega \cdot r$, where ω is a scaling factor that extends the filter to include the centroids of neighboring elements. The importance of this dynamic filter will be discussed later, particularly its role in improving irregular mesh topology optimization and eliminating intermediate density elements in shape control problems.

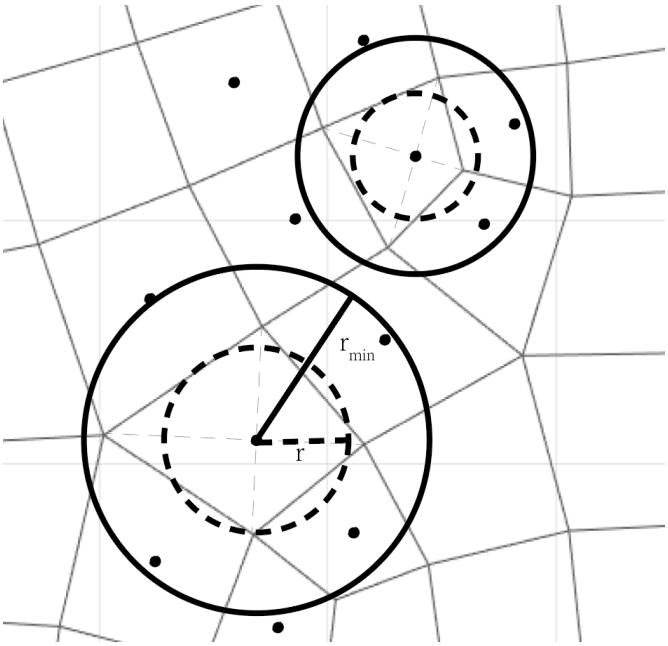

FIGURE 4.5. Dynamic filter radius

4.2 Code Verification and Results Comparison Using 4-Node Element Mesh

A finite element analysis (FEA) MATLAB code was developed to compute the displacement of the deformed airfoil under applied forces, taking into account variations in element area. The detailed equations are provided in Appendix Section 1. To verify the accuracy and performance of the code, a benchmark comparison was conducted using several standard optimization problems.

This section presents five cases. The first three cases compare random irregular meshes with regular meshes. The first two cases focus on compliance problems, while the third case addresses displacement inverter design. The later two case involves an airfoil-shaped mesh and compares the results with published code (Top88) and data, including minimum compliance and maximum displacement designs.

The Top88 is a compact MATLAB script created by Sigmund in 2011 to illustrate the essentials of density-based topology optimization [**81**]. In its default form it solves a classical minimum-compliance problem. Each iteration assembles a sparse global stiffness matrix, performs a finite-element analysis, evaluates element-wise sensitivities, filters those sensitivities to suppress checker-boarding, and then updates the densities with an Optimality-Criteria move limit. Because of this clarity and extensibility, top88 has become the “hello-world” of topology optimization and is still widely cited. The development of the code in this thesis is based on the algorithm and code structure introduced in the top88 code.

4.2.1 Case 1

In Case 1, the design domain is a square, with the left edge fixed against a wall and a single force applied at the right bottom node in the downward direction. Figures 4.6a and 4.6b show the design domain and the result generated using the Top88 code. Figures 4.7a and 4.7b illustrate the results for two different randomly generated irregular 50x50 meshes.

Additionally, Figures 4.7c and 4.7d display the results for two different mesh sizes. c is the strain energy to be minimized.

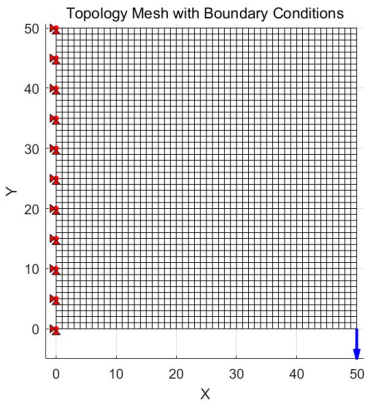

(A) Case 1 boundary conditions

(B) Top88 result c=0.0353mJ

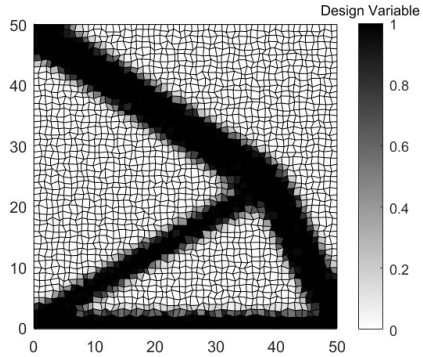

(A) Random mesh 1 with 50 by 50 mesh c = 0.0344mJ

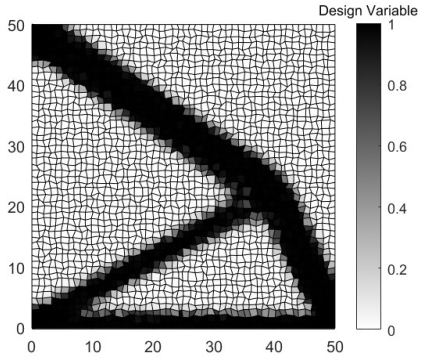

(B) Random mesh 2 with 50 by 50 mesh c = 0.0347mJ

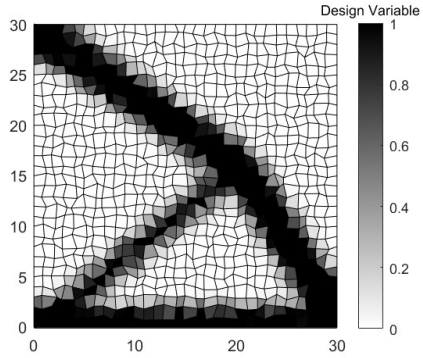

(C) Random mesh 3 result with 30 by 30 mesh c = 0.0370mJ

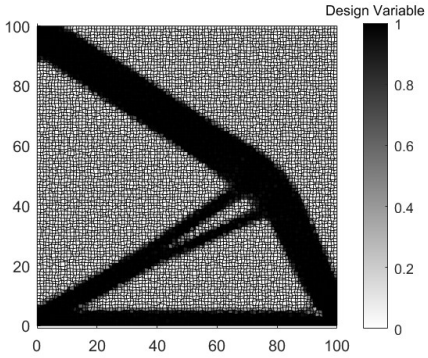

(D) Random mesh 4 result with 100 by 100 mesh c = 0.0340mJ

FIGURE 4.7. Case 1 minimum compliance design

4.2.2 Case 2

In Case 2, the design domain is rectangular, with the left edge fixed to a wall and a single force applied at the middle node of the right edge in the downward direction. Figures 4.8a and 4.8b illustrate the design domain and the result generated using the Top88 code. Figures 4.8c and 4.8d display the results for two different randomly generated irregular 120x40 meshes. Additionally, Figures 4.8e and 4.8f show the results for two different mesh sizes.

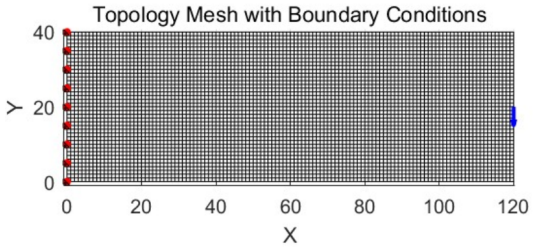

(A) Case 2 boundary conditions

(B) Top88 result c=0.3386mJ

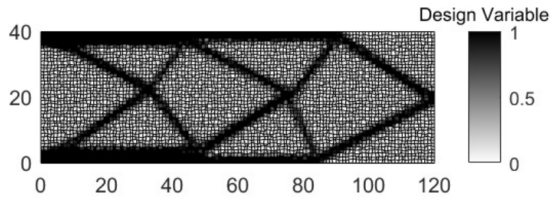

(C) Random mesh 1 with 120 by 40 mesh c = 0.3187mJ

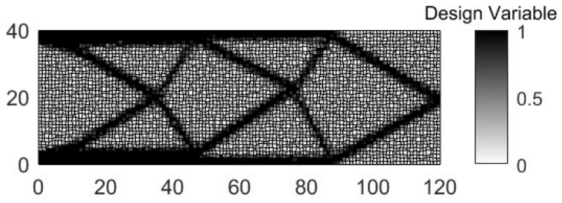

(D) Random mesh 2 with 120 by 40 mesh c = 0.3187mJ

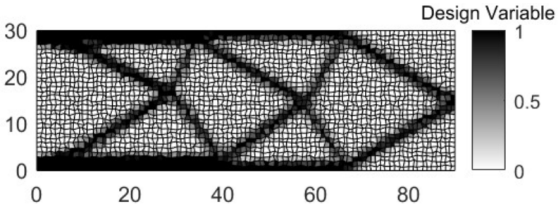

(E) Random mesh 3 result with 90 by 30 mesh c = 0.3607mJ

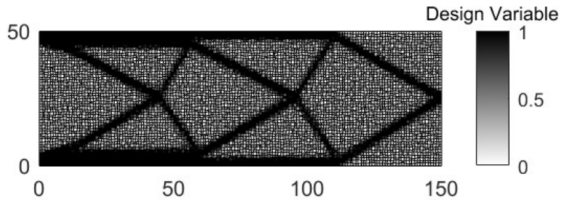

(F) Random mesh 4 result with 150 by 50 mesh c = 0.2969mJ

FIGURE 4.8. Case 2 minimum compliance design

4.2.3 Case 3

Case 3 involves a rectangular design domain focusing on displacement inverter design. The top left node is fixed to a wall, and the y-direction displacement of the bottom edge nodes

is constrained. A single force is applied to the lower left node in the left direction, while a virtual load is applied to the lower right node in the right direction. Figures 4.9a and 4.9b illustrate the design domain and the result generated using the Top88 code. Figures 4.9c and 4.9d display the results for two different randomly generated irregular 60x30 meshes. Additionally, Figures 4.9e and 4.9f show the results for two different mesh sizes.

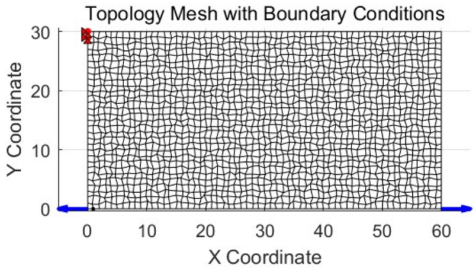

(A) Case 3 boundary conditions (irregular mesh)

(B) Top88 result c=10.76mm

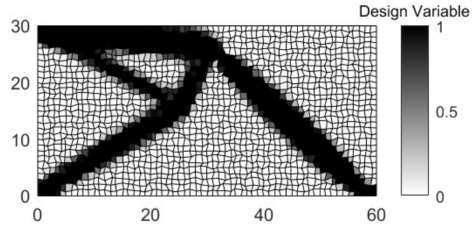

(C) Random mesh 1 with 60 by 30 mesh c = 10.21mm

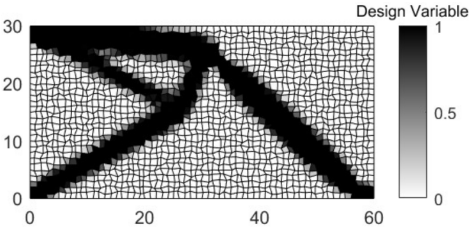

(D) Random mesh 2 with 60 by 30 mesh c = 10.14mm

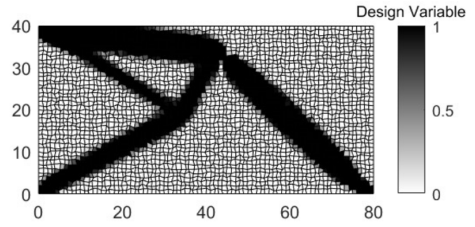

(E) Random mesh 3 result with 80 by 40 mesh c = 10.08mm

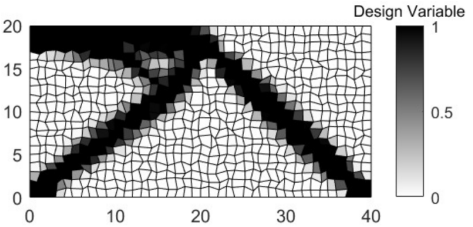

(F) Random mesh 4 result with 40 by 20 mesh c = 10.22mm

FIGURE 4.9. Case 3 minimum compliance design

4.2.4 Case 4

Case 4 utilizes the NACA 0021 airfoil leading edge shape to determine the optimal topology under aerodynamic load. Figure 4.10 presents the result from Srinivas et al. [**80**]. Figure 4.11

shows the result generated using the newly developed code, which exhibits a similar material distribution with a different filter applied.

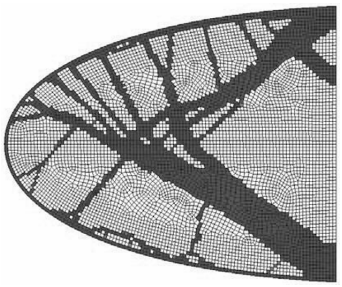

FIGURE 4.10. Maximum stiffness design from publication [**80**]

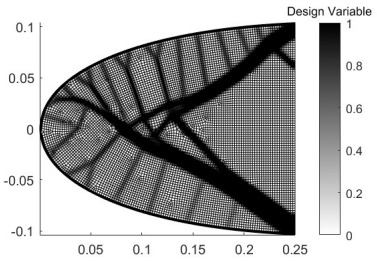

FIGURE 4.11. Maximum stiffness design using new code

4.2.5 Case 5

Case 5 uses the NACA 0021 airfoil leading edge shape to maximize displacement at the leading edge node. Figure 4.12 presents the result from Srinivas et al, which generated a maximum y-direction displacement -27 mm. [**80**]. Figure 4.13 shows the result generated using the new code. While the material distribution is nearly identical, a slight difference is observed due to a different optimization method and FEA solver compared to the one in the publication. However, a larger y-direction displacement at the output point is observed which is -29.8 mm.

FIGURE 4.12. Maximum displacement design from publication [**80**]

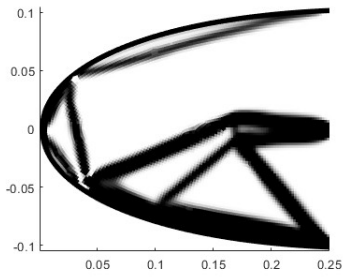

FIGURE 4.13. Maximum displacement design using new code

Five benchmark cases were chosen because they collectively exercise every classical behaviour a 4-node FEM topology optimizer must capture.

Case 1, the square cantilever with a tip load, checks pure bending;

Case 2, a rectangular plate with a central edge load, introduces combined bending and shear in a $3{:}1$ aspect-ratio domain;

Case 3, the displacement inverter, verifies the virtual-load / virtual-displacement formulation by demanding a sign-reversing output;

Cases 4 and **5** transfer the algorithm to a curved NACA-0021 leading edge, testing, respectively, minimum compliance and maximum tip deflection.

For *Cases 1–3* the present code reproduces the top88 layouts within $\pm 10\,\%$ compliance or ± 1 mm displacement, confirming mesh independence and demonstrating that the area-weighted sensitivity filter suppresses checker-boarding even on irregular grids.

In *Case 4* the solver matches the stiffest topology reported by Srinivas *et al.* with $< 5\,\%$ compliance error, though the adaptive filter yields a slightly thicker material band near the leading edge. In *Case 5* it attains a -29.8 mm tip deflection versus the literature value of -27 mm; the additional 2.8 mm implies greater flexibility but may reduce local buckling margins, so a nonlinear or eigen-buckling check is advisable.

Overall, the suite confirms that the solver and virtual-load formulation are correct and that the curved-mesh filter is effective, while highlighting the need to fine-tune filter radius and objective weighting for airfoil geometries.

4.3 Implementation of the shape control formulations using SIMP method

To design the shape control mechanism for achieving the target airfoil profile, an algorithm has been developed that integrates topology optimization with finite element analysis (FEA). The algorithm, implemented in MATLAB, includes airfoil shape data pre-processing, aerodynamic load calculations, topology optimization, FEA, and post-processing. By adjusting various

design parameters and boundary conditions, the resulting topology will exhibit different performance characteristics.

4.3.1 Flow chart and algorithm development

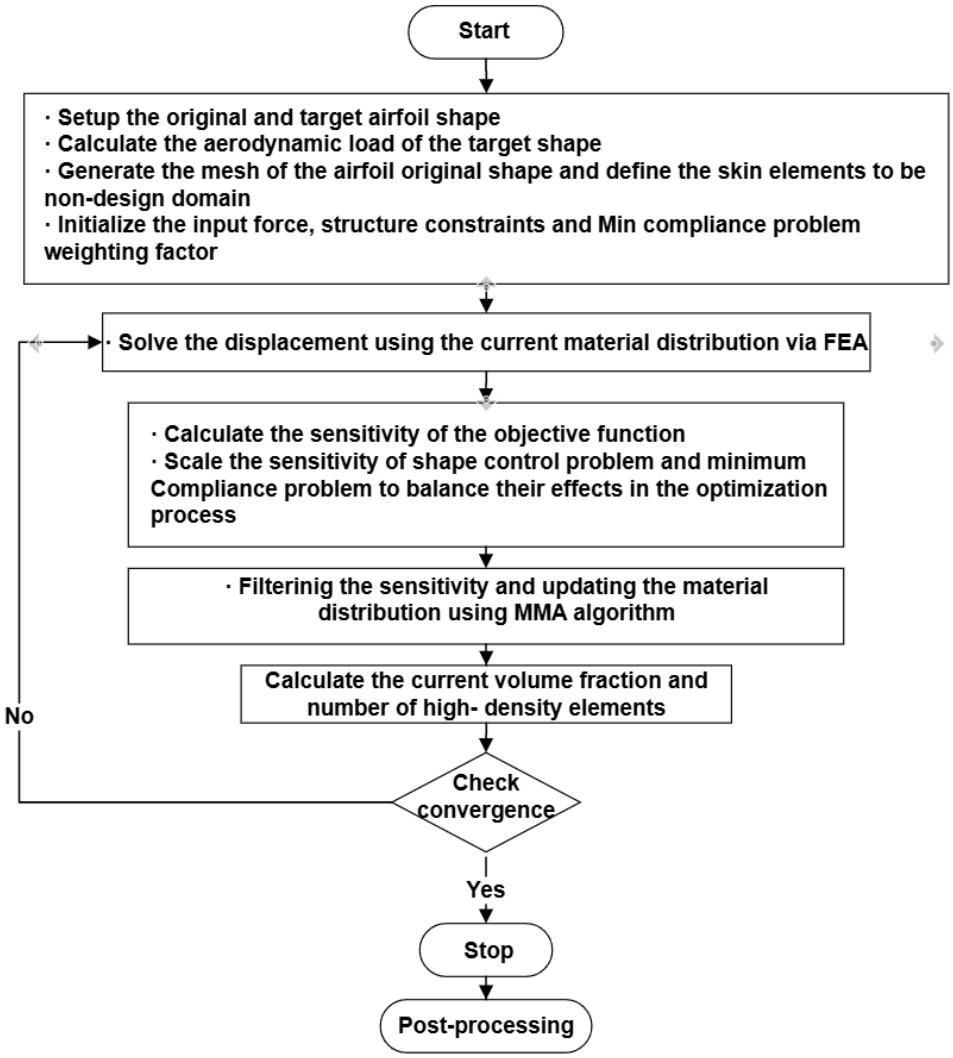

FIGURE 4.14. End-to-end algorithm for morphing-wing shape control. The flow chart shows data pre-processing, finite-element analysis loop, topology update, and post-processing that produces a fitted result for further analysis and validation.

This section discusses the impact of design parameters on the final topology and offers solutions to mitigate slow convergence. The parameter studies will prove the benefits of using combined (Multi) objective function to design morning airfoils, providing more possibilities to control the structure stiffness and shape fitting error. The resultant topology will be converted to CAD model and tested using commercial software. Finally, the 2D morphing wing is tested under different flight conditions using XFOIL, which calculates the optimal input force to achieve the most efficient configuration with optimized performance.

Figure 4.14 shows the flow chart for designing the internal structure of the morphing wing. The code is generated in MATLAB and the flow chart is used as a guidance to generate the program. ANSYS and XFOIL are used to generate mesh and airfoil aerodynamic parameters. The FEA code focuses on solving the 4-node element FEA problem and has been verified using a few cases.

Below are the objective function and its derivative derived:

Objective function

$$\text{Min } f(\rho) = \sum_{i=1}^{n} \left((u_{x,t,i} - u_{x,i})^2 + (u_{y,t,i} - u_{y,i})^2 \right) \cdot (1 - w_c) \cdot c_1 + \mathbf{F}^T \mathbf{U} \cdot w_c \cdot c_2 \quad (4.40)$$

Sensitivity of objective function

$$\begin{aligned} \frac{\partial f}{\partial \rho_e} = & \sum_{i=1}^{n} (-2p(E_0 - E_{min}) \cdot \big((u_{x,i} - u_{x,t,i}) \cdot p\rho_e^{p-1} \mathbf{v}_{e,x}^T \mathbf{k_0} \mathbf{u}_{e,x} \\ & + (u_{y,i} - u_{y,t,i}) \cdot p\rho_e^{p-1} \mathbf{v}_{e,y}^T \mathbf{k_0} \mathbf{u}_{e,y} \big) \cdot (1 - w_c)) \cdot c_1 \\ & + \left(-p\rho_e^{p-1} (E_0 - E_{min}) \mathbf{u_e}^T \mathbf{k}_0 \mathbf{u_e} \right) \cdot w_c \cdot c_2 \end{aligned} \quad (4.41)$$

The detailed solution strategies are as follows:

(1) Based on the aerodynamic design objective, calculate the optimal airfoil external profile. In this case, the optimization aims to maximize the endurance of a propeller-driven aircraft by maximizing the parameter $\frac{C_L^{\frac{3}{2}}}{C_D}$.

(2) To simulate the load condition of the deformed configuration, the aerodynamic load corresponding to the target airfoil profile is applied, assuming that the target shape is achieved.

A 2D quadrilateral mesh is generated using commercial software ANSYS, and the resulting mesh data is imported into MATLAB for further analysis.

(3) Generate a smooth boundary mesh, suitable for wing design and aerodynamic analysis, while defining a portion of the design domain's elements as solid material to represent the wing skin.

(4) Using the generated mesh and interpolated material density, compute the displacement of each node via FEA.

(5) Calculate the displacement error in both the x and y directions using the proposed real-time error calculation method.

(6) Evaluate the objective function and its sensitivity. The sensitivity scales for shape control and minimum compliance problems may differ significantly, posing challenges in determining the appropriate weighting factor for the objective function. The sensitivity values are scaled using c_1 and c_2 to balance their effects.

(7) The method of moving asymptotes (MMA) is employed to update the design variables, as the sensitivity of the shape control component can be either positive or negative. The detailed formulations and open-source MATLAB code can be found in [**82**], [**83**], and [**84**]. Parameters controlling the objective and constraint function restrictions need to be adjusted to accelerate convergence.

(8) Convergence is achieved when the maximum change in the design variable ρ_e is less than 0.01, and the volume fraction constraint is satisfied when the number of solid elements ($\rho_e > 0.9$) exceeds the designated value.

Different from the typical minimum compliance and maximum displacement topology optimization problem, the input force scale needs to be determined carefully because the force scale affects the total strain energy and the dynamic of the mechanism. A specific range of force input are suitable since the program will adjust the material distribution and stiffness to adapt the expected shape.

4.3.2 Mesh Generation and Boundary Conditions

The 2D morphing wing design comprises two distinct design domains: the leading edge and the trailing edge. Two smooth boundary meshes are generated using ANSYS to simulate the airfoil's external profile. The element node coordinates and element node numbers are then imported into MATLAB to perform the topology optimization.

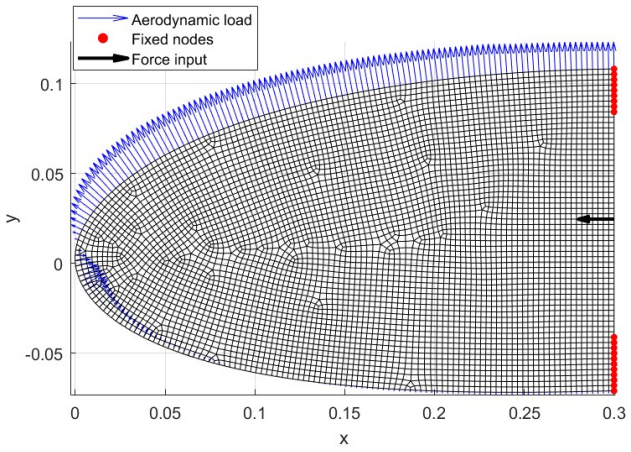

(A) Morphing wing leading edge design domain

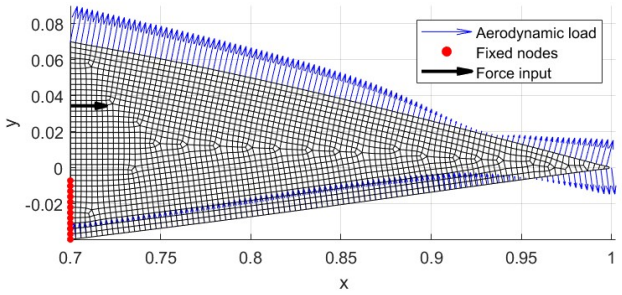

(B) Morphing wing trailing edge design domain

FIGURE 4.15. Discretised design domain using ANSYS

Figures 4.15 display the design domains with their respective meshes. The leading edge mesh contains 4920 elements, while the trailing edge mesh consists of 1910 elements. External elements are defined as non-design domains representing the morphing wing skin. The red dots indicate nodes fixed on the wall, and the black arrows show the direction of the force input. Note that only the lower root of the trailing edge is fixed, as the material typically used in aircraft is non-stretchable, requiring one surface to move freely to achieve the target shape.

A high-stiffness spring, with $k = 2 \times 10^4$, is attached at the input port in the horizontal direction to establish the load path between the input port and the observation points. The aerodynamic load is distributed along the external nodes of the airfoil mesh. The airfoil is assumed to have a thickness of 0.1 m in the spar direction and operates at a 5-degree angle of attack with a uniform flow. The aerodynamic performence is calculated using XFOIL with a viscous flow and $6 * 10^6$ Reynolds' number. These settings are good for XFOIL to provide converged results. The resultant pressure coefficients along the airfoil surface is output, allowing the pressure coefficient to be converted into force inputs at each node.

4.4 Results and Discussion

By applying the proposed formulation and varying the parameters in topology optimization, the resulting morphing wing topologies exhibit different performances, characterized by variations in displacement error, stiffness, and design clarity. The parameters to be tested and discussed include the displacement error measurement method, the compliance weighting factor, and the filter radius factor ω. The leading edge (LE) undergoes purely elastic body motion, while the trailing edge (TE) experiences both elastic and rigid body motion, depending on the boundary conditions. Therefore, the parameter settings will vary between the two cases. Figures 4.16 and 4.17 illustrate the initial topology, with a 25% volume fraction, meaning an initial density of 0.25 for each element. The skin elements are assigned a density of 1, and their corresponding sensitivity is set to zero to prevent unintended influence on the optimization process.

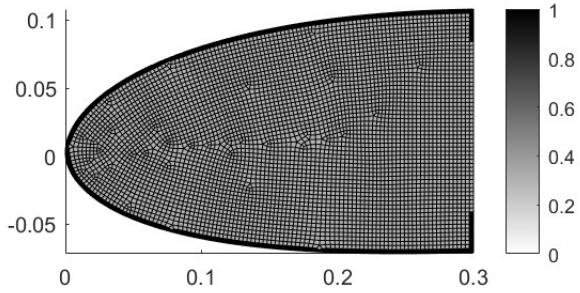

FIGURE 4.16. Initial leading edge topology

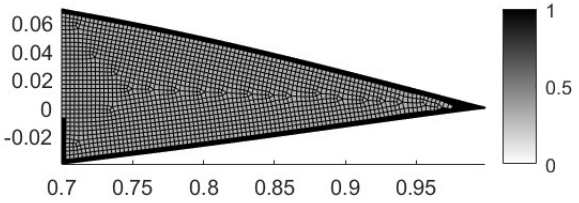

FIGURE 4.17. Initial trailing edge topology

4.4.1 Displacement Error Calculation Method Selection for LE

As mentioned, there are two methods to calculate the dynamic displacement error. Both methods are applied here to evaluate their advantages and disadvantages in the leading edge (LE) design. The design parameters for the two cases are as follows: $E_0 = 1.08 \times 10^9$ Pa, $w_c = 0.1$, $p = 3$, $F_{input} = -1000$ N, $v_{frac} = 0.25$, $c_1 = 5 \times 10^5$, $c_2 = 1 \times 10^3$, and $\omega = 1.8$. The results for the dynamic vertical plane (DVP) method are shown in Figure 4.18. The displacement error is minimized at the 115th iteration, the volume fraction constraint is satisfied at the 123rd iteration, and the minimum change in the design variable is achieved at the 197th iteration. The final displacement error is 0.0333 m, and the compliance is 7.67 J. The target geometry is nearly achieved, with a minor error located at the leading edge tip. Increasing the input force can further reduce this error, but it will slow down convergence. By analyzing the sensitivity function, the term $(u_{y,i} - u_{y,t,i})$ approaches zero as the current geometry gets closer to the target geometry, which causes the sensitivity function to diminish, thereby slowing the material update rate. A potential solution for improving both geometry accuracy and convergence speed is to increase the input force after the first convergence and continue running the program.

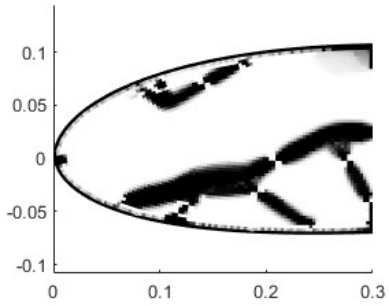

(A) LE topology using DVP

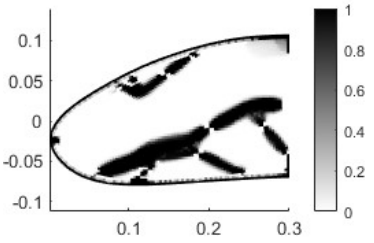

(B) Deformed topology using DVP

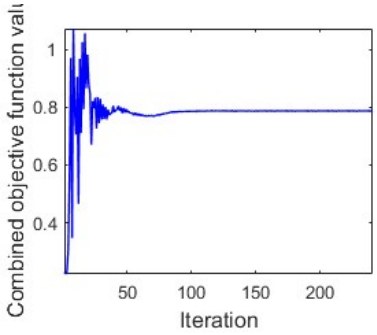

(C) Combined objective using DVP

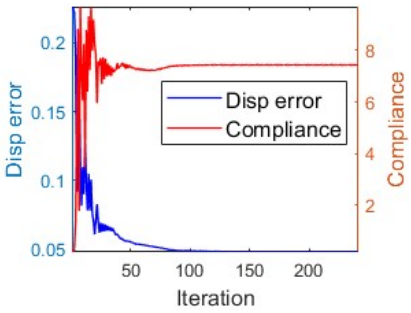

(D) Objective using DVP

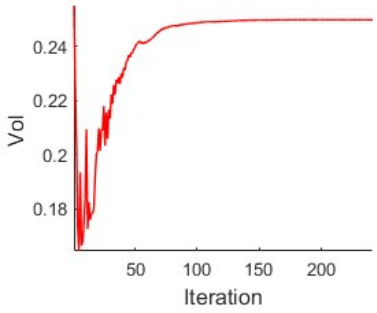

(E) Volume fraction using DVP

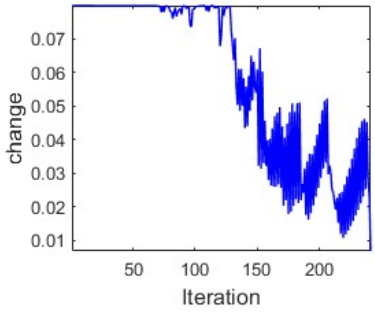

(F) Density change using DVP

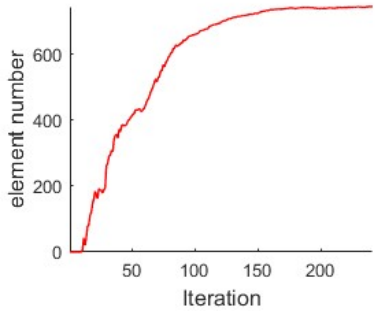

(G) High-density elements number using DVP

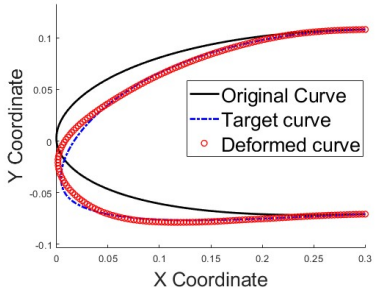

(H) Geometry fitting using DVP

FIGURE 4.18. Dynamic vertical plane method results details

The dynamic perpendicular-line (DPL) results are summarised in Fig. 4.19. The displacement error reaches its minimum at iteration 87, the volume-fraction limit is met by iteration 113, and convergence (minimal design-variable change) occurs at iteration 347. The final error is 0.0484 m with a compliance of 7.45 J. Compared with the dynamic vertical-plane (DVP) metric, DPL achieves a slightly lower compliance (7.45 J vs. 7.67 J) but a larger error (0.0484 m vs. 0.0333 m) and longer runtimes: 3.5 s per iteration and ≈ 690 s total, versus 2.2 s and ≈ 530 s for DVP.

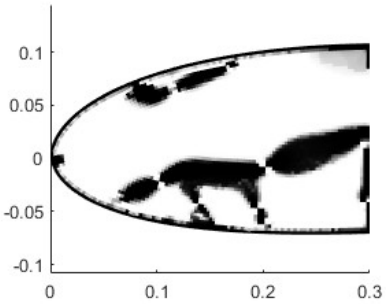

(A) LE topology using DPL

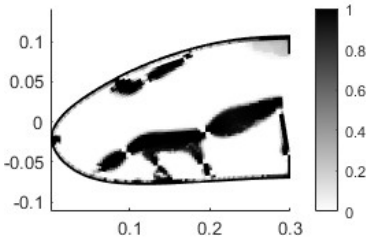

(B) Deformed topology using DPL

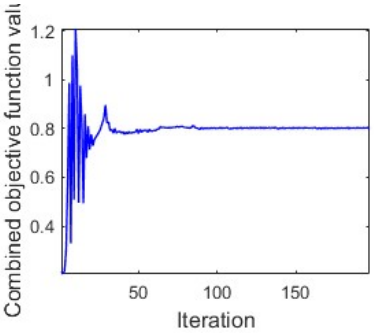

(C) Combined objective using DPL

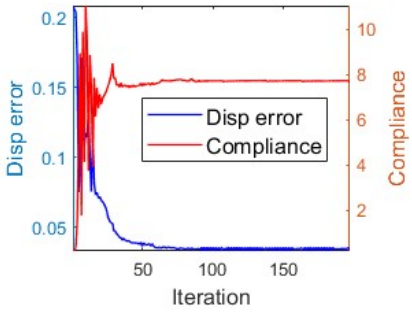

(D) Objective using DPL

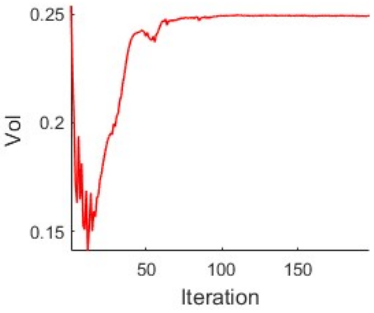

(E) Volume fraction using DPL

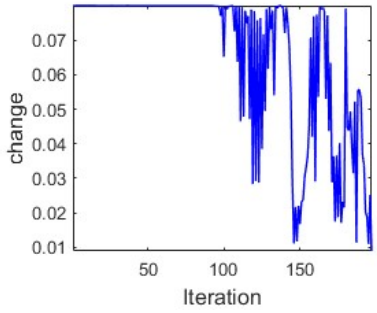

(F) Density change using DPL

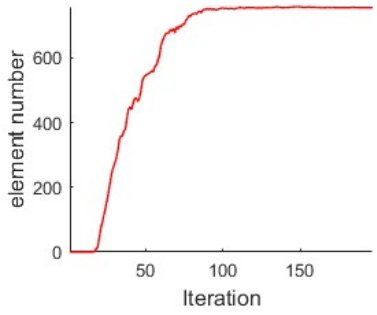

(G) High-density elements number using DPL

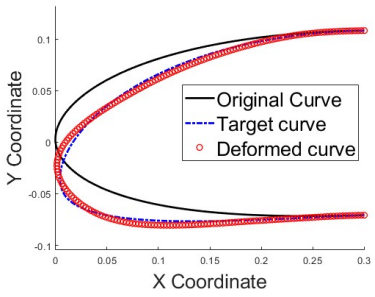

(H) Geometry fitting using DPL

FIGURE 4.19. Dynamic perpendicular line method results details

To achieve the best geometry fitting to enhance the performance, the dynamic perpendicular line method is preferred and will be used for further LE analysis.

4.4.2 Effects of compliance weighting factor for LE

In the next stage, the effects of the compliance weighting factor w_c are examined. The value of w_c ranges from 0 to 1, and 10 cases $(0.1, 0.2, \ldots, 1.0)$ are tested for comparison. Tables 4.1 and 4.2 show that increasing w_c leads to an increase in geometry-fitting error and a reduction in compliance. As w_c approaches 1, the design transitions smoothly from shape control optimization to minimum compliance design, controlled by the scaling factors c_1 and c_2 with appropriate values.

By evaluating topology quality, displacement error, and compliance, it is observed that cases with w_c between 0.1 and 0.4 exhibit acceptable topology quality and displacement error. The actual performance of these different designs will be analyzed and discussed in the following section. The w_c out of [0.1 0.4] would cause intermediate density materials and unmatched resultant shapes.

w_c	Topology	Geometry difference	Error (m)	Compliance (J)
0.1	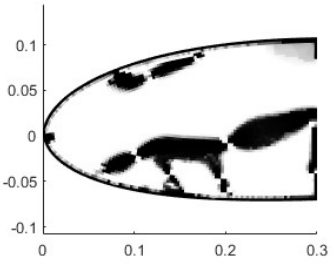	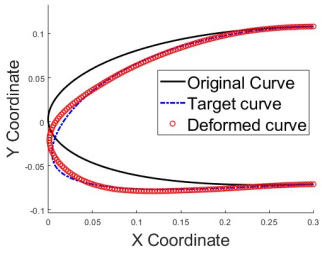	0.0333	7.67
0.2	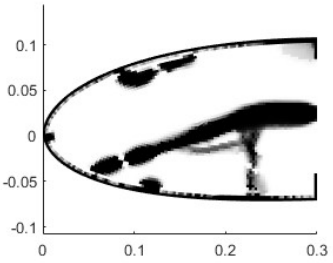	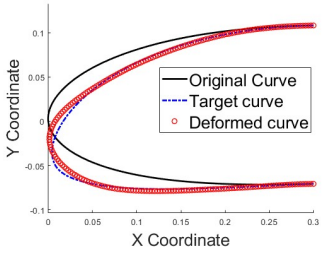	0.0349	7.98
0.3	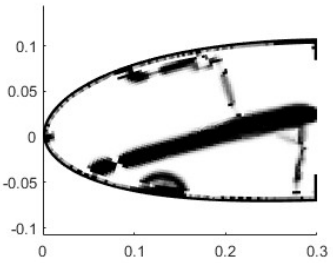	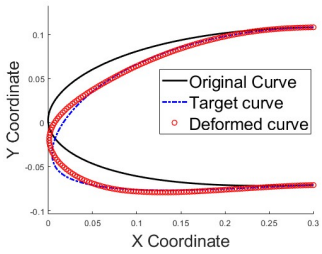	0.0376	7.82
0.4	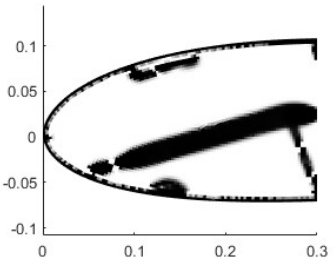	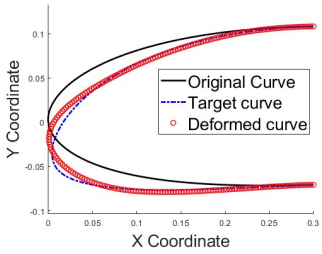	0.0391	6.99
0.5	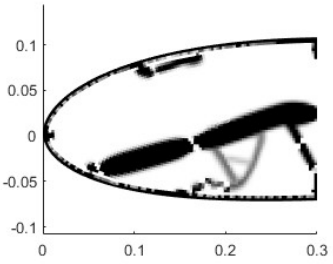	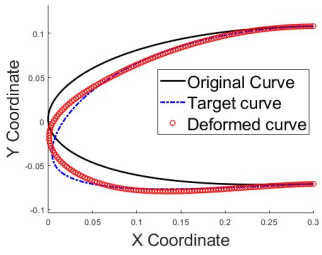	0.0472	5.91

TABLE 4.1. Effects of the compliance term weighting factor 0.1 - 0.5

w_c	Topology	Geometry difference	Error (m)	Compliance (J)
0.6	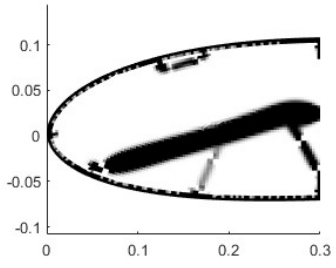	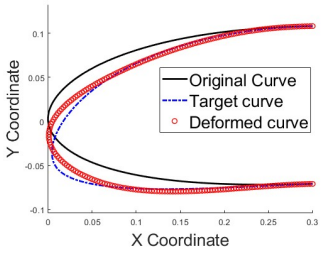	0.0539	5.26
0.7	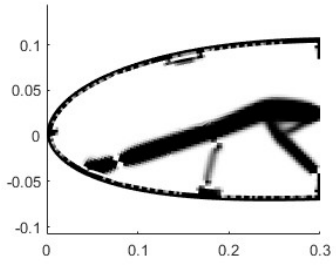	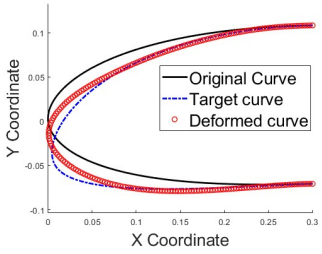	0.0613	4.62
0.8	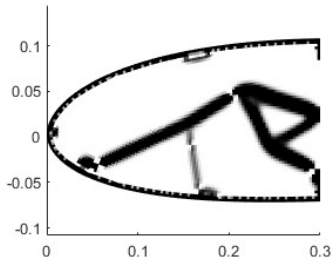	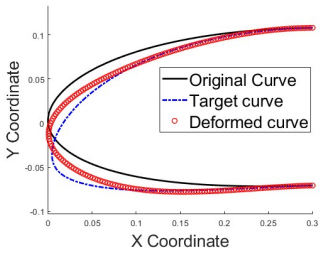	0.0697	3.73
0.9	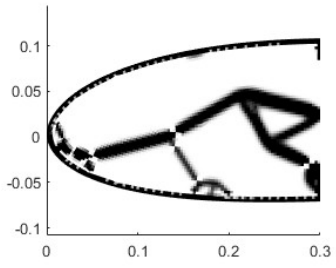	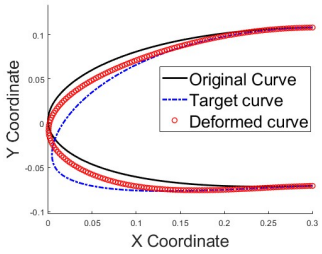	0.0968	2.18
1.0	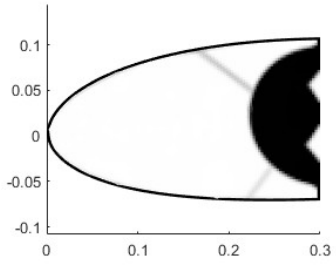	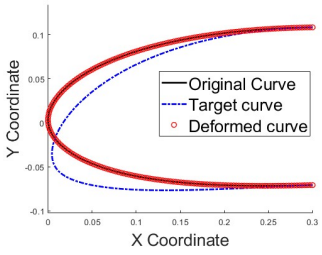	0.2071	0.005

TABLE 4.2. Effects of the compliance term weighting factor 0.6 - 1.0

4.4.3 Effects of filter radius factor

Different filter radius scaling factor ω is also tested and shown in table 4.3.

ω	Topology	Geometry difference	Error (m)	Compliance (J)
1.5	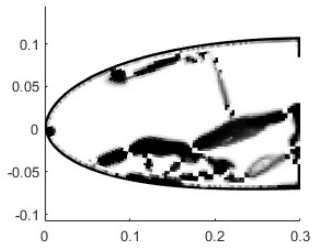	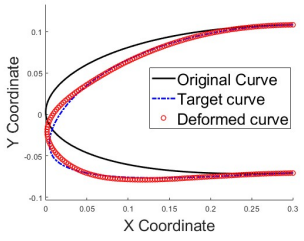	0.0323	7.55
1.8	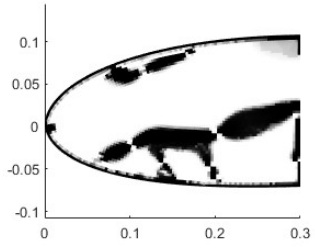	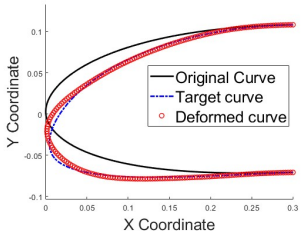	0.0333	7.67
2.1	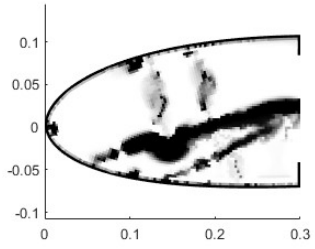	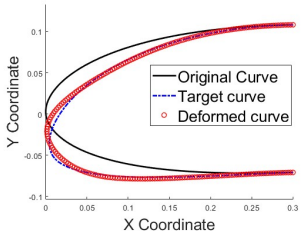	0.0320	8.71
2.4	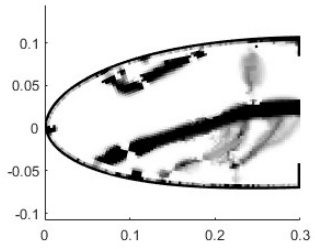	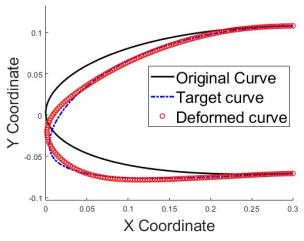	0.0317	8.81
2.7	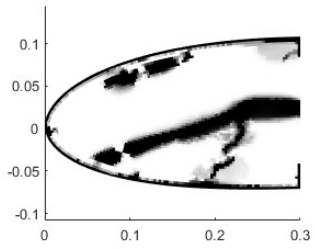	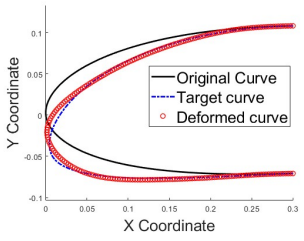	0.0349	8.78

TABLE 4.3. Effects of the filter radius scaling factor ω

It was observed that if the filter radius exceeds $1.8 \times \sqrt{A_e}$, some intermediate density elements become difficult to eliminate. This is one of the reasons for not using a constant filter radius for all elements. In shape control problems, thin but necessary structures are often required. If a constant large filter is used, as shown in Table 4.4, high-density elements representing thin structures become difficult to distinguish from intermediate density materials representing thicker structures, resulting in an unclear topology. On the other hand, using a constant small filter can reduce the number of intermediate density elements, but it leads to the formation of many de facto hinges or on-node hinges, which are challenging to convert into a solid model for testing. Therefore, an area-adapted filter, which adjusts the feature size based on the local element size, helps control these issues by reducing the number of hinges and intermediate density elements.

	$r_{min} = 0.003$	$r_{min} = 0.004$	$r_{min} = 0.005$
Topology	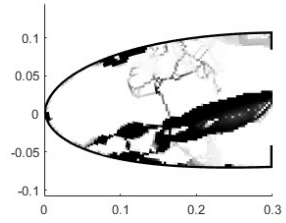	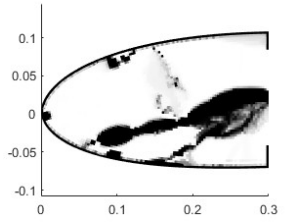	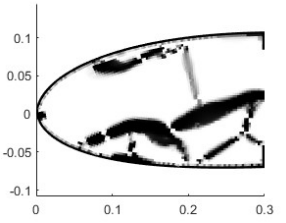
	$r_{min} = 0.006$	$r_{min} = 0.007$	$r_{min} = 0.008$
Topology	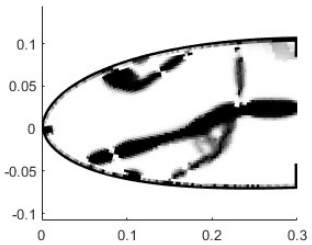	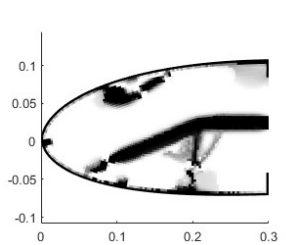	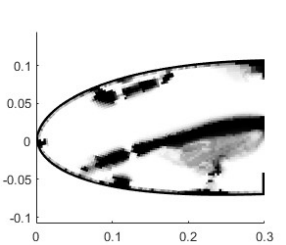

TABLE 4.4. Effects of the fixed filter radius r_{min}

4.4.4 Displacement error calculation method selection for TE

Similar to the method selection for LE, both of the two methods are tested on the trailing edge design. The design parameters setting for the two cases are: $E_0 = 1.08e9Pa$, $w_c = 0.1$, $p = 3$, $F_{input} = -650N$, $v_{frac} = 0.25$, $c_1 = 5e5$, $c_2 = 5e3$, $\omega = 1.2$.

The dynamic vertical plane method (DVP) results are shown in the figure 4.20. The displacement error is minimized at the 221 iteration, the volume fraction constraint is satisfied at the 342 iteration and the minimum change of design variable is satisfied at the 258 iteration. The program keeps running until the number of high-density element does not increase. The final displacement error is 0.0199m and the compliance is 5.77J.

To ensure a realized deformed shape, the trailing edge top left is not fixed to allow a rigid body motion. If both the top and bottom left of the airfoil are fixed, an elastic material is required and will cause insufficient stiffness to withstand aerodynamic load. Intelligent materials such as anisotropic material can be a suitable option but require a more complex FEA solver to calculate the required parameters. This thesis assumes that an elastic skin will cover the gap, allowing a continuous airfoil surface. The design of the elastic skin will not be introduced but similar technology has been mentioned in the FishBAC project [**15**].

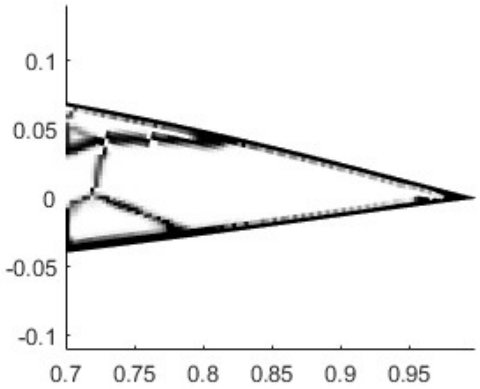

(A) TE topology using DVP

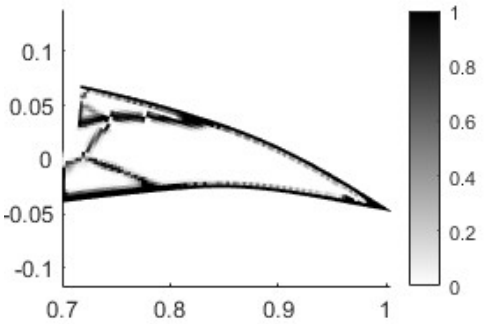

(B) Deformed topology using DVP

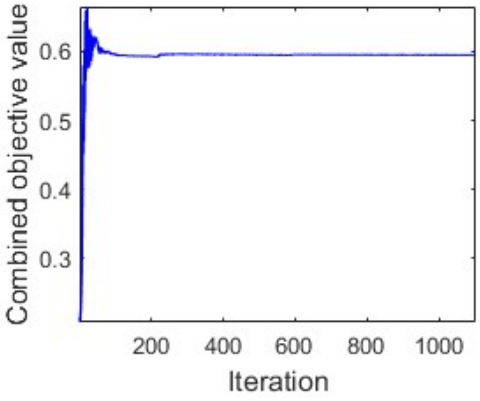

(C) Combined objective using DVP

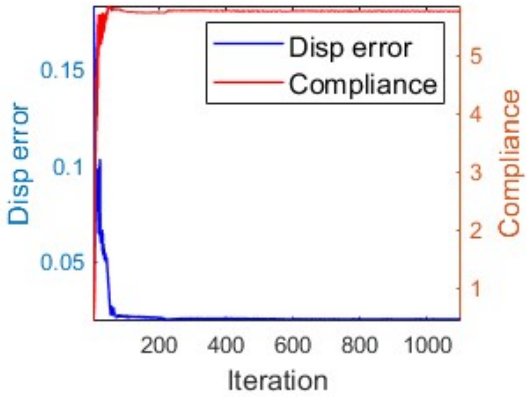

(D) Objective using DVP

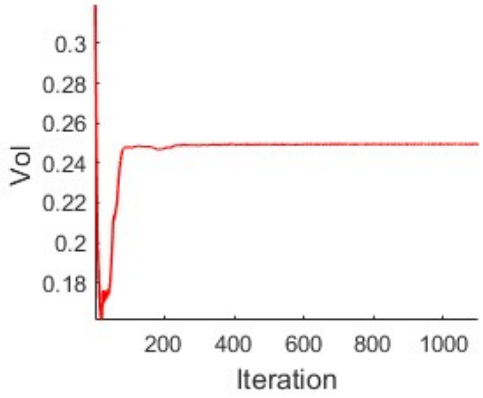

(E) Volume fraction using DVP

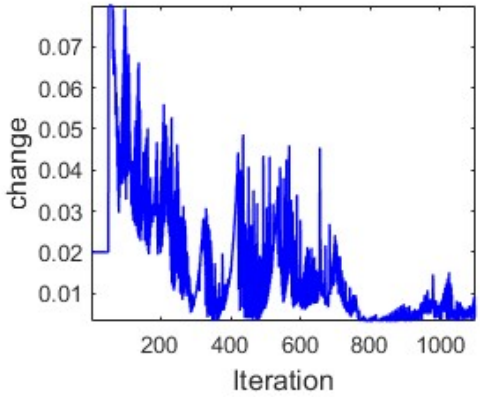

(F) Density change using DVP

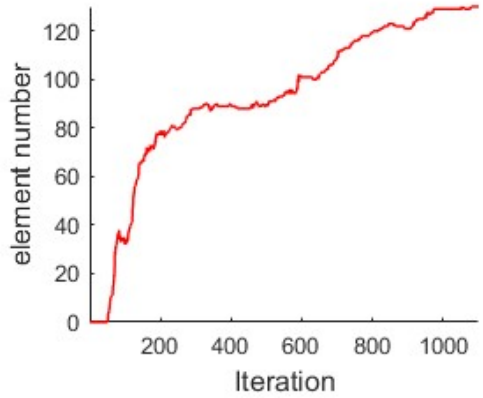

(G) High-density elements number using DVP

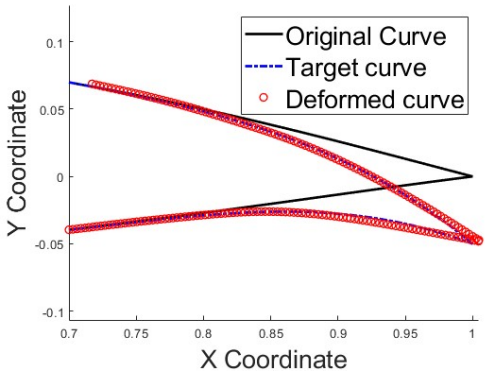

(H) Geometry fitting using DVP

FIGURE 4.20. Dynamic vertical plane method results details

The results of the dynamic perpendicular line (DPL) method are shown in Figure 4.21. The displacement error is minimized at the 356th iteration, the volume fraction constraint is satisfied at the 589th iteration, and the minimum change in the design variable is achieved at the 140th iteration. The program requires many iterations to reach a stable, converged result, due to the boundary conditions of the trailing edge. When using the DPL method, the measured x-direction displacement is smaller than the actual displacement, resulting in insufficient x-direction sensitivity.

The final displacement error is 0.0247 m, and the compliance is 5.62 J at the 1500th iteration. The comparison of the two TE examples shows that the dynamic vertical plane (DVP) method

achieves a smaller displacement error (0.0199 m < 0.0247 m) and slightly higher compliance (5.77 J > 5.62 J) than the dynamic perpendicular line method. Additionally, the DVP method requires fewer iterations to reach a converged result.

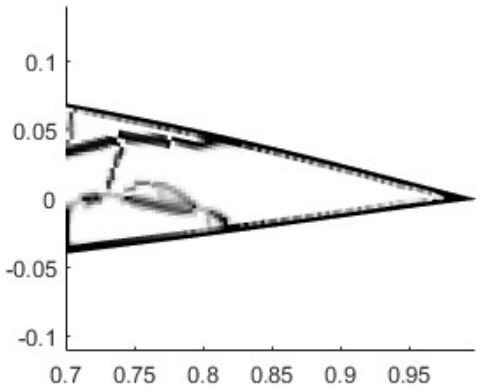

(A) TE topology using DPL

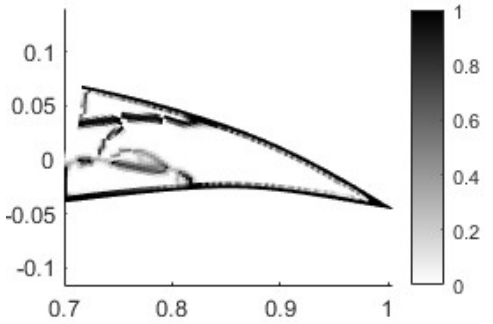

(B) Deformed topology using DPL

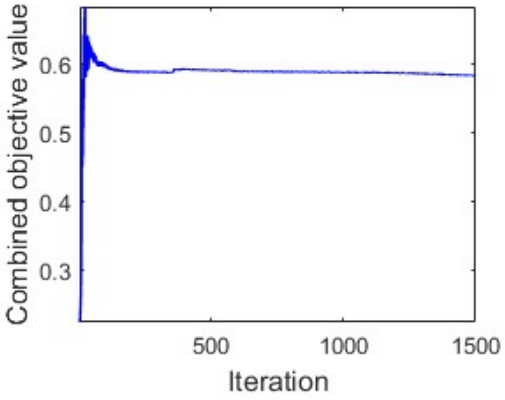

(C) Combined objective using DPL

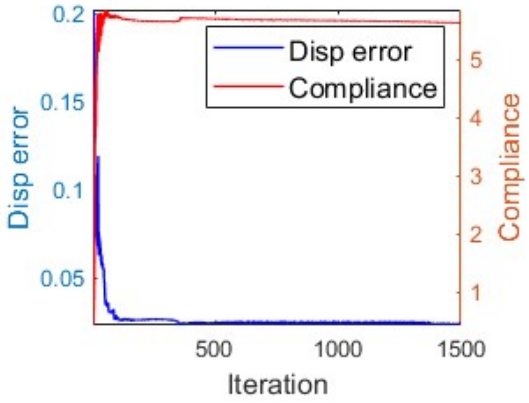

(D) Objective using DPL

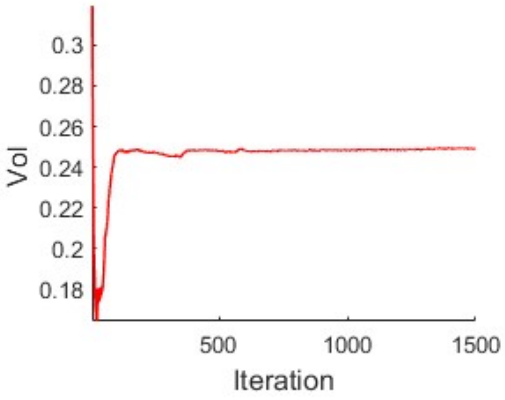

(E) Volume fraction using DPL

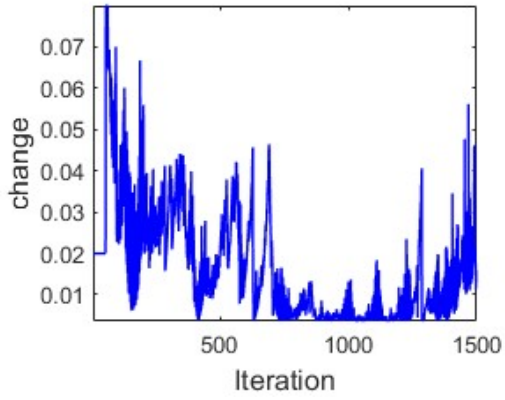

(F) Density change using DPL

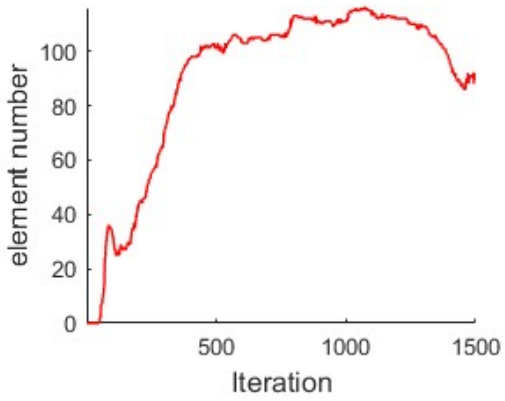

(G) High-density elements number using PL

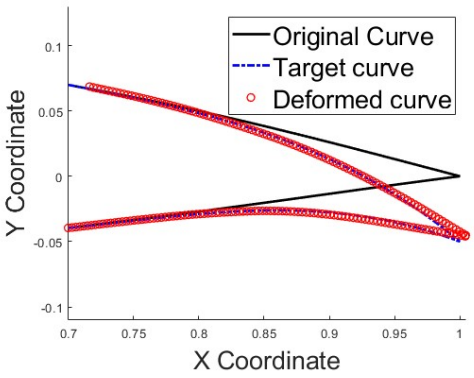

(H) Geometry fitting using PL

FIGURE 4.21. Dynamic perpendicular line method results details

In terms of computational cost, the average iteration time for the dynamic vertical plane (DVP) method is 0.6 seconds, while the dynamic perpendicular line (DPL) method takes 1.1 seconds per iteration. The total computation times for the two methods are 990 seconds and 1650 seconds, respectively. This is due to the number of virtual load cases in which the FEA solver needs to process. Considering the program's stability, the DVP method will be used for further trailing edge analysis.

4.4.5 Effects of Compliance Weighting Factor for TE

The effects of the compliance weighting factor w_c were also tested for the trailing edge and are shown in Tables 4.5 and 4.6. A similar trend to the LE design can be observed, where increasing w_c results in higher geometry-fitting error and reduced compliance.

By evaluating the topology quality, displacement error, and compliance, it is found that results with w_c between 0.1 and 0.5 exhibit acceptable topology quality and displacement error. w_c values out of the range [0.1 0.5] cause significantly different design and shape fitting errors, but a larger input force would change the appropriate range. The actual force required will be depend on the flow velocity and material selection, then the range of w_c will need an update.

w_c	Topology	Geometry difference	Error (m)	Compliance (J)
0.1	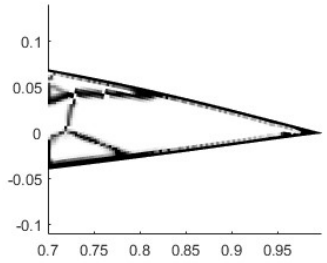	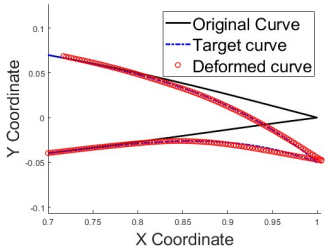	0.0199	5.77
0.2	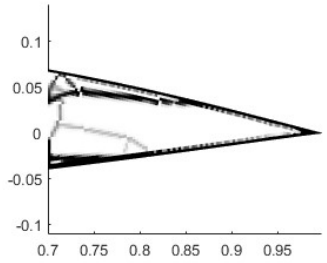	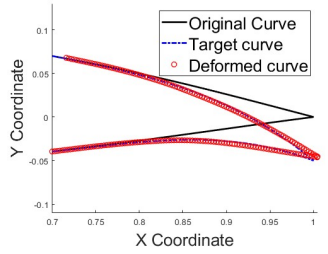	0.0216	5.61
0.3	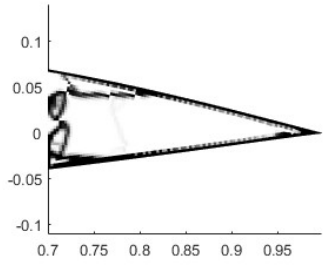	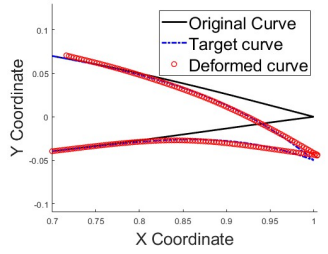	0.0278	4.22
0.4	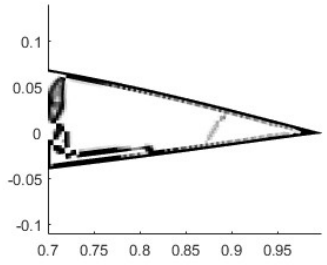	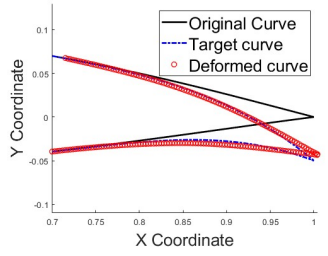	0.0294	3.39
0.5	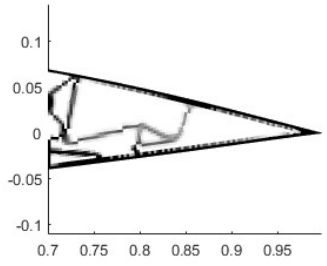	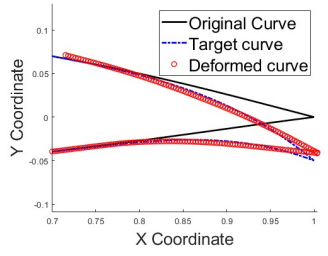	0.0412	3.37

TABLE 4.5. Effects of the compliance term weighting factor 0.1 - 0.5

w_c	Topology	Geometry difference	Error (m)	Compliance (J)
0.6	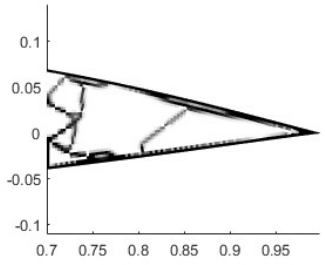	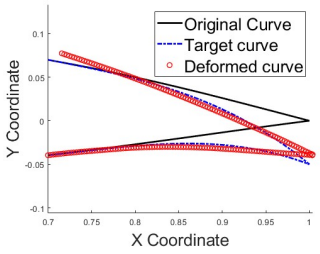	0.0486	1.97
0.7	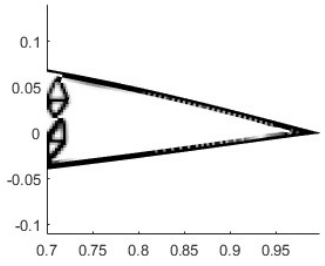	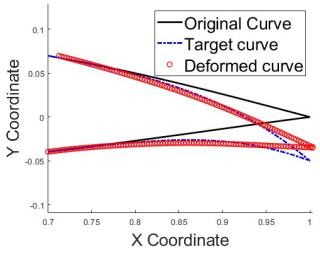	0.0572	2.81
0.8	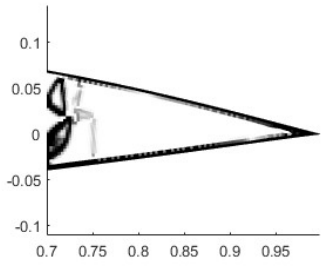	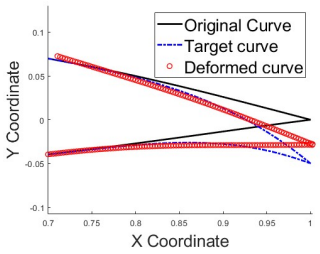	0.0768	1.88
0.9	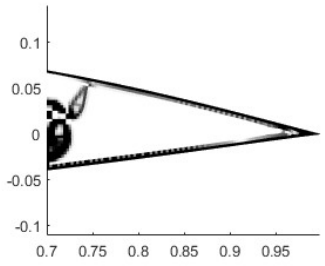	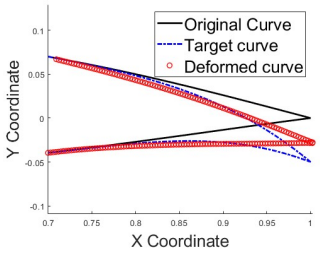	0.0809	1.09
1.0	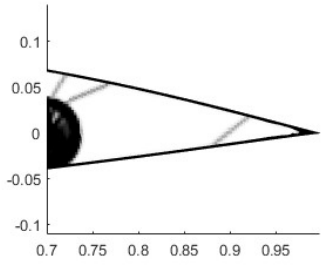	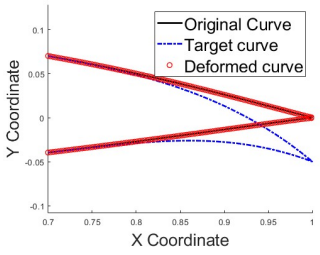	0.1975	0.02

TABLE 4.6. Effects of the compliance term weighting factor 0.6 - 1.0

4.4.6 Effects of filter radius factor

Different filter radius scaling factor ω is also tested and shown in table 4.7.

ω	**Topology**	**Geometry difference**	**Error (m)**	**Compliance (J)**
1.0* π	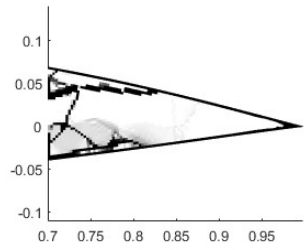	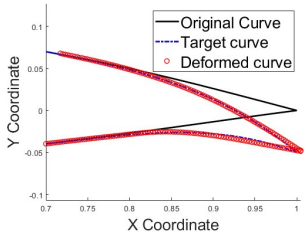	0.0191	5.65
1.2* π	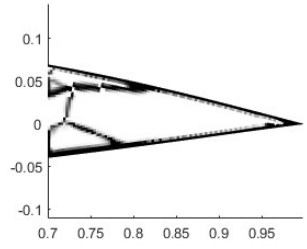	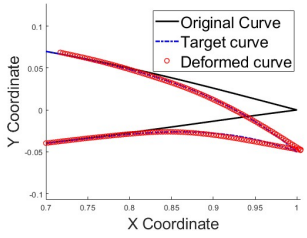	0.0199	5.77
1.4* π	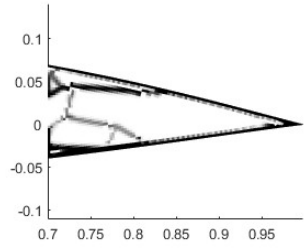	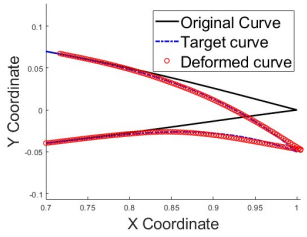	0.0191	5.68
1.6* π	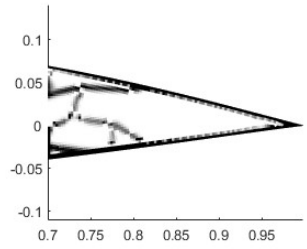	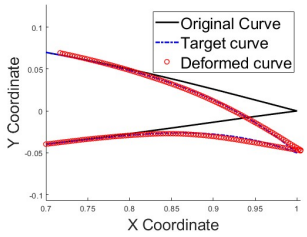	0.0218	5.69
1.8* π	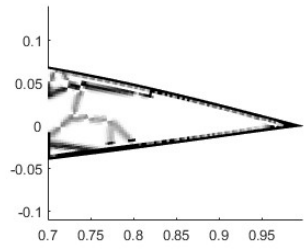	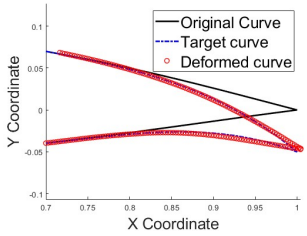	0.0223	5.70

TABLE 4.7. Effects of the filter radius scaling factor omega

Similar to the LE design cases, if the filter radius exceeds $1.2\pi \times \sqrt{A_e}$, it becomes difficult to represent thin structures using high-density elements. Conversely, if the filter radius is too small, the mesh-dependency problem becomes prominent. An area-adapted filter with $\omega = 1.2\pi$ is appropriate for the current mesh quality, ensuring a clear and well-defined topology.

In addition, the trailing edge topology optimization results take more iterations to converge compared to the leading edge results. This can be caused by: (1) Type of body motion. (2) Mesh quality including the number of elements and the type of element. (3) Direction of aerodynamic load.

4.4.7 Effects of the input force scale

To evaluate the effects of force input magnitude, larger force values were tested. Additionally, the compliance weighting factor was reduced to ensure acceptable shape fitting. Table 4.8 summarizes the effects of increased force inputs. The target shape was achieved with acceptable errors, and the resulting designs exhibited higher stiffness.

It is evident that increasing force inputs differs significantly from increasing weighting factors under limited, consistent force inputs, as shown in Tables 4.1 and 4.2. The program adjusts the stiffness to balance shape fitting with compliance minimization. This demonstrates that the newly combined objective function allows greater flexibility in designing morphing airfoils to meet various requirements and constraints, such as material properties and the operational conditions of the aircraft.

Furthermore, the designs generated with increased force inputs exhibit fewer hinges and intermediate-density materials. The application of finer mesh resolution or more stringent convergence criteria can further improve the results, thereby reducing challenges associated with manufacturing and performance analysis.

Force (N)	Topology	Geometry difference	Error (m)	Compliance (J)
170	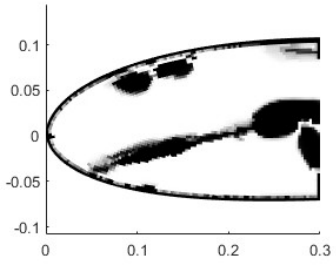	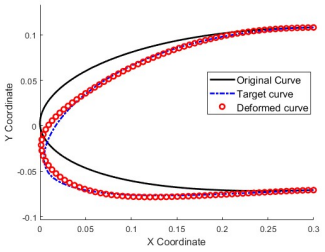	0.0287	13.37
210	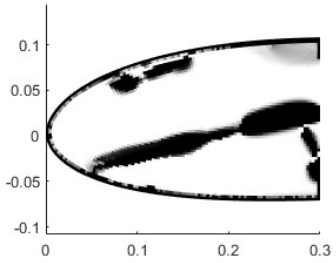	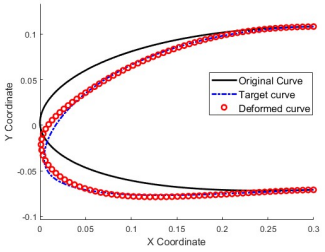	0.0276	16.04
250	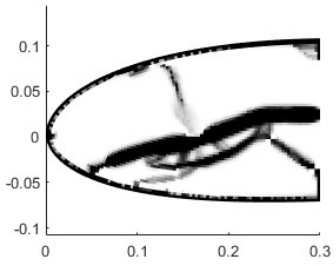	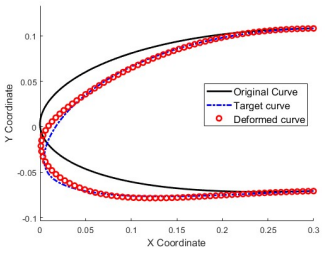	0.0269	19.10
270	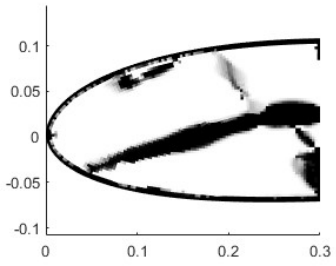	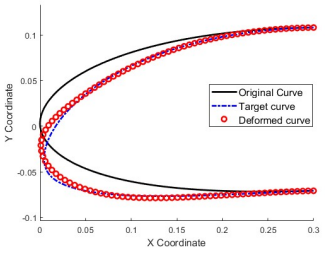	0.0276	19.78

TABLE 4.8. Effects of the force input scale 170N - 270N

4.4.8 Effects of the skin thickness

In the previous analysis, the outer layer was defined as the skin to transfer aerodynamic loads. To evaluate the effects of skin thickness on the design, the second and third outer layers of the trailing edge mesh were defined as skin in separate cases. As the fixed non-design domain

stiffness increases, larger input forces and smaller compliance weighting factors are required to achieve the desired results.

Table 4.9 summarizes the effects of increasing the number of skin layers. The results indicate that the stiffness of multi-layer designs increases significantly, require much larger input forces to achieve the target shape. However, the target shape can still be achieved with acceptable errors. For morphing airfoil designs using elastic materials, increasing the number of skin layers (or thickness) can be a viable option to enhance structural performance.

Layers	Topology	Geometry difference	Error (m)	Compliance (J)
1	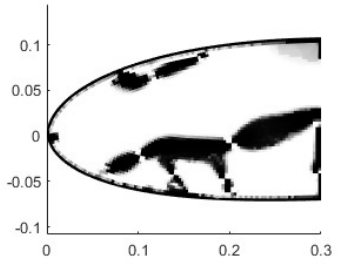	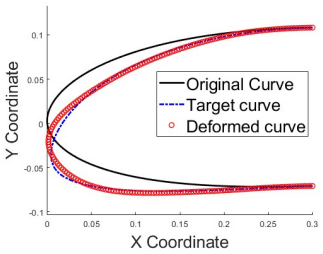	0.0333	7.67
2	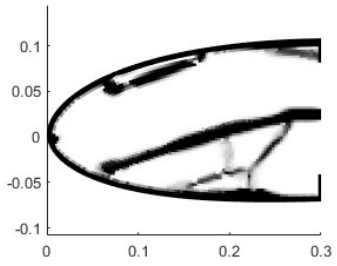	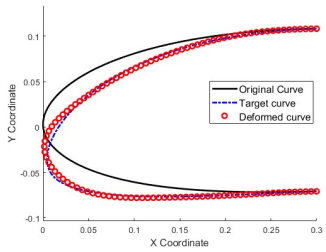	0.0249	72.99
3	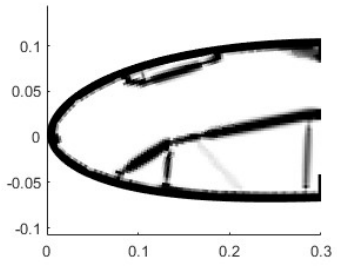	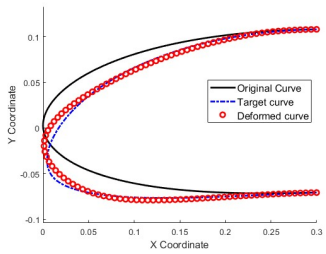	0.0416	109.98

TABLE 4.9. Effects of the number of skin layers

4.4.9 Effects of number of actuation

All previous cases utilized a single actuation to achieve the target shape. In this section, two additional cases involving two actuations are tested. For these cases, only the boundary

conditions are updated, with additional springs attached at the input ports to accommodate the increased number of actuations.

Table 4.10 presents the designs utilizing multiple actuations, with two single force inputs 100N and 150N attempted at each input port. The results indicate that the target shape can still be achieved with varying force inputs. However, the primary differences lie in the structural stiffness across different numbers of actuation and force input configurations. These tests validate the feasibility of using multiple actuations for designing morphing airfoils, providing greater flexibility in achieving desired aerodynamic performance under various design constraints.

Actuations	Force (N)	Topology	Geometry difference	Error (m)	Comp (J)
2	100N	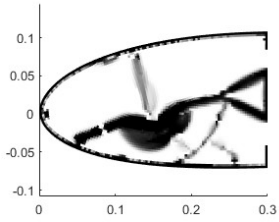	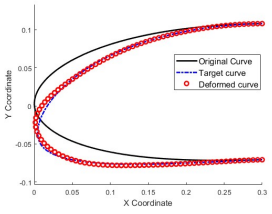	0.0333	7.67
2	150N	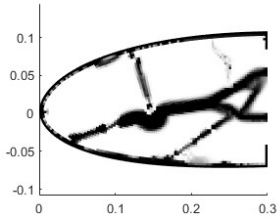	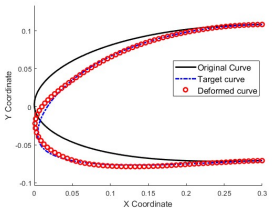	0.0223	24.27

TABLE 4.10. Effects of more actuations

4.4.10 Structure and Performance Analysis of the Combined Wing

To evaluate the generated topologies, the leading edge and trailing edge designs are converted into CAD models for structural testing. A simple algorithm was developed to extract the boundary nodes of the high-density elements from the topology. The steps are as follows:
(1) A density threshold in the range [0,1] is used to filter the high-density elements. Figure 4.22a shows the nodes of the elements with a density greater than 0.3.
(2) The boundary nodes of the high-density elements are then filtered to construct the model

shown in Figure 4.22b.

(3) The CAD model is created in ANSYS, with the same boundary conditions applied as in the topology optimization.

(4) The geometry difference between the ANSYS results and topology optimization results is compared by measuring the displacements at key nodes.

One leading edge and one trailing edge topology with good quality were selected for testing, and their converted CAD models are shown in Figures 4.22e and 4.22f. A density threshold of 0.3 was used, and some one-node hinges were modelled as thin hinges. The boundary nodes of those elements with density larger than 0.3 are selected to model the structure boundary.

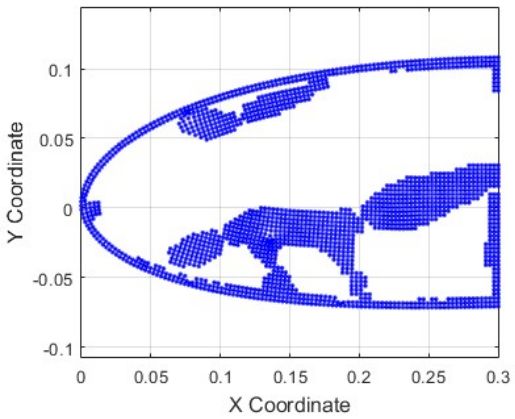

(A) Filtered LE high-density elements

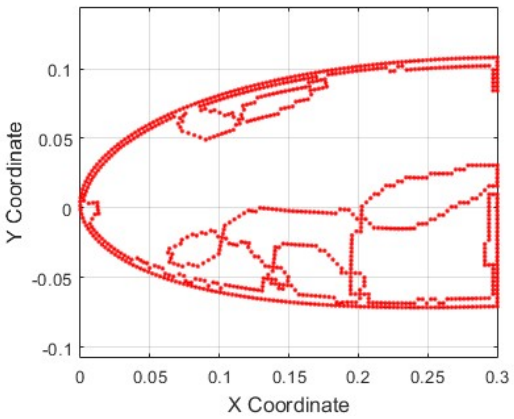

(B) Filtered LE high-density boundary nodes

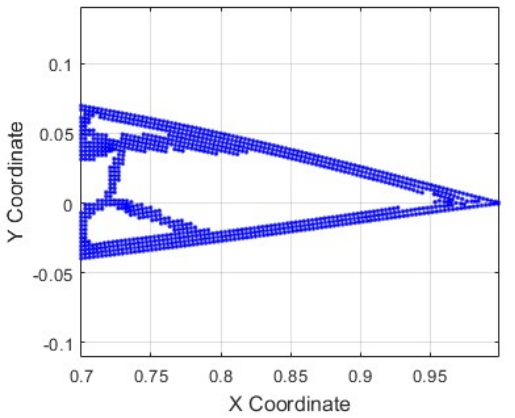

(C) Filtered TE high-density elements

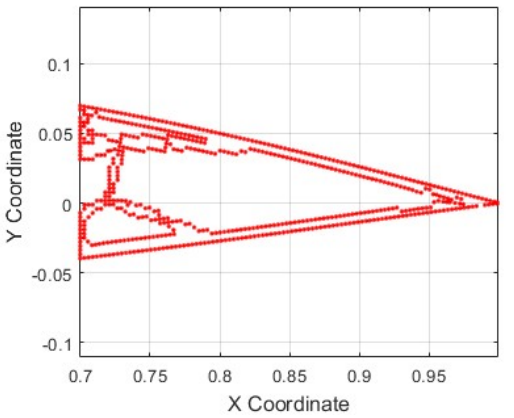

(D) Filtered TE high-density boundary nodes

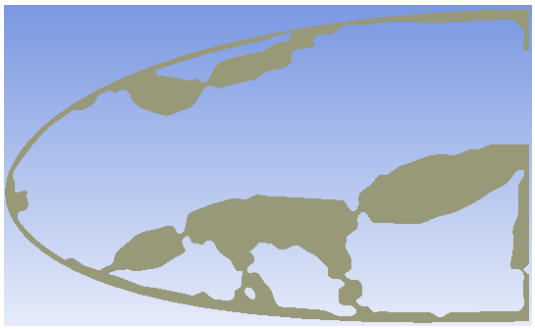

(E) Leading edge CAD model

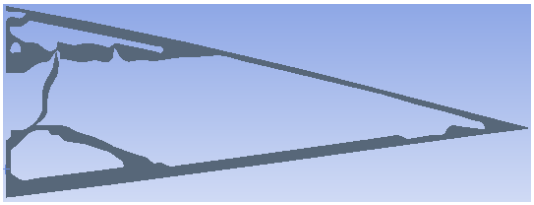

(F) Trailing edge CAD model

FIGURE 4.22. CAD model generation and testing

To accurately measure the difference between the topology optimization results and the FEA results of the converted model, the boundary coordinates of the deformed model are exported. Using the vertical perpendicular line method, the FEA errors compared to the target shape were measured and are presented in figure 4.23.

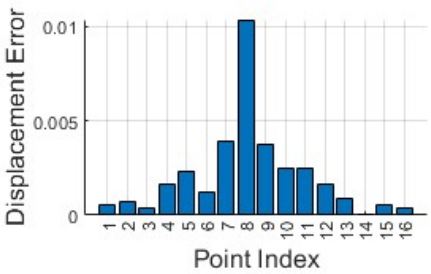

(A) Leading edge observation points displacement error

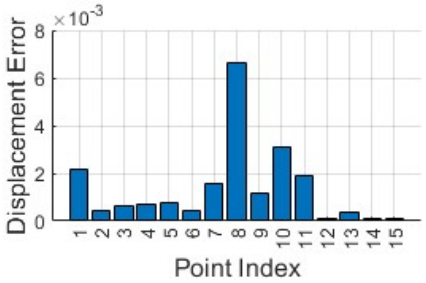

(B) Trailing edge observation points displacement error

FIGURE 4.23. Observation points displacement error measurements for leading and trailing edge

In the CAD model testing, no spring is attached at the input port. The material used is high-density polyethylene, with a Young's modulus of 1.08×10^9 Pa, which is the same material property used in the topology optimization. By applying the same fixed support conditions as in the topology optimization, the morphing leading edge and trailing edge are actuated under the applied force input. The deformed models are shown in Figure 4.24.

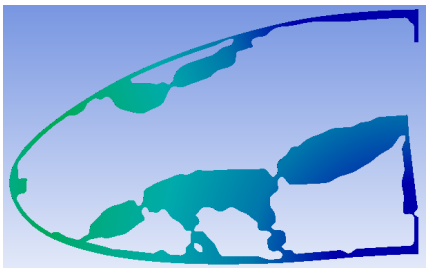

(A) Deformed leading edge model

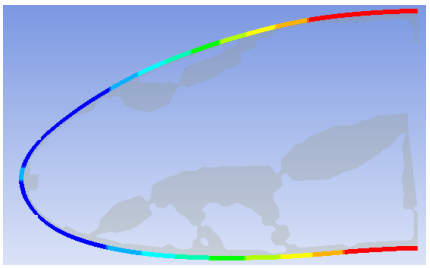

(B) Deformed leading edge model boundary coordinates

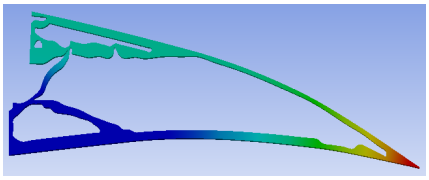

(C) Deformed trailing edge model

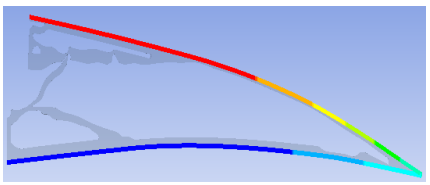

(D) Deformed trailing edge model boundary coordinates

FIGURE 4.24. FEA results with deformed model and model boundary coordinates

Figure 4.25 compares the target curve, the topology optimization resultant curve, and the FEA resultant curve. The FEA result of the converted CAD model differs slightly from the topology optimization curve due to the absence of intermediate density materials in the solid model, which alters the stiffness matrix. Additionally, the current model includes some one-node hinges that were artificially simulated as thin structures, which exhibit low stiffness and have risks to failure under high load conditions. This issue highlights the need for minimum feature control during topology optimization.

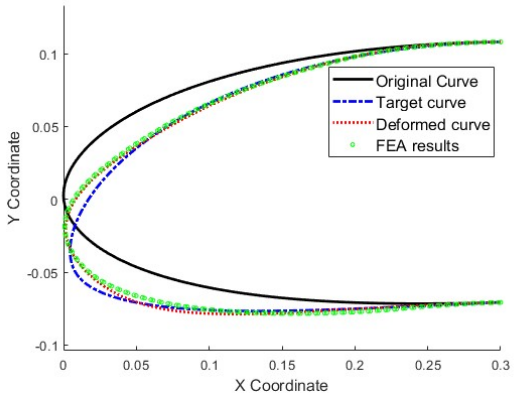

(A) Leading edge curves comparison

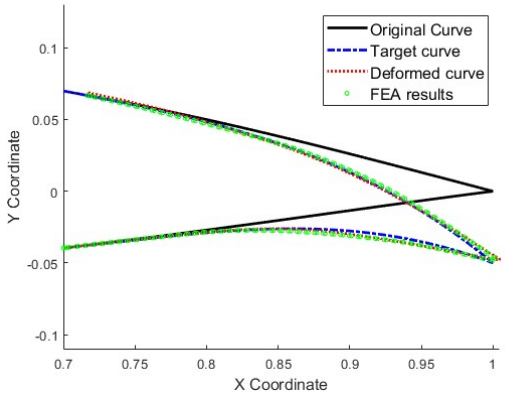

(B) Trailing edge curves comparison

FIGURE 4.25. Curves comparison of the target curve, topology optimization resultant curve and FEA resultant curve

4.4.11 Performance analysis of the optimized morphing wing

Since the baseline airfoil used for shape optimization is NACA2418, the maximum lift coefficient is compared between the baseline and the optimized morphing wing. Assuming that the 2-D airfoil is tested with fixed 5 degrees angle of attack, and $6 * 10^6$ Reynold's number using XFOIL. The algorithm uses differential evolution to update the input force and find the best configuration of the morphing wing to generate the best performance under specified design objectives. The baseline NACA2418 has $C_L = 0.807$, $L/D = 122.3$ and $L^{\frac{3}{2}}/D = 98.84$, while the optimized morphing wing can achieve $C_L = 1.754$, $L/D = 148.4$ and $L^{\frac{3}{2}}/D = 161.51$ after actuation shown in the figure 4.26.

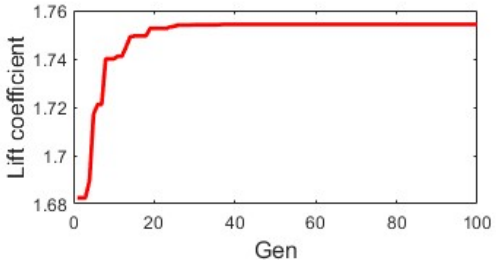

(A) Maximum lift coefficient configuration update history

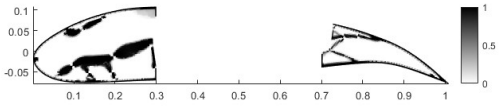

(B) Maximum lift coefficient configuration

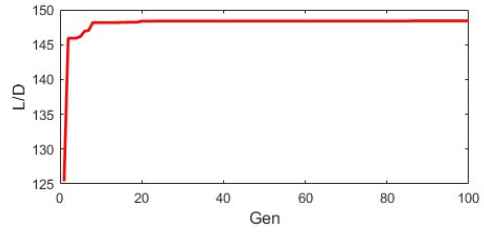

(C) Maximum lift to drag ratio configuration update history

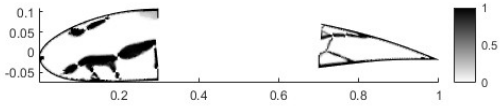

(D) Maximum lift to drag ratio configuration

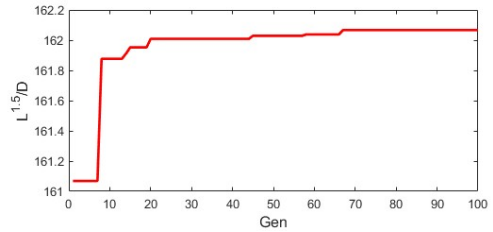

(E) Maximum endurance configuration update history

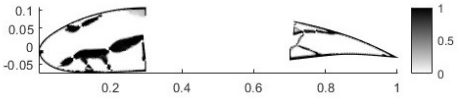

(F) Maximum endurance configuration

FIGURE 4.26. CFD results of the design 2-D morphing wing

4.5 Summary

The morphing wing design process integrates topology optimization and finite element analysis (FEA) to achieve precise shape control. The optimization process involves modifying the structure to meet specific aerodynamic objectives while maintaining structural integrity. Two key methods for displacement error calculation were tested: the dynamic vertical plane (DVP) method and the dynamic perpendicular line (DPL) method. Both methods aim to minimize the displacement error between the optimized and target airfoil shapes by adjusting material distribution.

The DVP method focuses on using a dynamic vertical plane that shifts with the observation point to measure displacement, whereas the DPL method uses a perpendicular line to the tangent at the observation point. Each approach has advantages: the DVP method tends to converge faster and with greater stability, while the DPL method provides more detailed

sensitivity to geometry changes. However, the DVP method's efficiency and accuracy, especially for complex designs like the trailing edge, made it preferable for further use.

Another important consideration in the optimization process is the compliance weighting factor, w_c. This factor balances the trade-off between shape control and structural compliance. Higher values of w_c prioritize stiffness over geometry fitting, while lower values emphasize shape accuracy. The use of adaptive filters based on element size, rather than a constant filter radius, is crucial to controlling feature sizes and minimizing issues like mesh dependency and intermediate density elements. These filters adjust based on local mesh characteristics to ensure more reliable and clearer topology.

The topology optimization is implemented using MATLAB, with airfoil shape data pre-processed from ANSYS-generated meshes. The boundary nodes of high-density elements are extracted to create a CAD model, which is then subjected to structural testing. This approach ensures that the optimized topology can be practically tested and analyzed under realistic aerodynamic loads.

The current design method encounters a challenge related to hinge reduction. In the present approach, the deformation is primarily achieved through localized hinges rather than distributed deformation across the structure. This reliance on hinges can complicate the manufacturing process, as these hinges may lead to mechanical weaknesses or increased complexity in fabrication.

To address this issue, integrating minimum feature size control within the topology optimization framework is necessary. This approach ensures that the design does not rely excessively on small, localized hinges and promotes more uniform deformation across the structure. By enforcing a minimum feature size, the optimization can produce a design that is easier to manufacture, mechanically robust, and more adaptable to real-world applications. This adjustment would allow the program to avoid small-scale features that could result in fragile or impractical designs, improving both the structural integrity and manufacturability of the optimized morphing wing.

CHAPTER 5

Conclusion and further expectations

5.1 Summary of the work

This research has undertaken an investigation into the design and optimization of an active morphing wing, focusing on aerodynamic and structural aspects. The overall objective was to develop a morphing wing that could dynamically adapt its shape in response to varying flight conditions, thus improving aircraft performance metrics such as lift, drag, and endurance. The challenges involved in this study were addressed through the integration of shape parameterization, evolutionary algorithms, topology optimization, and advanced computational techniques. MATLAB, XFOIL and commercial software are coupled to provide reliable validation of the designs and ensure that the performance improvements suggested by aerodynamic optimization were structurally possible.

5.1.1 Airfoil Shape Parameterization and Optimization

This work began with airfoil shape representation using the Bezier-PARSEC (BP) method, which was used to fit the airfoil curve relative to a baseline configuration. A modified BP method was then employed, allowing for independent optimization of the leading and trailing edges while maintaining the middle section unchanged. This segmentation approach was

critical for morphing wing design, as it enabled targeted regions of the airfoil to adapt to varying flight conditions, effectively replacing traditional control surfaces such as flaps, ailerons, and rudders.

The Differential Evolution (DE) algorithm was implemented to perform shape optimization. DE was selected for its robustness and ability to manage complex, multi-objective optimization problems, particularly in the aerodynamics optimization problems. The optimization objectives focused on maximizing the lift coefficient (C_L), lift-to-drag ratio (C_L/C_D), and endurance efficiency ($C_L^{1.5}/C_D$), which are all essential for enhancing overall aircraft performance.

The optimization process involved adjusting the camber profile within morphing ranges for the leading and trailing edges, which were carefully selected based on aerodynamic performance criteria. An innovation in this study was the inclusion of a curve length constraint, ensuring that the final optimized airfoil shapes remained physically feasible. This constraint was crucial for balancing theoretical performance improvements with practical manufacturability.

5.1.2 Structural Design and Topology Optimization

After achieving optimized airfoil shapes, the next step of the research focused on structural realization of the morphing wing. This involved designing a compliant mechanism capable of enabling controlled deformation in the morphing regions (leading and trailing edges) while maintaining sufficient stiffness to withstand aerodynamic loads. A smooth boundary mesh is generated in this thesis which makes it possible to test its aerodynamic performance after actuated.

Topology optimization techniques were employed to address the structural optimization problem. The main objective was to minimize the difference between the target geometry and the actuated geometry while ensuring adequate stiffness to bear aerodynamic loads. The leading and trailing edges were discretized using finite element models to determine the optimal material distribution. To avoid intermediate density materials in the final results, an area-adaptive filter was developed to control feature size, ensuring clean and precise topology.

Key design parameters in the topology optimization were tested to evaluate their impact on final design quality. The optimization code was verified against typical benchmark problems, and the results were compared with those from the literature to ensure accuracy. The final step of the research involved comparing the optimized morphing wing designs with baseline airfoil configurations. This analysis highlighted the aerodynamic performance improvements, as well as the structural feasibility of the optimized designs. The morphing leading and trailing edges showed significant improvements in lift coefficient and endurance compared to the baseline NACA 2418 airfoil, demonstrating that the shape optimized using the modified BP and DE method can be achieved using the designed compliant mechanism.

5.2 Further expectations

There are several ways to further improve morphing wing designs based on the findings of this thesis. First, the current shape and topology optimization were performed in a 2D design domain, which introduces challenges for applying morphing structures to real-world scenarios. In practice, the aerodynamic performance of a 3D wing is generally worse than that of a 2D airfoil. To address this, future research should focus on extending the optimization to 3D, updating aerodynamic parameters and accounting for more complex flight conditions. A 3D parameterization, such as a multi-level Bezier-PARSEC method, could represent a full wing by stacking multiple layers of airfoils together.

Second, the constant aerodynamic load used in the current topology optimization corresponds to the target shape. However, this approach neglects the design-dependent nature of aerodynamic loads, where the wing's changing geometry alters the pressure distribution. Future work should apply design-dependent loads based on deformed geometry, ensuring more accurate results for the optimized structures.

Third, the present topology optimization does not account for geometric and material nonlinearities, which can lead to inaccurate results under large deformations. Nonlinear Finite Element Analysis (FEA) should be incorporated into the optimization process, some nonlinear

topology optimization studies have shown that designs may exhibit significant differences in material distribution and performance when nonlinear effects are considered.

Moreover, this thesis assumes that the compliant mechanism is actuated by a single actuator. To achieve multiple target shapes with a single topology under different loading conditions, a multi-actuator system could be implemented. However, integrating more than one actuator presents challenges, especially in establishing effective connections between input and output ports. Designing a multi-input, multi-output compliant mechanism could be a potential solution, but it would require a more advanced approach for cases where the desired shape is complex and difficult to achieve with simple mechanisms.

Finally, this research separated aerodynamic analysis from structural design, which required multiple data conversions and modifications between stages. A fluid-structure interaction (FSI) approach would greatly improve design accuracy by directly coupling aerodynamic forces with structural mechanics. However, the computational cost of FSI can be prohibitive, as it requires solving both fluid dynamics and structural equations simultaneously. To overcome this limitation, future work could explore simplified models or assumptions to enable FSI under constrained computational resources.

References

[1] Barbarino S, Bilgen O, Ajaj RM, et al. (2011) A review of morphing aircraft. Journal of Intelligent Material Systems and Structures 22(9): 823–877.

[2] Vasista, S., Tong, L., and Wong, K. C., "Realization of morphing wings: A multidisciplinary challenge," Journal of Aircraft, vol. 49, 2012, pp. 11–28.

[3] Sofla, A. Y. N., Meguid, S. A., Tan, K. T., and Yeo, W. K., "Shape morphing of aircraft wing: Status and challenges," Materials and Design, vol. 31, 2010, pp. 1284–1292.

[4] Statkus, F. D., "Continuous Skin, Variable Camber Airfoil Edge Actuating Mechanism," U.S. Patent, 4,351,502, 28 Sept. 1982.

[5] Dunbar, B., "AFTI F-111," NASA Available:https://www.nasa.gov/centers/dryden/multimedia/imagegallery/F-111AFTI/F-111AFTI_proj_desc.html.

[6] Kudva, J. N., "Overview of the DARPA smart wing project," Journal of Intelligent Material Systems and Structures, vol. 15, 2004, pp. 261–267.

[7] Scherer, L. B., Martin, C. A., West, M. N., Florance, J. P., Wieseman, C. D., Burner, A. W., and Fleming, G. A., SPIE Proceedings, 1999.

[8] Monner, H. P., "Realization of an optimized wing camber by using formvariable flap structures," Aerospace Science and Technology, vol. 5, 2001, pp. 445–455.

[9] Kota, S., Hetrick, J. A., Osborn, R., Paul, D., Pendleton, E., Flick, P., and Tilmann, C., "Design and application of compliant mechanisms for morphing aircraft structures," SPIE Proceedings, 2003.

[10] Kota, S., Osborn, R., Ervin, G., Maric, D., Flick, P., Paul, D. (2009, April). Mission adaptive compliant wing–design, fabrication and flight test. In RTO Applied Vehicle Technology Panel (AVT) Symposium (pp. 1-18). Evora, Portugal: RTO-MP-AVT-168.

[11] Carter, D., Osborn, R., Hetrick, J., and Kota, S., "Quest for Efficient Transonic Cruise," 7th AIAA ATIO Conf, 2nd CEIAT Int'l Conf on Innov and Integr in Aero Sciences,17th

LTA Systems Tech Conf; followed by 2nd TEOS Forum, 2007.

[12] Kota, S., and Hetrick, J. A., "Adaptive Compliant Wing and Rotor System," US Patent 7384016 B2, June 10, 2008.

[13] Kota, S., Flick, P., and Collier, F. S., "Flight testing of flexfloiltm adaptive compliant trailing edge," 54th AIAA Aerospace Sciences Meeting, 2016.

[14] Mkhoyan, T., Thakrar, N. R., De Breuker, R., and Sodja, J., "Design and development of a seamless smart morphing wing using Distributed Trailing Edge camber morphing for active control," AIAA Scitech 2021 Forum, 2021.

[15] Woods, B. K., Bilgen, O., and Friswell, M. I., "Wind tunnel testing of the Fish Bone Active camber morphing concept," Journal of Intelligent Material Systems and Structures, vol. 25, 2014, pp. 772–785.

[16] Burns, R. H., and E., C. F. R., Kinetostatic synthesis of flexible link mechanisms, New York, NY: ASME, 1968.

[17] Howell, L. L., and Midha, A., "Parametric deflection approximations for end-loaded, large-deflection beams in compliant mechanisms," Journal of Mechanical Design, vol. 117, 1995, pp. 156–165.

[18] Ole Sigmund (1997) On the Design of Compliant Mechanisms Using Topology Optimization, Mechanics of Structures and Machines, 25:4, 493-524, DOI: 10.1080/08905459708945415

[19] Her, I., and Midha, A., "A compliance number concept for compliant mechanisms, and type synthesis," Journal of Mechanisms, Transmissions, and Automation in Design, vol. 109, 1987, pp. 348–355.

[20] Midha, A., Norton, T. W., and Howell, L. L., "On the nomenclature and classification of compliant mechanisms: Abstractions of mechanisms and mechanism synthesis problems," 22nd Biennial Mechanisms Conference: Flexible Mechanisms, Dynamics, and Analysis, 1992.

[21] Murphy, M. D., Midha, A., and Howell, L. L., "The topological synthesis of compliant mechanisms," Mechanism and Machine Theory, vol. 31, 1996, pp. 185–199.

[22] Gallego, J. A., and Herder, J., "Synthesis methods in compliant mechanisms: An overview," Volume 7: 33rd Mechanisms and Robotics Conference, Parts A and B, 2009.

[23] Yu, J., Li, S., Su, H., and Culpepper, M. L., "Screw theory based methodology for the deterministic type synthesis of flexure mechanisms," Journal of Mechanisms and Robotics, vol. 3, 2011.

[24] Yu, J., Dong, X., Pei, X., and Kong, X., "Mobility and singularity analysis of a class of two degrees of freedom rotational parallel mechanisms using a visual graphic approach,"

Journal of Mechanisms and Robotics, vol. 4, 2012.

[25] L.L. Howell, Compliant Mechanisms, John Wiley and Sons, 2001.

[26] Wang, N., Zhang, Z., Yue, F., and Zhang, X., "Exploration of translational joint design using corrugated flexure units with Bézier curve segments," Journal of Mechanical Design, vol. 141, 2019.

[27] Zhang, H., Zhu, B., and Zhang, X., "Origami kaleidocycle-inspired symmetric multistable compliant mechanisms," Journal of Mechanisms and Robotics, vol. 11, 2018.

[28] Ling, M., Cao, J., Howell, L. L., and Zeng, M., "Kinetostatic modeling of complex compliant mechanisms with serial-parallel substructures: A semi-analytical matrix displacement method," Mechanism and Machine Theory, vol. 125, 2018, pp. 169–184.

[29] Dearden, J., Grames, C., Orr, J., Jensen, B. D., Magleby, S. P., and Howell, L. L., "Cylindrical cross-axis flexural pivots," Precision Engineering, vol. 51, 2018, pp. 604–613.

[30] Pei, X., Yu, J., Zong, G., and Bi, S., "An effective pseudo-rigid-body method for beam-based compliant mechanisms," Precision Engineering, vol. 34, 2010, pp. 634–639.

[31] Zhao, H., Zhao, C., Ren, S., and Bi, S., "Analysis and evaluation of a near-zero stiffness rotational flexural pivot," Mechanism and Machine Theory, vol. 135, 2019, pp. 115–129.

[32] Bendsoe, M. P., and Sigmund, O., Topology Optimization: Theory, methods, and applications, Berlin: Springer, 2004.

[33] Nishiwaki, S., Frecker, M. I., Min, S., and Kikuchi, N., "Topology optimization of compliant mechanisms using the homogenization method," International Journal for Numerical Methods in Engineering, vol. 42, 1998, pp. 535–559.

[34] Frecker, M. I., Ananthasuresh, G. K., Nishiwaki, S., Kikuchi, N., and Kota, S., "Topological synthesis of compliant mechanisms using multi-criteria optimization," Journal of Mechanical Design, vol. 119, 1997, pp. 238–245.

[35] Zhang, X., and Zhu, B., Topology optimization of compliant mechanisms, 2018.

[36] Li, D., "Multi-objective topology optimization of Thermo-mechanical compliant mechanisms," Chinese Journal of Mechanical Engineering, vol. 24, 2011, p. 1123.

[37] Tran, A. V., Zhang, X., and Zhu, B., "The development of a new piezoresistive pressure sensor for low pressures," IEEE Transactions on Industrial Electronics, vol. 65, 2018, pp. 6487–6496.

[38] Cao, L., Dolovich, A. T., Chen, A., and Zhang, W. (Chris), "Topology optimization of efficient and strong hybrid compliant mechanisms using a mixed mesh of beams and flexure hinges with strength control," Mechanism and Machine Theory, vol. 121, 2018,

pp. 213–227.

[39] Frecker, M., Kikuchi, N., and Kota, S., "Topology optimization of compliant mechanisms with multiple outputs," Structural Optimization, vol. 17, 1999, pp. 269–278.

[40] Hetrick, J. A., and Kota, S., "An energy formulation for parametric size and shape optimization of compliant mechanisms," Journal of Mechanical Design, vol. 121, 1999, pp. 229–234.

[41] S. Kota, J. Joo, Z. Li, S.M. Rodgers, J. Sniegowski, Design of compliant mechanisms: applications to mems, Analog Integr. Circt. Signal Process. 29 (1–2) (2001) 7–15.

[42] Saxena, A., and Ananthasuresh, G. K., "On an optimal property of compliant topologies," Structural and Multidisciplinary Optimization, vol. 19, 2000, pp. 36–49.

[43] Zhan, J., "Topology optimization of compliant mechanisms with geometrical nonlinearities using the ground structure approach," Chinese Journal of Mechanical Engineering, vol. 24, 2011, p. 257.

[44] J. Zhan, X. Zhang, Research on static and dynamic multi-objective topology optimization of continuum structures, J. Mech. Strength 6 n(2010).

[45] Ananthasuresh, G. K., Kota, S., and Gianchandani, Y., "A methodical approach to the design of compliant MICROMECHANISMS," 1994 Solid-State, Actuators, and Microsystems Workshop Technical Digest, 1994.

[46] G. Ananthasuresh, S. Kota, N. Kikuchi, Strategies for systematic synthesis of compliant mems, in: Proceedings of the 1994 ASME Winter Annual Meeting, 1994, pp. 677–686.

[47] Nishiwaki, S., Frecker, M. I., Min, S., and Kikuchi, N., "Topology optimization of compliant mechanisms using the homogenization method," International Journal for Numerical Methods in Engineering, vol. 42, 1998, pp. 535–559.

[48] U.D. Larsen, O. Sigmund, S. Bouwsta, Design and fabrication of compliant micromechanisms and structures with negative Poisson's ratio, J. Microelectromech. Syst. 6 (2) (1997) 99–106.

[49] Zhu, B., Zhang, X., Zhang, H., Liang, J., Zang, H., Li, H., and Wang, R., "Design of compliant mechanisms using continuum topology optimization: A Review," Mechanism and Machine Theory, vol. 143, 2020, p. 103622.

[50] Nishiwaki, S., Frecker, M. I., Min, S., and Kikuchi, N., "Topology optimization of compliant mechanisms using the homogenization method," International Journal for Numerical Methods in Engineering, vol. 42, 1998, pp. 535–559.

[51] G.K. Lau, H. Du, M.K. Lim, Techniques to suppress intermediate density in topology optimization of compliant mechanisms, Comput. Mech. 27 (5) (2001) 426–435.

[52] T. Buhl, Simultaneous topology optimization of structure and supports, Struct. Multidiscip. Optim. 23 (5) (2002) 336–346.

[53] G. Allaire, F. Jouve, A.M. Toader, Structural optimization using sensitivity analysis and a level-set method, J. Comput. Phys. 194 (1) (2004) 363–393.

[54] Luo, Z., Tong, L., and Wang, M. Y., "Design of distributed compliant micromechanisms with an implicit free boundary representation," Structural and Multidisciplinary Optimization, vol. 36, 2007, pp. 607–621.

[55] Ansola, R., Veguería, E., Canales, J., and Tárrago, J. A., "A simple evolutionary topology optimization procedure for compliant mechanism design," Finite Elements in Analysis and Design, vol. 44, 2007, pp. 53–62.

[56] Ansola, R., Veguería, E., Maturana, A., and Canales, J., "3D compliant mechanisms synthesis by a finite element addition procedure," Finite Elements in Analysis and Design, vol. 46, 2010, pp. 760–769.

[57] Takezawa, A., Nishiwaki, S., and Kitamura, M., "Shape and topology optimization based on the phase field method and sensitivity analysis," Journal of Computational Physics, vol. 229, 2010, pp. 2697–2718.

[58] Gain, A. L., and Paulino, G. H., "Phase-field based topology optimization with polygonal elements: A finite volume approach for the evolution equation," Structural and Multidisciplinary Optimization, vol. 46, 2012, pp. 327–342.

[59] GUO, X., "Doing topology optimization explicitly and geometrically: A new moving morphable components based framework," Frontiers in Applied Mechanics, 2015, pp. 31–32.

[60] Zhang, W., Li, D., Yuan, J., Song, J., and Guo, X., "A new three-dimensional topology optimization method based on moving morphable components (mmcs)," Computational Mechanics, vol. 59, 2016, pp. 647–665.

[61] Sharma, D., Deb, K., and Kishore, N. N., "Domain-specific initial population strategy for compliant mechanisms using customized genetic algorithm," Structural and Multidisciplinary Optimization, vol. 43, 2010, pp. 541–554.

[62] Yoo, K.-S., and Han, S.-Y., "Topology optimum design of compliant mechanisms using modified ant colony optimization," Journal of Mechanical Science and Technology, vol. 29, 2015, pp. 3321–3327.

[63] Vasista, S., and Tong, L., "Design and testing of pressurized cellular planar morphing structures," AIAA Journal, vol. 50, 2012, pp. 1328–1338.

[64] Pedersen, C. B., Buhl, T., and Sigmund, O., "Topology synthesis of large-displacement compliant mechanisms," International Journal for Numerical Methods in Engineering, vol. 50, 2001, pp. 2683–2705.

[65] Shili, L., Wenjie, G., and Shujun, L., "Optimal design of compliant trailing edge for shape changing," Chinese Journal of Aeronautics, vol. 21, 2008, pp. 187–192.

[66] Zhang, Y., Ge, W., Zhang, Z., Mo, X., and Zhang, Y., "Design of compliant mechanism-based Variable camber morphing wing with nonlinear large deformation," International Journal of Advanced Robotic Systems, vol. 16, 2019, p. 172988141988674.

[67] LI, Y., GE, W., ZHOU, J., ZHANG, Y., ZHAO, D., WANG, Z., and DONG, D., "Design and experiment of concentrated flexibility-based Variable Camber Morphing Wing," Chinese Journal of Aeronautics, vol. 35, 2022, pp. 455–469.

[68] Tong, X., Ge, W., Sun, C., and Liu, X., "Topology optimization of compliant adaptive wing leading edge with composite materials," Chinese Journal of Aeronautics, vol. 27, 2014, pp. 1488–1494.

[69] Tong, X., Ge, W., Gao, X., and Li, Y., "Simultaneous optimization of fiber orientations and topology shape for composites compliant leading edge," Journal of Reinforced Plastics and Composites, vol. 38, 2019, pp. 706–716.

[70] TONG, X., GE, W., YUAN, Z., GAO, D., and GAO, X., "Integrated design of topology and material for composite morphing trailing edge based compliant mechanism," Chinese Journal of Aeronautics, vol. 34, 2021, pp. 331–340.

[71] Li, D., Zhao, X., De Breuker, R., and Abdalla, M. M., "A Review of Modelling and Analysis of Morphing Wings," Progress in Aerospace Sciences, Vol. 100, 2018, pp. 46–62. https://doi.org/10.1016/j.paerosci.2018.06.002.

[72] Rogalsky, T. P., "Acceleration of differential evolution for aerodynamic design," thesis, 2004.

[73] Derksen, R. W., and Rogalsky, T., "Bezier-Parsec: An optimized aerofoil parameterization for design," Advances in Engineering Software, vol. 41, 2010, pp. 923–930.

[74] Chan YY. Applications of genetic algorithms to aerodynamic design. Can Aeronaut Space J 1998;44(3):182–7.

[75] Rogalsky T, Derksen RW, Kocabiyik S. Differential evolution in aerodynamic optimization. Can Aeronaut Space J 2000;46(4):183–90.

[76] Amoiralis EI, Nikolos IK. Freeform deformation versus B-spline representation in inverse airfoil design. J Comput Inform Sci Eng 2008;8(2):024001-1–024001-13.

[77] Price, K., Storn, R. M., and Lampinen, J. A., Differential evolution a practical approach to global optimization, Berlin: Springer Berlin, 2014.

[78] Storn, R., Price, K. (1997). Differential evolution-a simple and efficient heuristic for global optimization over continuous spaces. Journal of global optimization, 11(4), 341.

[79] Sobieczky, H., “Parametric airfoils and Wings,” Notes on Numerical Fluid Mechanics (NNFM), 1999, pp. 71–87.

[80] Vasista, S., and Tong, L., "Topology Optimisation via the Moving ISO-Surface Threshold Method: Implementation and Application," The Aeronautical Journal, Vol. 118, No. 1201, 2014, pp. 315–342.

[81] Sigmund, O., “Efficient Topology Optimization in MATLAB Using 88 Lines of Code,” Structural and Multidisciplinary Optimization, Vol. 21, No. 2, 2001, pp. 120–127. https://doi.org/10.1007/s001580050176

[82] Svanberg, K., “The Method of Moving Asymptotes—A New Method for Structural Optimization,” *International Journal for Numerical Methods in Engineering*, Vol. 24, No. 2, 1987, pp. 359–373.
doi:10.1002/nme.1620240207

[83] Svanberg, K., “A Class of Globally Convergent Optimization Methods Based on Conservative Convex Separable Approximations,” *SIAM Journal on Optimization*, Vol. 12, No. 2, 2002, pp. 555–573.
doi:10.1137/S1052623499362822

[84] Svanberg, K., “SMOPtiT – Structural and Multidisciplinary Optimization Tool,” SMOPtiT, URL: https://www.smoptit.se/ [cited 12 August 2024].

[85] Sigmund, O., “Morphology-Based Black and White Filters for Topology Optimization,” *Structural and Multidisciplinary Optimization*, Vol. 33, Nos. 4–5, 2007, pp. 401–424.
doi:10.1007/s00158-006-0087-z

[86] Anderson, J. D. Jr., Introduction to Flight, 8th ed., McGraw-Hill Education, New York, 2015, pp. 506.

CHAPTER A

FEA Formulations

A1 4-node element equations

A1.1 Shape Functions N

The shape functions for a 2D quadrilateral element are defined as follows:

$$\begin{cases} N_1 = \frac{1}{4}(1-\xi)(1-\eta) \\ N_2 = \frac{1}{4}(1+\xi)(1-\eta) \\ N_3 = \frac{1}{4}(1+\xi)(1+\eta) \\ N_4 = \frac{1}{4}(1-\xi)(1+\eta) \end{cases}$$

The shape function matrix N is given by:

$$N = \begin{bmatrix} N_1 & 0 & N_2 & 0 & N_3 & 0 & N_4 & 0 \\ 0 & N_1 & 0 & N_2 & 0 & N_3 & 0 & N_4 \end{bmatrix}$$

A1.2 Strain-Displacement Relationship

$$\epsilon_{xx} = \frac{\partial u}{\partial x} = \frac{\partial u(\xi,\eta)}{\partial x} = \frac{\partial}{\partial x}\left(\sum_{i=1}^{n} N_i(\xi,\eta)u_i\right)$$

$$\epsilon_{yy} = \frac{\partial v}{\partial y} = \frac{\partial v(\xi,\eta)}{\partial y} = \frac{\partial}{\partial y}\left(\sum_{i=1}^{n} N_i(\xi,\eta)v_i\right)$$

$$2\epsilon_{xy} = \left(\frac{\partial u(\xi,\eta)}{\partial y} + \frac{\partial v(\xi,\eta)}{\partial x}\right) = \frac{\partial}{\partial y}\left(\sum_{i=1}^{n} N_i(\xi,\eta)u_i\right) + \frac{\partial}{\partial x}\left(\sum_{i=1}^{n} N_i(\xi,\eta)v_i\right)$$

A1.3 Displacement in Shape Functions

$$u = \mathbf{N}\mathbf{q} \quad \text{where} \quad \mathbf{q} = \begin{bmatrix} u_1 & v_1 & u_2 & v_2 & u_3 & v_3 & u_4 & v_4 \end{bmatrix}^T$$

$$\begin{cases} u = \sum_{i=1}^{4} N_i(x,y)u_i = N_1u_1 + N_2u_2 + N_3u_3 + N_4u_4 \\ v = \sum_{i=1}^{4} N_i(x,y)v_i = N_1v_1 + N_2v_2 + N_3v_3 + N_4v_4 \end{cases}$$

$$\begin{bmatrix} u \\ v \end{bmatrix} = \begin{bmatrix} N_1 & 0 & N_2 & 0 & N_3 & 0 & N_4 & 0 \\ 0 & N_1 & 0 & N_2 & 0 & N_3 & 0 & N_4 \end{bmatrix} \begin{bmatrix} u_1 \\ v_1 \\ u_2 \\ v_2 \\ u_3 \\ v_3 \\ u_4 \\ v_4 \end{bmatrix}$$

A1.4 Matrix Form of Strain

$$\epsilon = \begin{bmatrix} \epsilon_{xx} \\ \epsilon_{yy} \\ 2\epsilon_{xy} \end{bmatrix} = \begin{bmatrix} \frac{\partial N_1}{\partial x} & 0 & \frac{\partial N_2}{\partial x} & 0 & \frac{\partial N_3}{\partial x} & 0 & \frac{\partial N_4}{\partial x} & 0 \\ 0 & \frac{\partial N_1}{\partial y} & 0 & \frac{\partial N_2}{\partial y} & 0 & \frac{\partial N_3}{\partial y} & 0 & \frac{\partial N_4}{\partial y} \\ \frac{\partial N_1}{\partial y} & \frac{\partial N_1}{\partial x} & \frac{\partial N_2}{\partial y} & \frac{\partial N_2}{\partial x} & \frac{\partial N_3}{\partial y} & \frac{\partial N_3}{\partial x} & \frac{\partial N_4}{\partial y} & \frac{\partial N_4}{\partial x} \end{bmatrix} \begin{bmatrix} u_1 \\ v_1 \\ u_2 \\ v_2 \\ u_3 \\ v_3 \\ u_4 \\ v_4 \end{bmatrix}$$

A1.5 Constitutive Matrix D

The constitutive matrix D for plane stress of each element is given by:

$$D_e(\rho_e) = \begin{bmatrix} \frac{E_e}{1-\nu^2} & \frac{\nu E_e}{1-\nu^2} & 0 \\ \frac{\nu E_e}{1-\nu^2} & \frac{E_e}{1-\nu^2} & 0 \\ 0 & 0 & \frac{E_e}{2(1+\nu)} \end{bmatrix}$$

A1.6 Element Stiffness Matrix

The element stiffness matrix ke is calculated using:

$$[K_e]_{8\times 8} = \int_{A_e} B^T D_e B \cdot t \cdot dA$$

where B is the strain-displacement matrix, D is the constitutive matrix, J is the Jacobian matrix, and t is the thickness. The area dA is defined as:

$$dA = dxdy = \det[J]d\xi d\eta$$

A1.7 Strain-Displacement Matrix B

The matrix B is derived from the shape function derivatives and the Jacobian matrix:

$$B = A \cdot G$$

where

$$A = \frac{1}{\det(J)} \begin{bmatrix} J_{22} & -J_{12} & 0 & 0 \\ 0 & 0 & -J_{21} & J_{11} \\ -J_{21} & J_{11} & J_{22} & -J_{12} \end{bmatrix}$$

and G is a matrix of shape function derivatives.

A1.8 Jacobian Matrix J

The Jacobian matrix for each element is computed as:

$$J = \frac{1}{4} \begin{bmatrix} -(1-\eta) & (1-\eta) & (1+\eta) & -(1+\eta) \\ -(1-\xi) & -(1+\xi) & (1+\xi) & (1-\xi) \end{bmatrix} \begin{bmatrix} x_1 & y_1 \\ x_2 & y_2 \\ x_3 & y_3 \\ x_4 & y_4 \end{bmatrix}$$

A1.9 Computation of G Matrix

The matrix G for a quadrilateral element is computed as follows:

$$G = \frac{1}{4} \begin{bmatrix} \eta-1 & 0 & 1-\eta & 0 & \eta+1 & 0 & -\eta-1 & 0 \\ \xi-1 & 0 & -\xi-1 & 0 & \xi+1 & 0 & 1-\xi & 0 \\ 0 & \eta-1 & 0 & 1-\eta & 0 & \eta+1 & 0 & -\eta-1 \\ 0 & \xi-1 & 0 & -\xi-1 & 0 & \xi+1 & 0 & 1-\xi \end{bmatrix}$$

For a 2x2 integration, there are four integration points. These points are located symmetrically within the element at ±0.5774 in both the η and ξ directions. Each point has an equal weight of 1.

A1.10 Displacement Vector U)

The displacement vector U is obtained by solving the linear system:

$$KU = F$$